Advanced

Relaxation Oscillation SQUIDs

Cover: Optical micrograph of the prototype of the "smart DROS" (chapter 5).

The work described in this thesis has been financially supported by the "Stichting voor Technische Wetenschappen" (STW). It has been performed in the Low Temperature Division of the Department of Applied Physics at the University of Twente, P.O. Box 217, 7500 AE Enschede, The Netherlands.

M.J. van Duuren,
Advanced Relaxation Oscillation SQUIDs,
Proefschrift Universiteit Twente, Enschede.

ISBN 90-365-10740

Druk: FEBO druk BV, Enschede

ADVANCED RELAXATION OSCILLATION SQUIDS

PROEFSCHRIFT

ter verkrijging van
de graad van doctor aan de Universiteit Twente,
op gezag van de rector magnificus,
prof. dr. F.A. van Vught,
volgens besluit van het College voor Promoties
in het openbaar te verdedigen
op donderdag 22 januari 1998 te 13.15 uur.

door

Michiel Jos van Duuren
geboren op 15 maart 1970
te Groenlo

Dit proefschrift is goedgekeurd door:

prof. dr. H. Rogalla (promotor)
dr. ir. J. Flokstra (assistent-promotor)

Contents

Chapter 1

Introduction

The first direct current superconducting quantum interference device (dc SQUID) was reported in 1964 by Jaklevic *et al.* [1,2,3]. A dc SQUID consists of a superconducting loop, interrupted by two weak links, the so-called Josephson junctions. The main purpose of the experiments of Jaklevic *et al.* was the direct observation of two physical phenomena, viz. the macroscopic phase coherence of the superconducting wave function and the Josephson effect [4]. Later, dc SQUIDs turned out to be excellent flux sensors and, currently, they constitute the most sensitive magnetic flux detectors.

SQUIDs can be fabricated using conventional low T_c metallic superconductors, as for instance Pb, Nb or NbN, but also with the relatively new high T_c ceramic superconductors [5], such as $YBa_2Cu_3O_{7-\delta}$. Due to their low superconducting transition temperature of the order of 10 K, most low T_c devices are operated at a temperature of 4.2 K in liquid ^{4}He. The high T_c devices have a much higher transition temperature, typically above 90 K, enabling operation at higher temperatures, e.g. at 77 K, the boiling point of N_2. The discussion in this thesis will be restricted to the more sensitive low T_c devices.

As SQUIDs can sense very accurately any physical quantity that can be converted to a magnetic flux, for instance magnetic field, electric current or mechanical displacement, they have a wide field of applications. A well-known example is the detection of the very small magnetic signals that are produced by the human brain (magneto-encephalography) or heart (magneto-cardiography) [6]. An illustration of such a bio-magnetic measurement is shown in Fig. 1.1. Other applications are the readout of cryogenic particle detectors such as bolometers, superconducting tunnel junctions or gravitational wave antennae [7,8], non-destructive testing [6], susceptometers [9], picovoltmeters [10] and magnetic microscopes [6,11].

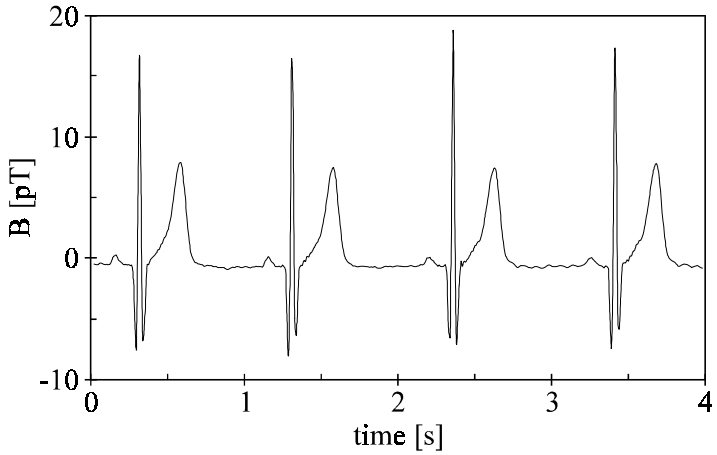

Figure 1.1 *A magneto-cardiogram measured in the magnetically shielded room at the University of Twente. Details concerning the measurement system will be presented in section 4.3.*

Essentially, a dc SQUID is a flux-to-voltage converter. Due to the limited flux-to-voltage transfer of conventional dc SQUIDs, a sophisticated readout configuration is required. This readout scheme, involving ac flux modulation techniques and cooled step-up transformers between the dc SQUID and the room temperature pre-amplifier, limits the versatility of standard dc SQUIDs. A major restriction caused by the readout scheme is for instance the measurement bandwidth, which is typically below 100 kHz. Certain applications, e.g. the readout of X-ray spectrometers based on superconducting tunnel junctions, require the outstanding sensitivity of a dc SQUID, but a bandwidth considerably larger than that typical value.

Some imaging applications, such as bio-magnetism or non-destructive testing, require many parallel channels for sufficient spatial resolution [6]. In such large systems, which can comprise as many as hundred or more SQUIDs, the standard flux modulated readout scheme can induce crosstalk between adjacent channels. Moreover, the cooled step-up transformers, which are located close to the SQUIDs, increase the complexity, and thus the production costs of the systems.

To avoid such complications, various “second generation” dc SQUIDs, enabling simpler readout schemes without degrading the sensitivity, have been developed [12]. In the Low Temperature Division at the University of Twente, the development of second generation SQUIDs started in the early 1990’s with the fabrication of relaxation oscillation SQUIDs (ROSs) and double relaxation oscillation SQUIDs (DROSs) [13], which are based on relaxation oscillations [14] induced in hysteretic Josephson elements by an external L-R circuit. In this thesis, the research concerning further improvement of (D)ROSs is described.

In chapter 2, the basics of conventional dc SQUID systems are discussed, followed by a concise survey of various second generation dc SQUIDs, including the ROS and the DROS. The ROS, which is a flux-to-frequency converter, is discussed thoroughly in chapter 3. In that chapter, theoretical and experimental ROS characteristics are presented.

The subject of chapter 4 is the DROS. Like conventional dc SQUIDs, a DROS is a flux-to-voltage transducer, but its flux-to-voltage transfer coefficient exceeds that of a standard dc SQUID by typically one order of magnitude. This allows a simple, reliable and fast readout scheme based on direct voltage detection with a room temperature pre-amplifier. As the experimental results presented in chapter 4 indicate, the sensitivity of DROSs matches that of standard dc SQUIDs, notwithstanding the straightforward readout electronics.

As will be demonstrated in chapter 5, the output signal of a DROS is particularly suited for digital readout, e.g. with integrated superconducting Josephson electronics. Potentially, such an integrated "smart DROS" sensor has a very large measurement bandwidth. In addition, the number of wires between the room temperature electronics and the SQUID sensors in a multi-channel system could be reduced substantially. Fully integrated smart DROS prototypes have been designed, fabricated and characterized. The experimental characteristics showed that the devices operated according to the theoretical expectations. These results offer promising perspectives for future developments.

References

[1] R.C. Jaklevic, J.J. Lambe, A.H. Silver and J.E. Mercereau, "Quantum interference effects in Josephson tunneling", *Phys. Rev. Lett.* **12**, 159-160 (1964).

[2] R.C. Jaklevic, J.J. Lambe, A.H. Silver and J.E. Mercereau, "Quantum interference from a static vector potential in a field-free region", *Phys. Rev. Lett.* **12**, 274-275 (1964).

[3] R.C. Jaklevic, J.J. Lambe, J.E. Mercereau and A.H. Silver, "Macroscopic quantum interference in superconductors", *Phys. Rev.* **5A**, 1628-1637 (1965).

[4] B.D. Josephson, "Possible new effects in superconductive tunneling", *Phys. Lett.* **1**, 251-253 (1962).

[5] J.G. Bednorz and K.A. Müller, "Possible high T_c superconductivity in the Ba-La-Cu-O system", *Z. Phys. B* **64**, 189-193 (1986).

[6] J.P. Wikswo Jr., "SQUID magnetometers for biomagnetism and nondestructive testing: Important questions and initial answers", *IEEE Trans. Appl. Supercond.* **5**, 74-120 (1995).

[7] N.E. Booth and D.J. Goldie, "Superconducting particle detectors", *Supercond. Sci. Technol.* **9**, 493-516 (1996).

[8] see, for instance, *The detection of gravitational waves*, ed. D.G. Blair, Cambridge University Press, Cambridge (1993).

[9] M. Ketchen, D.J. Pearson, K. Stawiasz, C-K. Hu, A.W. Kleinsasser, T. Brunner, C. Cabral, V. Chandrashekhar, M. Jaso, M. Manny, K. Stein, M. Bhushan, "Octagonal washer dc SQUIDs and integrated susceptometers fabricated in a planarized sub-μm Nb-AlO_x-Nb technology", *IEEE Trans. Appl. Supercond.* **3**, 1795-1799 (1993).

[10] V. Polushkin, D. Drung and H. Koch, “A broadband picovoltmeter based on the direct current superconducting quantum interference device with additional positive feedback”, *Rev. Sci. Instrum.* **65**, 3005-3011 (1994).

[11] J.P. Wikswo Jr., “High-resolution magnetic imaging: cellular action currents and other applications”, in *SQUID Sensors: Fundamentals, Fabrication and Applications*, ed. H. Weinstock, NATO ASI Series **329**, Kluwer Academic Publishers, Dordrecht / Boston / London (1996).

[12] D. Drung, “Recent low temperature SQUID developments”, *IEEE Trans. Appl. Supercond.* **4**, 121-127 (1994).

[13] D.J. Adelerhof, *Second generation dc SQUID magnetometers: (Double) Relaxation Oscillation SQUIDs*, Ph.D. thesis University of Twente, Enschede (1993).

[14] F.L. Vernon and R.J. Pedersen, “Relaxation oscillations in Josephson junctions”, *J. Appl. Phys.* **39**, 2661-2664 (1968).

Chapter 2

SQUIDs

The operation principle of superconducting quantum interference devices (SQUIDs) is based on two phenomena inherent to superconductivity, namely the macroscopic character of the superconducting wave function and the Josephson effects. These two keystones of superconducting electronics will be discussed in sections 2.1 and 2.2, whereas the basic theory for the dc SQUID will be presented in section 2.3.

A dc SQUID is a non-linear flux-to-voltage converter and is generally operated as a null-detector in a feedback loop, the so-called *flux locked loop*. In section 2.4, this flux locked loop and the conventional flux modulation scheme which is used to match the low output impedance of the SQUID to the high input impedance of the room temperature pre-amplifier are discussed. For some applications, for instance those requiring fast and simple electronics, this modulated readout scheme is impractical or even unsuitable. To enable operation without modulation schemes, various “second generation” dc SQUID types, for example the relaxation oscillation SQUID and the double relaxation oscillation SQUID, have been developed. A short review of some common second generation dc SQUIDs is given in section 2.5.

2.1 Basics of superconductivity

Before turning the attention to SQUIDs, some basic concepts of superconductivity will be introduced in this section. When a superconductor is cooled below its critical temperature T_c, its electrical resistance vanishes abruptly. Another peculiar property of a superconductor is that it shows perfect diamagnetism, a phenomenon known as the *Meissner effect*. In other words, both the electric field $\boldsymbol{E}$ and the magnetic field $\boldsymbol{B}$ are equal to zero in the bulk of

the material. The expulsion of the magnetic field is caused by superconducting screening currents in the surface layer. Within this layer, the magnetic field decreases exponentially over a characteristic length λ_L, the *London penetration depth*.

2.1.1 The BCS theory

The *BCS theory* [1], developed in 1957 by Bardeen, Cooper and Schrieffer, states that, due to the strong electron-phonon interaction in a superconductor, it is energetically favourable for electrons to condense into pairs at the Fermi energy E_F. As these *Cooper pairs* are bosons, they all occupy the same quantum state, described by the macroscopic complex wave function Ψ. The squared amplitude of this wave function, $|\Psi|^2$, can be interpreted as the fraction of the conduction electrons which has condensed into Cooper pairs. Thus, in the normal state, $|\Psi| \equiv 0$, and in the superconducting state it varies between 0 and 1.

Figure 2.1 shows a semiconductor-like representation of the electronic density of states $N(E)$ in a superconductor according to the BCS theory. As can be seen, an *energy gap* Δ is present at both sides of E_F. For temperatures just below T_c, Δ depends strongly on the temperature, whereas at lower temperatures, i.e. below $\sim T_c/2$, the gap energy does not vary significantly with temperature. At finite temperatures, some Cooper pairs are thermally excited and form electron-like and hole-like charge carriers, the so-called *quasiparticles*. In the semiconductor representation, the hole-like excitations are modeled as missing electrons in the initially completely filled energy band below E_F.

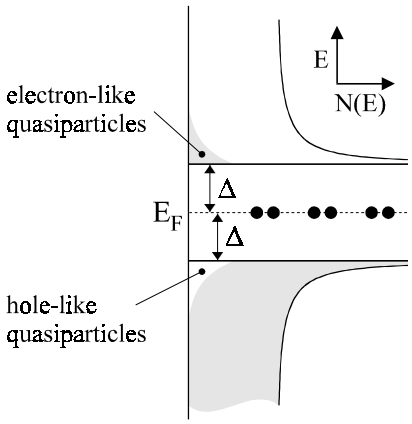

Figure 2.1 *Density of states in a superconductor at $T > 0$. The shaded regions represent occupied electron-like states and the dots at $E = E_F$ symbolize Cooper pairs.*

2.1.2 Flux quantization

The phase difference $\Delta\varphi$ [2] of the superconducting wave function between two points P_1 and P_2 in a superconductor depends on the supercurrent density $\boldsymbol{J_s}$ and on the magnetic vector potential $\boldsymbol{A}$, defined as $\boldsymbol{B}$ = rot $\boldsymbol{A}$:

$$\Delta\varphi = \frac{2\pi}{h}\int_{P_1}^{P_2}\left(\frac{2m}{n_s e}\vec{J}_s + 2e\vec{A}\right)\cdot d\vec{l}\ . \tag{2.1a}$$

In Eq. (2.1a), $h = 6.63\cdot10^{-34}$ J·s is Planck's constant, $m = 9.11\cdot10^{-31}$ kg represents the mass of an electron, n_s is the number of superconducting electrons per m^3 and $e = 1.60\cdot10^{-19}$ C symbolizes the electric charge of an electron. When calculating the integral of Eq. (2.1a) along an arbitrary closed path within the superconductor, a phase difference of $n\cdot2\pi$ should result, otherwise Ψ would not be single valued. Thus,

$$\begin{aligned}\Delta\varphi &= 2\pi\left(\frac{2m}{h n_s e}\oint\vec{J}_s\cdot d\vec{l} + \frac{2e}{h}\Phi\right) = n\cdot 2\pi \\ &\Leftrightarrow \\ \Phi' &= \frac{m}{n_s e^2}\oint\vec{J}_s\cdot d\vec{l} + \Phi = n\cdot\frac{h}{2e} = n\cdot\Phi_0\ .\end{aligned} \tag{2.1b}$$

In this equation, n is an integer, Φ symbolizes the total magnetic flux enclosed by the path of integration, and the quantity Φ' represents the *fluxoid*. According to Eq. (2.1b), Φ' is quantized in units of $\Phi_0 = h/2e = 2.07\cdot10^{-15}$ Wb, the *flux quantum*.

Inside the bulk of a superconductor, $\boldsymbol{J_s} = \boldsymbol{0}$ and hence Eq. (2.1b) reduces in this case to:

$$\Phi = n\cdot\Phi_0\ . \tag{2.1c}$$

As Eq. (2.1c) expresses, the magnetic flux in a superconducting loop is quantized in units of Φ_0, a property known as *flux quantization*.

2.2 Josephson junctions

2.2.1 The Josephson equations

A Josephson tunnel junction consists of two superconducting electrodes which are separated by a thin insulating barrier of thickness *d*. If *d* is sufficiently small, of the order of 1 nm, the superconducting wave functions in both electrodes are correlated. Because of this correlation, or *weak link*, Cooper pairs can tunnel between the two electrodes and a supercurrent can flow through the

barrier without causing a voltage drop [3]. This Cooper pair tunnel current I_{CP} influences the phase difference ϕ between the wave functions in both electrodes, as is expressed by the *dc Josephson equation*:

$$I_{CP} = I_0 \sin\phi . \tag{2.2}$$

In Eq. (2.2), the *critical current* I_0 represents the maximum value of I_{CP}. If the current through the junction is increased above I_0, a voltage V will develop across the barrier. Because of this voltage, the phase difference ϕ changes in time. This phenomenon is described by the *ac Josephson equation*:

$$\frac{\partial\phi}{\partial t} = \frac{2e}{\hbar}V \qquad (\hbar = h/2\pi) . \tag{2.3}$$

Equations (2.3) and (2.2) imply that a time-averaged voltage $\langle V \rangle$ across a Josephson junction causes an alternating Josephson current with a frequency of $f_J = (2e/h)\cdot\langle V \rangle = (483.59767\ \text{MHz}/\mu\text{V})\cdot\langle V \rangle$. This property can for instance be used for the construction of voltage standards.

2.2.2 Quasiparticle tunneling

In the presence of a potential difference, the quasiparticles can tunnel through the barrier. In Fig. 2.2a, the semiconductor energy representation is applied to a Josephson junction which is biased at a voltage between zero and the *gap voltage* $V_g = (\Delta_A+\Delta_B)/e$, with $\Delta_{A,B}$ the gap energies of the electrodes. Since in this case only the thermally excited quasiparticles can tunnel through the barrier, the resulting tunnel current is rather small and strongly dependent on the temperature.

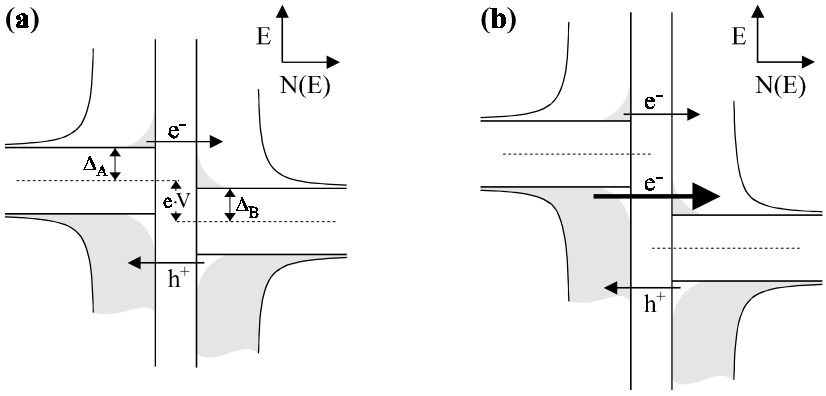

Figure 2.2 *Density of states in the electrodes of a Josephson junction for bias voltages* $V < V_g$ **(a)** *and* $V > V_g$ **(b)**. *The quasiparticle tunnel currents are indicated with arrows, marked* e^- *for electron-like quasiparticles and* h^+ *for hole-like quasiparticles.*

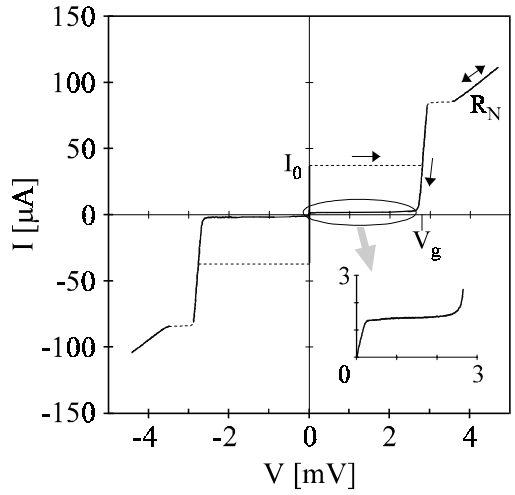

Figure 2.3 *Measured current vs. voltage characteristic of a 10 x 10 μm² Nb/Al,AlO$_x$/Al/Nb tunnel junction at T = 4.2 K. The inset gives an enlargement of the subgap region. The gap voltage of the junction is V_g = 2.8 mV. An external magnetic field was applied to suppress the critical current while recording the subgap.*

If the voltage is increased above V_g, this situation changes drastically. Then, electrons from the almost completely filled band below E_F in one electrode can tunnel to the almost empty energy band above E_F in the other electrode, as indicated by the large arrow in Fig. 2.2b. The result is a sharp increase of the quasiparticle tunnel current at $V = V_g$, as illustrated in Fig. 2.3, which shows the experimental current vs. voltage (*I*-*V*) characteristic of a Nb/Al,AlO$_x$/Al/Nb Josephson junction.

For voltages much larger than V_g, the *I*-*V* characteristic of a Josephson tunnel junction has an Ohmic character with a normal resistance R_N.

2.2.3 The RCSJ model for Josephson junctions

For quantitative analysis of circuitry containing Josephson junctions, the *RCSJ* (Resistively and Capacitively Shunted Junction) model, depicted schematically in Fig. 2.4, is widely used [4,5]. The cross symbolizes the Josephson element, which is described by Eqs. (2.2) and (2.3). The resistor R_j represents the non-linear resistance caused by tunneling of quasiparticles. Often, an additional shunt resistor is connected across a Josephson junction to modify its properties. In this case, R_j represents the effective resistance of the shunt resistor and the quasiparticle resistance. The junction capacitance, C_j, depends on the thickness and the dielectric constant of the barrier, and on the junction area.

The RCSJ model assumes that the phase difference ϕ between both superconducting electrodes is constant over the whole junction area, or, in

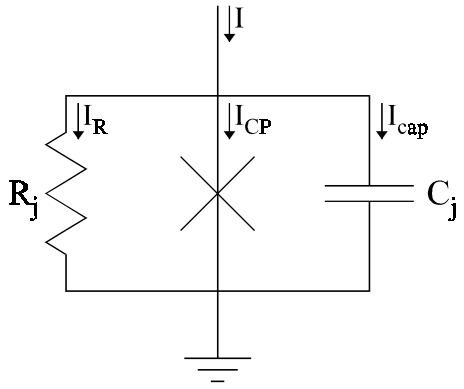

Figure 2.4 *The RCSJ representation of a Josephson tunnel junction. The cross symbolizes the Josephson element.*

other words, that the current flow is uniform. This is the case if no external magnetic field is applied to the junction and if the junction size is smaller than the *Josephson penetration depth* λ_J, which is given by [6]

$$\lambda_J = \sqrt{\frac{\hbar}{2e\mu_0 J_0 (2\lambda_L + d)}}\,. \tag{2.4}$$

Here, $\mu_0 = 4\pi\cdot 10^{-7}$ H/m represents the permeability of vacuum, J_0 is the critical current density and $2\lambda_L + d$ is the effective magnetic thickness of the barrier. For a typical Nb/Al junction with $J_0 = 100$ A/cm^2, Eq. (2.4) yields $\lambda_J \approx 40$ µm. As the typical junction size of the devices presented in this thesis is about one order of magnitude below this value, the RCSJ model is applicable.

Using the Josephson relations, the following circuit equations can be derived:

$$\begin{aligned} I &= I_R + I_{cap} + I_{CP} = \frac{V}{R_j} + C_j \frac{\partial V}{\partial t} + I_0 \sin\phi \\ &= \frac{1}{R_j}\cdot\frac{\hbar}{2e}\cdot\frac{\partial\phi}{\partial t} + C_j \frac{\hbar}{2e}\cdot\frac{\partial^2\phi}{\partial t^2} + I_0 \sin\phi\,. \end{aligned} \tag{2.5a}$$

Equation (2.5a) can be transformed to an energy equation by multiplying with a factor $\hbar/2e$:

$$\left(\frac{\hbar}{2e}\right)^2 \cdot \left(\frac{1}{R_j}\cdot\frac{\partial\phi}{\partial t} + C_j \frac{\partial^2\phi}{\partial t^2}\right) = -\frac{\partial E}{\partial\phi} \quad , \quad E = -\frac{\hbar I_0}{2e}\left(\frac{I}{I_0}\phi + \cos\phi\right). \tag{2.5b}$$

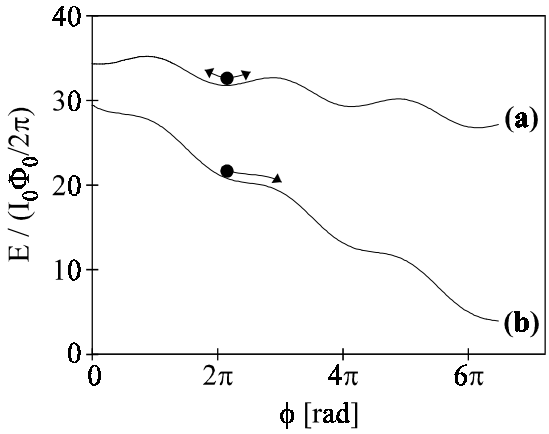

Figure 2.5 *The tilted washboard model with $I/I_0 = 0.4$* **(a)** *and $I/I_0 = 1.3$* **(b)**. *The ball moves through a viscous medium which causes damping of its motion.*

The factor $\hbar I_0/2e = I_0\Phi_0/2\pi$ in Eq. (2.5b) represents the *Josephson coupling energy* [3]. Equation (2.5b) can be interpreted with the mechanical analogue of a ball moving in a "tilted washboard" potential [1] E, see Fig. 2.5. In this analogue, E represents the potential energy of the ball, the position of the ball is given by ϕ, the voltage across the junction is proportional to the velocity $\partial\phi/\partial t$, the capacitance C_j corresponds to the mass of the ball, and the $1/R_j$ term represents the viscous damping of the motion. The relative tilt of the washboard is given by I/I_0.

If $|I| < I_0$, local potential wells exist in which the ball can be confined, as illustrated by trace (a) in Fig. 2.5. The trapped ball can oscillate back and forth around its equilibrium position at the bottom of the well. The frequency of these *plasma oscillations* is given by the plasma frequency f_p:

$$f_p = \sqrt{\frac{I_0}{2\pi\Phi_0 C_j}} \cdot \sqrt[4]{1-\left(\frac{I}{I_0}\right)^2}\,, \tag{2.6}$$

where the influence of R_j on f_p has been neglected. During the plasma oscillations, the average velocity of the ball (i.e. the voltage) is zero, implying that the junction is in the superconducting state. If the bias current exceeds the critical current, the potential wells in the washboard vanish, as illustrated by trace (b) in Fig. 2.5, and the ball starts to roll downhill. According to Eq. (2.3), the continuously increasing value of ϕ causes a voltage drop across the junction. If $I \gg I_0$, the speed of the ball is only determined by the $1/R_j$ damping term and consequently the junction is in the Ohmic regime.

When the junction is in the voltage state and the bias current is decreased to a value below the critical current, the moving ball can be trapped again in

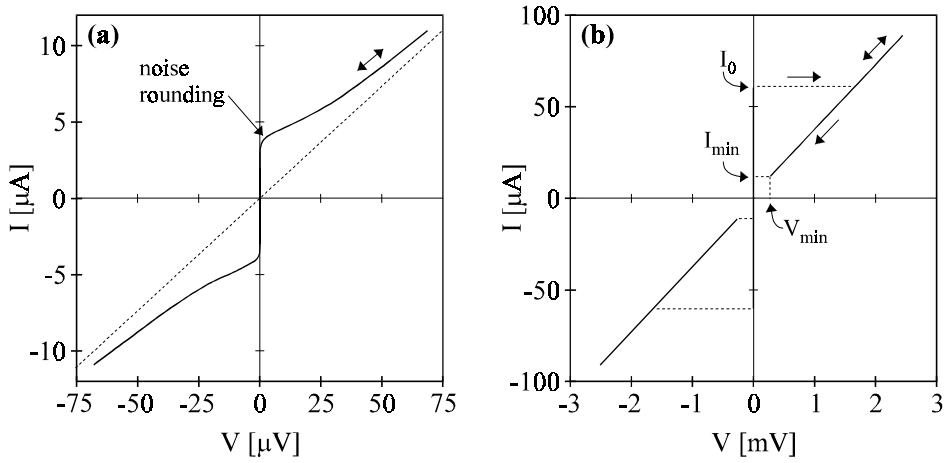

Figure 2.6 *Measured current vs. voltage characteristics of resistively shunted Nb/Al,AlO$_x$/Al/Nb tunnel junctions at T = 4.2 K.* **(a)** *Non-hysteretic junction with I_0 = 4 μA, R_{shunt} = 6.8 Ω and $\beta_C \approx 0.3$.* **(b)** *Hysteretic junction with I_0 = 60 μA, R_{shunt} = 28 Ω and $\beta_C \approx 50$.*

one of the potential wells, provided that the damping is large enough, i.e. that R_j is sufficiently small. The result is a non-hysteretic *I-V* characteristic, as shown in Fig. 2.6a. On the other hand, if the system is weakly damped (large R_j), the motion of the ball can persist at bias currents below the critical current. This causes a hysteretic *I-V* characteristic, like the one already shown in Fig. 2.3.

The value of the *McCumber parameter*, defined as

$$\beta_C = \frac{2\pi I_0 R_j{}^2 C_j}{\Phi_0}, \tag{2.7}$$

determines to which degree a junction shows hysteresis. If $\beta_C \ll 1$, the junction is non-hysteretic, and if $\beta_C \gg 1$, the junction has a hysteretic *I-V* characteristic. Between the two extreme situations of Fig. 2.3 and Fig. 2.6a, junctions with moderate hysteresis exist, see e.g. Fig. 2.6b.

In hysteretic Josephson junctions, the voltage state can only persist for bias currents larger than the *minimum return current*, I_{min}, indicated in Fig. 2.6b. Several expressions relating the minimum return current to the value of β_C can be found in the literature [7,8]. For $\beta_C \gg 1$,

$$I_{min} \approx \frac{4}{\pi\sqrt{\beta_C}} I_0 . \tag{2.8a}$$

When highly hysteretic junctions are considered, the concept of minimum return *voltage*, V_{min}, is more appropriate than the minimum return *current*. Using $V_{min} = I_{min} \cdot R_j$, the following expression can be derived from Eq. (2.8a):

$$V_{min} = I_{min} \cdot R_j = \frac{4}{\pi}\sqrt{\frac{I_0\Phi_0}{2\pi C_j}}\,. \tag{2.8b}$$

Note that R_j does not appear explicitly in the expression for V_{min}.

An alternative approach to derive an expression for V_{min} is the following. If a junction is biased at an average voltage V_{dc}, the ac Josephson current has an amplitude of I_0 and a frequency of $f_j = (2e/h)\cdot V_{dc}$. Neglecting the current through R_j and the non-harmonic character of the Josephson oscillations, the oscillating Josephson current causes an ac voltage across the capacitance C_j with an amplitude of $V_{ac} = I_0/(2\pi f_j C_j) = I_0\Phi_0/(2\pi C_j V_{dc})$. If $V_{ac} \approx V_{dc}$, the junction voltage approaches zero each oscillation period. Obviously, the junction can easily be trapped in the $V = 0$ state in this situation. Taking V_{min} to be that value of V_{dc} where $V_{dc} = V_{ac}$, one obtains $V_{min} = \sqrt{(I_0\Phi_0/2\pi C_j)}$, which is equal to Eq. (2.8b), apart from the factor $4/\pi$ (≈ 1.3).

2.2.4 Thermal noise in Josephson junctions

The discussion of the RCSJ model in the previous section did not include the effect of thermal noise. Like in any system, also the total energy of a Josephson junction, expressed by Eq. (2.5b), is subject to thermal fluctuations of the order $k_B T$, where $k_B = 1.38\cdot10^{-23}$ J/K is the Boltzmann constant. To prevent the junction dynamics from being wiped out by the thermal fluctuations, these fluctuations should be small compared to the Josephson coupling energy of $I_0\Phi_0/2\pi$. The ratio between the thermal energy and the Josephson coupling energy is expressed by the *noise rounding parameter* Γ:

$$\Gamma = \frac{k_B T}{I_0\Phi_0/2\pi} = \frac{2\pi k_B T}{I_0\Phi_0}\,. \tag{2.9}$$

Computer simulations indicate that for $\Gamma < 0.2$, the effect of thermal fluctuations is negligibly small [9]. In practice, often a "safer" criterion, namely $\Gamma < 0.05$, is used. At 4.2 K, the latter value of Γ implies a minimum critical current of 3.5 μA.

In hysteretic junctions, thermal fluctuations can cause a premature (i.e. at $I < I_0$) transition from the superconducting state to the voltage state, as will be discussed in detail in section 3.2. In non-hysteretic junctions, the thermal fluctuations can cause the ball to roll out of a potential minimum into the next one from time to time. If this happens, small voltage pulses, randomly spaced in time, are produced, which causes *noise rounding* of the *I-V* characteristic at $I \approx I_0$, like indicated in Fig. 2.6a.

In resistively shunted junctions, the Johnson noise generated by the shunt resistor R, having a spectral density S_I of

$$S_I = 4k_B T / R, \tag{2.10}$$

also contributes to the noise. This noise source can be modeled by adding a noise term to the bias current. In the mechanical analogue, the Johnson noise causes fluctuations in the tilt of the washboard. Hence, also the Johnson noise generated by the junction shunt resistor can cause the ball to escape from a potential well in the washboard at bias currents below I_0.

Equation (2.10) only holds in the classical limit $f < k_B T/h$, with f the frequency. All devices presented in this thesis operate within this limit. For devices operating at a very high frequency or at extremely low temperatures, Eq. (2.10) is no longer valid and *zero point fluctuations*, the quantum mechanical counterpart of Johnson noise, become important [10,11].

2.3 DC SQUIDs

Roughly speaking, SQUIDs can be divided into two families: rf SQUIDs and dc SQUIDs. An rf SQUID is based on only one Josephson junction whereas dc SQUIDs have two identical junctions. Until the early 1980's, the rf SQUID was widely used because the reproducible fabrication of two identical Josephson junctions was problematic. When production techniques became mature, the dc SQUID took the leading role because of its better sensitivity, although the discovery of the ceramic high T_c superconductors in 1986 renewed the interest for rf SQUIDs [12]. Since all devices in this thesis are based on low T_c dc SQUIDs, the discussion in this section will be restricted to these devices.

2.3.1 The threshold characteristic of a dc SQUID

Figure 2.7 shows a schematic picture of a dc SQUID, consisting of two identical Josephson junctions with a critical current I_0, connected in parallel by a superconducting loop with inductance L_{sq}. The junctions can be shunted with an external resistor R to remove the junction hysteresis. A dc bias current I_b - hence the name *dc* SQUID - is injected symmetrically into the SQUID loop. This bias current distributes over the two junctions:

$$I_b = I_1 + I_2 = I_0\left(\sin\phi_1 + \sin\phi_2\right), \tag{2.11}$$

where ϕ_1 and ϕ_2 represent the phases of both junctions.

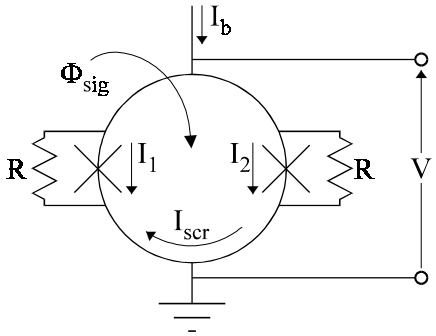

Figure 2.7 *Scheme of a dc SQUID. The Josephson junctions are represented by crosses, the shunt resistors are optional. The signal flux Φ_{sig} is applied to the superconducting SQUID loop.*

The superconducting SQUID ring has to comply with the flux quantization condition (section 2.1.2), taking into account the phases ϕ_1 and ϕ_2:

$$2\pi \frac{\Phi_{tot}}{\Phi_0} + \phi_1 - \phi_2 = n \cdot 2\pi \,. \tag{2.12}$$

In this equation, Φ_{tot} represents the total magnetic flux comprised by the SQUID loop, i.e. the sum of the applied signal flux Φ_{sig} and the flux caused by the circulating screening current I_{scr}:

$$\Phi_{tot} = \Phi_{sig} - L_{sq} \cdot I_{scr} \quad , \quad I_{scr} = \frac{I_2 - I_1}{2} \,. \tag{2.13}$$

If the signal flux Φ_{sig} equals $n \cdot \Phi_0$, no screening current flows in the SQUID loop and the bias current is divided symmetrically over the two junctions: $I_1 = I_2 = I_b/2$. In this case, the critical current I_c of the SQUID is just the sum of the critical currents of the junctions: $I_c(\Phi_{sig} = n \cdot \Phi_0) = 2I_0$. For other values of the flux, the screening current is non-zero, which causes an imbalance between I_1 and I_2. Therefore, the current through one of the junctions reaches its critical value already for $I_b < 2I_0$ and, consequently, the critical current of the SQUID is suppressed if $\Phi_{sig} \neq n \cdot \Phi_0$.

Qualitatively, the *I-V* characteristic of a hysteretic dc SQUID (having junctions with $\beta_C \gg 1$) looks like that of a single hysteretic Josephson junction, see e.g. Fig. 2.3. The large difference is that the critical current of the dc SQUID can be modulated with the signal flux Φ_{sig} which is applied to the SQUID loop. Figure 2.8 shows an experimental I_c-Φ_{sig} characteristic (*threshold*

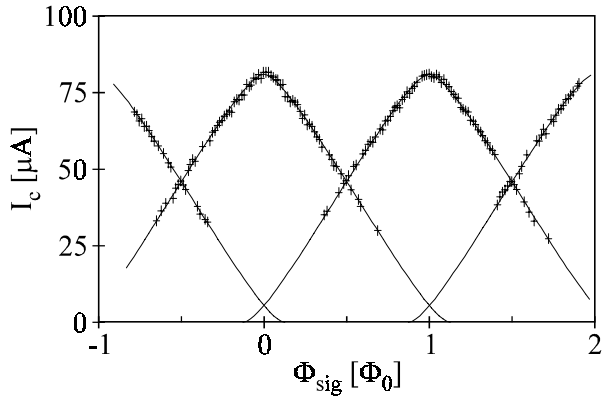

Figure 2.8 *Markers: experimental threshold characteristic of a hysteretic dc SQUID. The solid line gives a theoretical fit to the experimental data. From this fit, a SQUID inductance of L_{sq} = 32 pH (±10%) was deduced.*

curve) of a hysteretic dc SQUID. The characteristic was recorded by sweeping the signal flux at a slow rate (~0.1 Hz) while the bias current was swept from zero to ~100 μA at a considerably larger frequency (~100 Hz). The transition from $V = 0$ to $V = V_g$ was used to trigger an analogue-to-digital converter which measured both the bias current and the signal flux at the transition point. The solid line in Fig. 2.8 represents a theoretical fit to the measured data. The underlying model is based on Eqs. (2.11) to (2.13) [13].

The measurements in Fig. 2.8 show that $I_c(\Phi)$ is not single-valued if $\Phi_{sig} \approx (m+½)\cdot\Phi_0$. The reason is that for $\Phi_{sig} \approx (m+½+\delta)\cdot\Phi_0$, with $|\delta| \ll 1$, the value of the integer n in Eq. (2.12) can be either n = m or n = (m+1). If $\delta > 0$, the n = (m+1) state is energetically preferred since it corresponds to the smallest screening current, and, on the other hand, if $\delta < 0$, the n = m state is more likely to occur.

2.3.2 The non-hysteretic dc SQUID

Most low T_c dc SQUIDs are based on resistively shunted, non-hysteretic Josephson tunnel junctions. Figure 2.9a shows the schematic *I-V* characteristic of a non-hysteretic dc SQUID for two different values of the signal flux. If $\Phi_{sig} = n\cdot\Phi_0$, the critical current of the dc SQUID has its maximum value of $I_c = I_{c,max} = 2I_0$ and, on the other hand, if $\Phi_{sig} = (n+½)\cdot\Phi_0$, the critical current is minimum, viz. $I_c = I_{c,min}$.

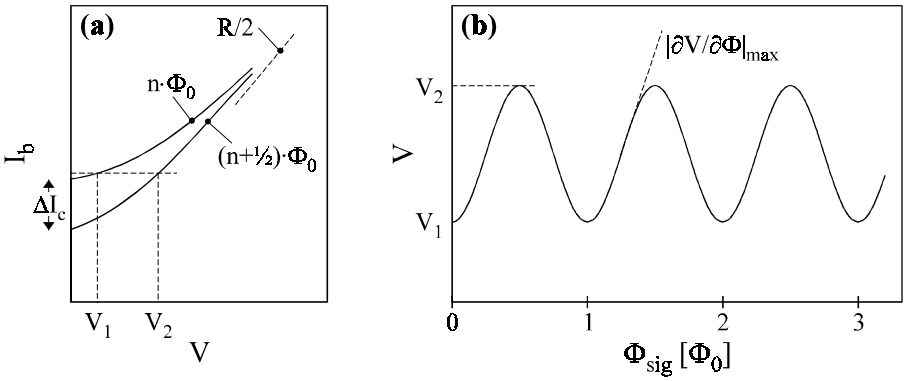

Figure 2.9 **(a)** *Schematic I_b-V and* **(b)** *V-Φ_{sig} characteristics of a non-hysteretic dc SQUID.*

The modulation depth ΔI_c of the critical current can be calculated as [13]

$$\Delta I_c = I_{c,max} - I_{c,min} \approx \frac{1}{1+\beta_L} \cdot 2I_0 \tag{2.14}$$

if the *screening parameter* β_L, defined as

$$\beta_L = \frac{2I_0 L_{sq}}{\Phi_0}, \tag{2.15}$$

is of the order of 10^0. The horizontal dotted line in Fig. 2.9a corresponds to a fixed bias current, slightly larger than the maximum critical current of the SQUID. If Φ_{sig} is varied, the voltage across the SQUID swings between V_1 and V_2. Thus, a current biased non-hysteretic dc SQUID is a flux-to-voltage converter. The corresponding voltage vs. flux characteristic is shown in Fig. 2.9b. From computer simulations, the maximum slope of the V-Φ_{sig} characteristic, generally referred to as the *flux-to-voltage transfer*, was derived to be [9]

$$\frac{\partial V}{\partial \Phi_{sig}} \approx \frac{2\beta_L}{1+\beta_L} \cdot \frac{R}{L_{sq}}. \tag{2.16}$$

For optimized dc SQUIDs, β_L should be close to unity [9], in which case Eq. (2.16) reduces to $\partial V/\partial \Phi_{sig} \approx R/L_{sq}$.

2.3.3 White noise in non-hysteretic dc SQUIDs

The main noise source in resistively shunted dc SQUIDs - at least at temperatures around 4.2 K - is the Johnson noise generated in the shunt resistors R, causing a voltage noise of

$$S_V = \gamma \cdot 2S_I \cdot \left(\frac{\partial V}{\partial I_b}\right)^2 \approx \gamma \cdot 2k_B TR \tag{2.17a}$$

at the output of the SQUID. In Eq. (2.17a), the dynamic resistance $\partial V/\partial I_b$ of the SQUID was approximated with $R/2$ and the noise of both shunt resistors was considered to be uncorrelated. The factor γ arises from the fact that Johnson noise, generated at frequencies around the Josephson frequency, is *mixed down* to lower frequencies by the Josephson oscillations and the inherent non-linearity of the junctions. Computer simulations showed that $\gamma \approx 8$ [9]. Dividing S_V by $(\partial V/\partial \Phi_{sig})^2$, the flux noise spectral density, S_Φ, can be derived:

$$S_\Phi = \frac{S_V}{\left(\partial V/\partial \Phi_{sig}\right)^2} \approx \gamma \cdot \frac{2k_B T L_{sq}^{\,2}}{R}, \tag{2.17b}$$

where β_L was set to unity. A typical low T_c dc SQUID, operating at 4.2 K, has a flux noise of the order of $\sqrt{S_\Phi} \approx 1\ \mu\Phi_0/\sqrt{\text{Hz}}$.

To compare the sensitivity of SQUIDs with different inductances, the *energy resolution* ε is commonly used :

$$\varepsilon = \frac{S_\Phi}{2L_{sq}} \approx \gamma \cdot k_B T \frac{L_{sq}}{R}. \tag{2.17c}$$

When deriving Eq. (2.17a), only the in-phase components of the Johnson noise currents generated by both shunt resistors were taken into account. The out-of-phase components induce a noise current I_N in the SQUID loop which generates a flux noise $\Phi_N = I_N \cdot L_{sq}$ [14]. For most applications, this effect is not important, and only in a few particular cases, e.g. when using a SQUID as a tuned radio frequency amplifier, it is significant. In this case, Φ_N induces a noise current in the tuned input circuit (*back action*), which current on its turn generates additional flux noise in the SQUID loop.

2.3.4 1/f noise in dc SQUIDs

At low frequencies, the flux noise spectral density of practical dc SQUIDs increases with a 1/f character. Two mechanisms for this 1/f noise have been identified, namely fluctuations of the critical current and motion of flux lines within the SQUID body [15].

The critical current fluctuations are caused by the presence of *energy traps* in the tunnel barriers of the junctions. When a tunneling electron is captured in one of these local energy wells, the critical current density changes. After a random time, the trapped electron is released, and the local critical current density is restored. The *telegraph noise* generated by the random trapping of electrons in several independent localized states in the barrier causes a 1/f-like noise spectrum. With high quality Josephson junctions, having low excess currents in the subgap region, this 1/f noise source can be reduced significantly. Moreover, specific modulation techniques, in which the SQUID is biased with an ac instead of a dc bias current, can be advantageous in reducing the 1/f noise due to critical current fluctuations [16,17].

The second origin of 1/f noise, the motion of trapped magnetic flux lines, is associated with the quality and microstructure of the material of the SQUID body. If a SQUID is placed in an ambient field, e.g. the earth's magnetic field (~ 50 μT), magnetic flux lines can penetrate the SQUID body, for instance at material defects. These flux lines cause a magnetic flux in the SQUID which changes when the flux lines move randomly from one pinning center to another. Since this noise manifests itself as "real" flux noise, it can not be reduced with modulation schemes. The motion of flux lines can be restricted by introducing strong pinning centers ("moats") in the SQUID body to trap the moving flux lines [18]. Another approach is to decrease the size of the superconducting structures in the SQUID body, so that the flux penetration in the superconducting material is strongly reduced [19].

2.4 DC SQUIDs in practical systems

2.4.1 DC SQUID readout: the flux locked loop

For many applications, the non-linear V-Φ_{sig} characteristic of a dc SQUID is not suitable. By using the SQUID as *null detector* in a feedback loop, its response can be linearized. Figure 2.10 shows a schematic diagram of such a *flux locked loop* (FLL) configuration.

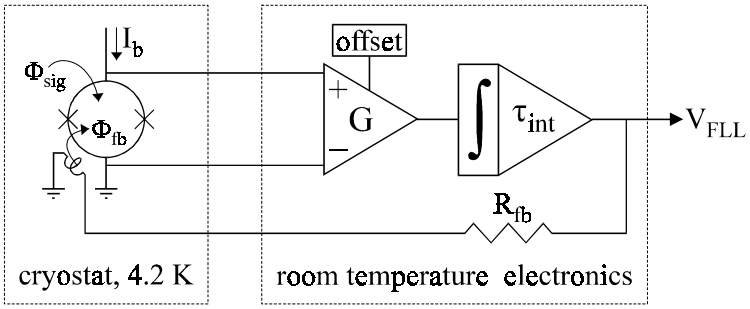

Figure 2.10 *Basic flux locked loop configuration without flux modulation.*

When a SQUID is operated in a FLL, in addition to the signal flux, a feedback flux (Φ_{fb}) is applied by means of a coil in the vicinity of the SQUID. The feedback loop keeps the output voltage of the SQUID, and hence the total flux $\Phi_{sig} + \Phi_{fb}$, constant. Thus, if the signal flux changes by an amount $\Delta\Phi_{sig}$, the feedback flux changes by an amount $\Delta\Phi_{fb} = -\Delta\Phi_{sig}$:

$$\Delta\Phi_{fb} = \frac{M_{fb}}{R_{fb}} \cdot \Delta V_{FLL} = -\Delta\Phi_{sig} \quad \rightarrow \quad \Delta V_{FLL} = -\frac{R_{fb}}{M_{fb}} \cdot \Delta\Phi_{sig} . \qquad (2.18)$$

As Eq. (2.18) shows, the dependence between the output voltage of the flux locked loop (V_{FLL}) and the input flux (Φ_{sig}) is linear and only dependent on the feedback parameters R_{fb} and M_{fb}.

The output voltage noise $\sqrt{S_V}$ of a dc SQUID at the flux locking point is given by $\sqrt{S_V} = \sqrt{S_\Phi} \cdot (\partial V/\partial\Phi)$. With $\sqrt{S_\Phi} = 1\ \mu\Phi_0/\sqrt{\text{Hz}}$ and $\partial V/\partial\Phi = 100\ \mu\text{V}/\Phi_0$, which are typical values for a dc SQUID operating at 4.2 K, this yields an output voltage noise of $\sqrt{S_V} = 0.1$ nV/$\sqrt{\text{Hz}}$. This is about one order of magnitude below the input voltage noise of a room temperature dc amplifier. Therefore, the FLL scheme of Fig. 2.10 leads to amplifier limitation of the system sensitivity. To overcome this situation, the FLL configuration of Fig. 2.11 is commonly used. In this scheme, a modulating flux with a peak-to-peak amplitude of $\frac{1}{2}\Phi_0$ is applied to the SQUID, usually via the same coil which is used for the feedback flux. This enables the use of ac impedance matching circuitry, e.g. a cooled resonant L-C circuit or a resonant step-up transformer, between the SQUID and the pre-amplifier [15]. An additional benefit of this flux modulated readout scheme is that the signal spectrum is shifted towards the sidebands of the modulation frequency, which eliminates the 1/f noise contribution of the pre-amplifier.

Various sophisticated modulation schemes, in which not only the flux, but also the bias current is modulated, have been developed [16,17]. With such *bias reversal* schemes, the 1/f noise generated by critical current fluctuations can be suppressed considerably, although the white noise level might increase slightly.

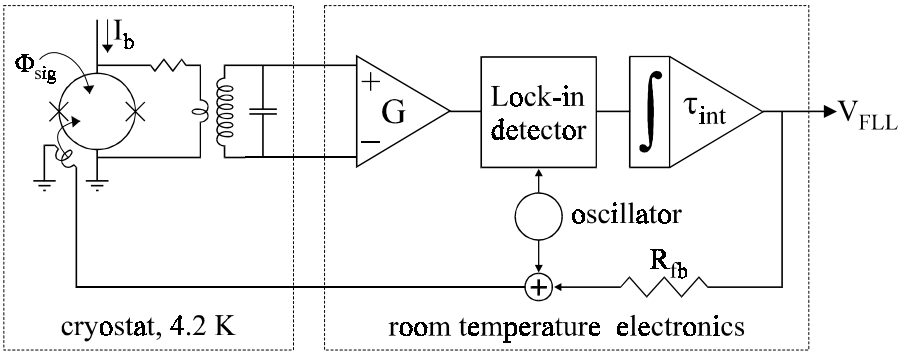

Figure 2.11 *Flux locked loop configuration with flux modulation and resonant step-up transformer.*

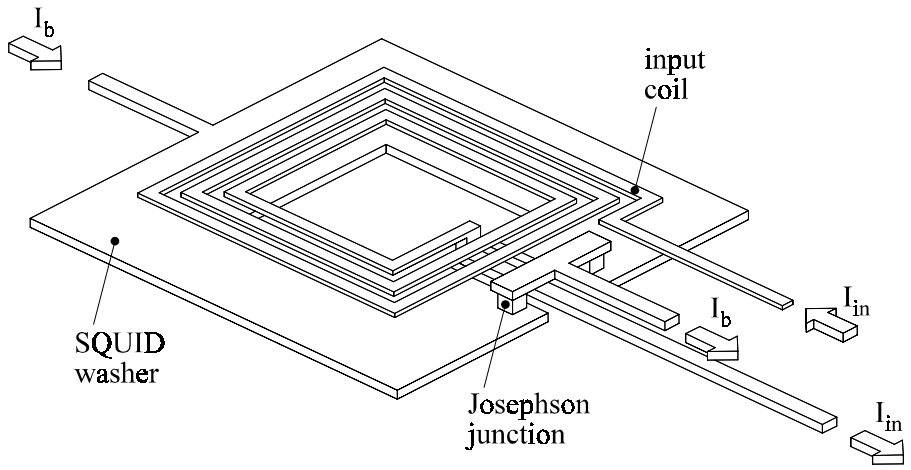

Figure 2.12 *Washer-type dc SQUID with integrated multi-turn input coil. The shunt resistors of the Josephson junctions are not indicated.*

2.4.2 The washer-type dc SQUID

At present, most high performance dc SQUIDs are made in thin film technology. A commonly used thin film configuration, the *washer-type* dc SQUID with tightly coupled input coil, is shown in Fig. 2.12. In this configuration, the SQUID inductance is composed of a square washer, which has an inductance of [20]

$$L_w = 1.25 \cdot \mu_0 \cdot d\,, \tag{2.19}$$

provided that the outer size of the washer is much larger than the hole width d, and that the thickness of the washer is at least $2\lambda_L$ to ensure a complete Meissner effect. The inductance of the slit in the washer, which also contributes to the total SQUID inductance, is not taken into account in Eq. (2.19). Typically, this slit inductance amounts to 0.3 .. 0.4 pH per µm length [21]. Generally, for low T_c materials like niobium, the kinetic inductance gives no major contribution to the total SQUID inductance [22].

The superconducting multi-turn input coil on top of the washer enables efficient coupling to the outside world. The inductance of the input coil, L_{in}, is given by [20]

$$L_{in} \approx n^2 L_w\,, \tag{2.20a}$$

with n the number of turns of the input coil.

The mutual inductance between the input coil and the SQUID inductance amounts to

$$M_{in} = k\sqrt{L_{in}L_{sq}} \approx k \cdot n \cdot L_w . \qquad (2.20b)$$

In practice, the coupling coefficient k can be close to unity, with typical values above 0.8.

To compare the sensitivity of dc SQUIDs with integrated input coils, the *coupled energy resolution* ε_{coupl} should be used instead of the intrinsic energy resolution ε [cf. Eq. (2.17c)] to account for different coupling efficiencies [23]:

$$\varepsilon_{coupl} = \frac{L_{in}S_I}{2} = \frac{L_{in}S_\Phi}{2M_{in}^2} = \frac{\varepsilon}{k^2} . \qquad (2.21)$$

In this equation, $S_I = S_\Phi/M_{in}^2$ represents the equivalent current noise spectral density referred to the input coil.

The parasitic capacitance between the SQUID washer and the input coil has a negative influence on the SQUID dynamics [24]. Moreover, standing waves can occur in the input coil due to its transmission line geometry. These resonance phenomena cause irregularities in the V-Φ_{sig} and I-V characteristics at voltages where the Josephson frequency is equal to one of the resonance frequencies. At these resonant points, the SQUID performance is degraded considerably. Therefore, proper damping of these resonances is essential. This can be achieved by adding an extra shunt resistor across the SQUID inductance to damp L-C oscillations in the SQUID loop [25], and by connecting an R-C shunt across the input coil to attenuate the microwave resonances in the input coil [26]. Recently, a novel solution, in which each turn of the input coil is shunted by a separate resistor (*intra coil damping*) was presented [27]. Another recent development is the use of distributed eddy current damping filters on top of the input coil [28]. Also, intermediate flux transformers can be used in order to decrease the size of the input coil, thus reducing the parasitic capacitance [24].

2.5 Second generation dc SQUIDs

Unfortunately, the flux modulated readout mode discussed in section 2.4.1 has some drawbacks. Usually, the matching circuitry is located near the SQUID, i.e. in the cryogenic environment. Especially in large multi-channel systems, as for instance used for bio-magnetism, careful screening is required to minimize the crosstalk between the matching transformers and the SQUIDs. This increases the complexity of the system, and thus the production costs, considerably. Furthermore, the bandwidth of a flux modulated FLL is limited by the modulation frequency, which is in the range 100 .. 500 kHz for most

systems, although a system operating at a modulation frequency of 16 MHz has been reported [29,30]. For some applications, such as the readout of X-ray detectors based on superconducting tunnel junctions [31], this restricted bandwidth is a serious disadvantage.

To allow flux locked loop operation with the simple direct voltage readout scheme of Fig. 2.10, several SQUID types with a larger flux-to-voltage transfer have been developed, and a few of them will be discussed below.

2.5.1 Two-stage SQUID systems

The transfer coefficient of a dc SQUID can be increased by using a second SQUID as a pre-amplifier. In such a configuration, the sensor SQUID can be optimized with respect to noise, whereas the readout SQUID can be designed to yield maximum output. Two-stage systems with a readout stage consisting of a series array of 100 to 200 dc SQUIDs [32] have been commercialized by HYPRES [33]. A schematic diagram of such a device is shown in Fig. 2.13.

A small resistor R_x (~50 mΩ) is used to bias the sensor SQUID at a constant voltage. The flux dependent current $I_{sens}(\Phi_{sig})$ generated by the sensor SQUID flows through the input coils of the SQUID array. If all SQUIDs in the array modulate coherently, their individual V-Φ characteristics add constructively, which results in a large voltage swing at the output.

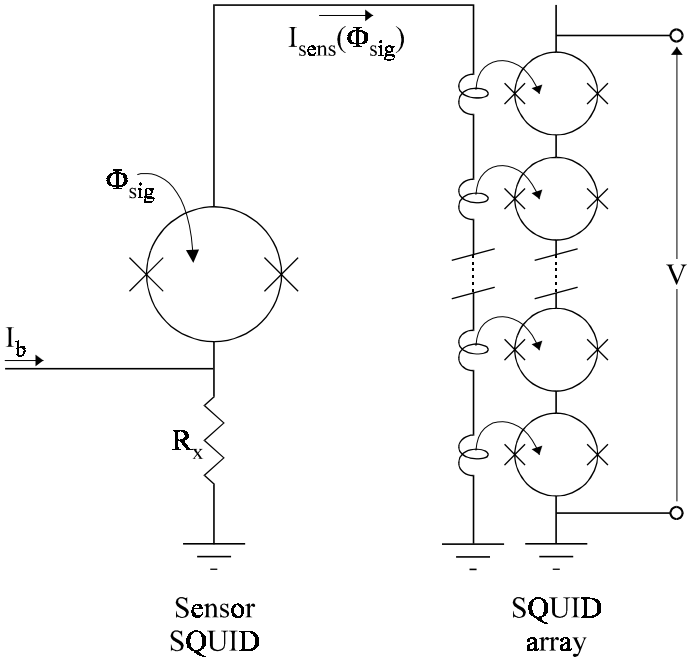

Figure 2.13 *Two-stage dc SQUID with a SQUID array as the second stage. The shunt resistors across the junctions are not shown.*

For devices like this, an output voltage swing of about 8 mV [34], a flux-to-voltage transfer of $\partial V_{out}/\partial\Phi_{sig} > 20$ mV/Φ_0 and a white energy resolution of $\varepsilon \approx 30\ h$ ($\varepsilon_{coupl} \approx 310\ h$) have been reported [32]. A disadvantage of the device is its susceptibility to flux trapping. If flux is trapped in the SQUIDs of the array, their V-Φ characteristics are shifted with respect to one another. As a result, the V-Φ curves no longer add constructively and the voltage modulation depth is decreased drastically.

2.5.2 SQUIDs with additional positive feedback

Another approach to increase the flux-to-voltage transfer is the dc SQUID with additional positive feedback (APF) [35], which is shown schematically in Fig. 2.14a. In the APF configuration, a non-hysteretic dc SQUID is shunted by a resistor R_{apf} and a coil L_{apf}, which is inductively coupled to the SQUID via a mutual inductance M_{apf}. Thus, in addition to the signal flux, a flux of $\Phi_{apf} = V\cdot(M_{apf}/R_{apf})$ is applied to the SQUID. Consequently, the V-Φ_{sig} characteristic is skewed and it becomes steeper at one flank, as illustrated in Fig. 2.14b.

The values of R_{apf} and M_{apf} should be within fairly tight limits. If the APF gain is too low, the flux-to-voltage transfer is not increased sufficiently. On the other hand, if the APF gain is too high, the V-Φ_{sig} characteristic becomes hysteretic. Several ways to adjust the APF gain have been reported, for instance the use of a cooled GaAs FET instead of a fixed APF resistor [36], or the integration of an on-chip resistor network, allowing to trim R_{apf} with Al bonding wires [35] or with laser trimming.

Flux-to-voltage transfer coefficients of several mV/Φ_0, as well as a white energy sensitivity of $\varepsilon = 36\ h$ have been reported for low T_c APF SQUIDs. With a 7.2 x 7.2 mm^2 directly coupled multi-loop APF magnetometer, a magnetic field noise of $\sqrt{S_B} = 1$ fT/$\sqrt{\text{Hz}}$ (2 fT/$\sqrt{\text{Hz}}$ @ 1 Hz) was achieved [37]. Also, wideband APF systems with a bandwidth up to 11 MHz and a maximum slew rate of $5\cdot10^7\ \Phi_0$/s have been developed [38,39].

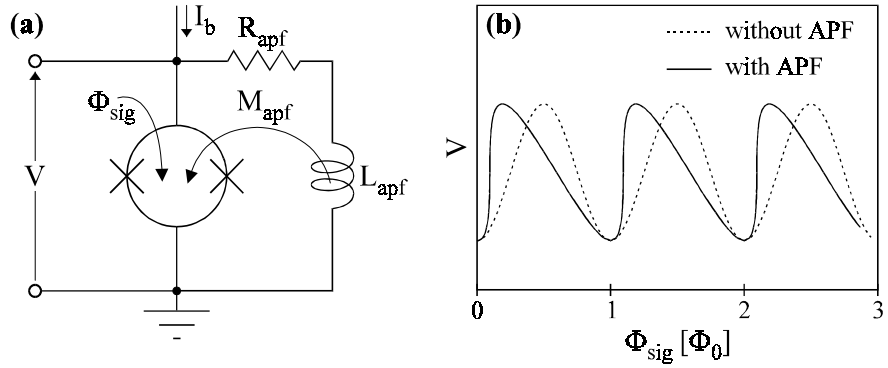

Figure 2.14 (a) *Schematic picture and* **(b)** *V-Φ_{sig} characteristic of a dc SQUID with additional positive feedback. The junction shunt resistors are not shown.*

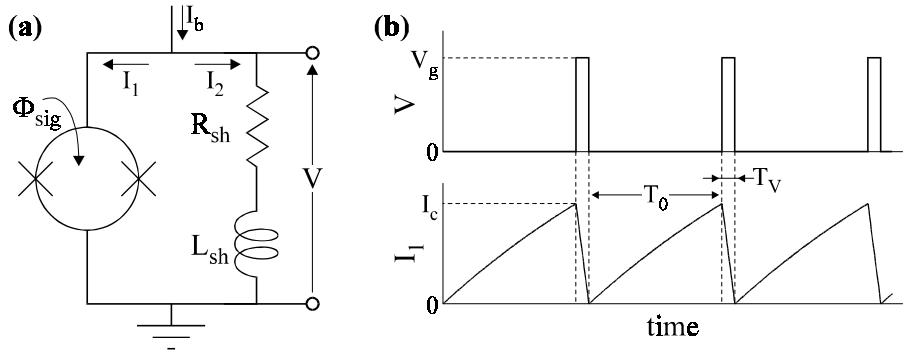

Figure 2.15 (a) *Scheme of a relaxation oscillation SQUID (ROS).* **(b)** *I_1-t and V-t traces of a current biased ROS.*

2.5.3 Relaxation oscillation SQUIDs

As Fig. 2.15a shows, a relaxation oscillation SQUID (ROS) consists of a hysteretic dc SQUID, shunted by a resistor R_{sh} and an inductor L_{sh}, which is not magnetically coupled to the SQUID. If a ROS is biased with an appropriate dc bias current $I_b > I_c(\Phi_{sig})$, *relaxation oscillations* are generated [40,41]. A thorough discussion of the dynamics of the ROS will be given in chapter 3, the discussion in this section is restricted to a simple model to clarify its principle of operation.

Let us assume that at a time $t = 0$ the current I_1 through the SQUID branch is zero, so that the SQUID is in the superconducting state. Since $I_1 + I_2 = I_b$ and $I_1 = 0$, it follows that $I_2 = I_b$. Because $V = 0$, the current I_2 decays exponentially with a time constant L_{sh}/R_{sh}. Consequently, I_1 increases, as is indicated in Fig. 2.15b. After a time T_0, given by [41]

$$T_0 = \frac{L_{sh}}{R_{sh}} \ln\left(\frac{I_b}{I_b - I_c\left(\Phi_{sig}\right)}\right), \tag{2.22a}$$

the current through the hysteretic dc SQUID reaches its critical value $I_c(\Phi_{sig})$, and the SQUID switches to the gap voltage V_g.

In the presence of the voltage $V = V_g$, the current I_2 through the L_{sh}-R_{sh} shunt increases again, and consequently the current through the SQUID, I_1, decreases. After having spent a time T_V, given by [41]

$$T_V = \frac{L_{sh}}{R_{sh}} \ln\left(1 + \frac{R_{sh} I_c\left(\Phi_{sig}\right)}{V_g - R_{sh} I_b}\right), \tag{2.22b}$$

in the voltage state, the current through the SQUID has decayed to zero, the SQUID switches back to the superconducting state, and the whole cycle starts again, as shown in Fig. 2.15b.

As a result of the relaxation oscillation process, voltage pulses with an amplitude V_g and a frequency f_{RO} of

$$f_{RO} = \frac{1}{T_0 + T_V} \approx \frac{1}{T_0} \tag{2.23}$$

are generated at the ROS output. The right-hand approximate expression in Eq. (2.23) is justified by the fact that, generally, $T_0 \gg T_V$.

Since both T_0 and T_V depend on the critical current of the dc SQUID, f_{RO} is a function of the applied flux, which makes a ROS a *flux-to-frequency converter*. Because T_0 and T_V have a different dependence on $I_c(\Phi_{sig})$, the time-averaged voltage $<V>$ across the ROS, calculated as

$$< V > = \frac{T_V}{T_0 + T_V} V_g , \tag{2.24}$$

is also modulated by the signal flux. Consequently, a ROS can be used either in frequency or in voltage readout mode. However, as will be shown in chapter 3, the flux-to-voltage transfer of a ROS with voltage readout is comparable to that of a standard non-hysteretic dc SQUID, which implies that a ROS with voltage readout does not have significant advantages compared to standard dc SQUIDs. Therefore, frequency readout is the appropriate readout scheme for a ROS.

The sensitivity of a ROS depends on the relaxation frequency. Typically, optimum noise performance is achieved at a relaxation frequency around 1 GHz.

Various uncoupled ROSs have been presented in literature, with relaxation frequencies ranging from a few MHz [42,43] to 7 GHz [40,44]. The best reported energy sensitivity, measured in a FLL with frequency readout at room temperature, is $\varepsilon \approx 600\ h$ [40].

2.5.4 Double relaxation oscillation SQUIDs

Figure 2.16a shows a schematic diagram of a double relaxation oscillation SQUID (DROS). Contrary to the ROS, which is operated with frequency readout, the DROS is designed for direct voltage readout. In a DROS, the external L_{sh}-R_{sh} circuit shunts two hysteretic dc SQUIDs, the *signal SQUID* and the *reference SQUID*. The signal flux Φ_{sig} is applied to the signal SQUID, whereas a constant reference flux Φ_{ref} is applied to the reference SQUID. In a predecessor of the DROS, the signal flux was applied to both SQUIDs. However, this device, the *balanced ROS* [45], will not be discussed here. By tuning Φ_{ref}, the critical current of the reference SQUID can be adjusted to a

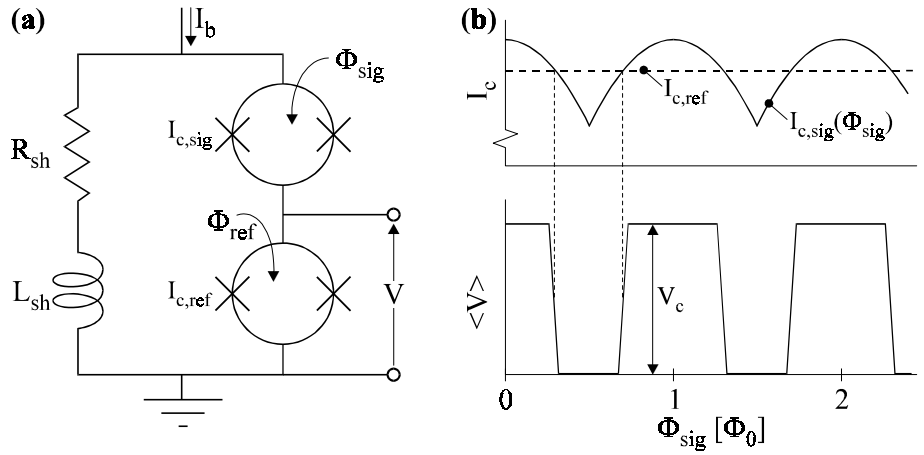

Figure 2.16 (a) *Scheme of a double relaxation oscillation SQUID (DROS).* **(b)** *I_c-Φ_{sig} and <V>-Φ_{sig} graphs for a DROS.*

value in the middle of the critical current modulation range of the signal SQUID, as indicated in the schematic I_c-Φ_{sig} graph in Fig. 2.16b.

If a DROS is biased with a dc bias current, relaxation oscillations are generated under the same conditions as for a ROS. The main difference with a ROS is that a DROS acts as a *critical current comparator*. Only the SQUID with the smallest critical current participates in the relaxation oscillations, while the other SQUID remains superconducting. As a consequence, the output voltage, which is measured across the reference SQUID, equals zero when $I_{c,sig}(\Phi_{sig}) < I_{c,ref}$. On the other hand, when the signal flux is changed in such a way that $I_{c,sig}(\Phi_{sig}) > I_{c,ref}$, voltage pulses with a frequency f_{RO} arise at the DROS output. If an amplifier with a bandwidth considerably smaller than f_{RO} is used for readout, only the time-averaged dc component $\langle V \rangle = V_c$ of these pulses is measured. The resulting $\langle V \rangle$-Φ_{sig} characteristic has a modulation depth V_c and a large flux-to-voltage transfer at the points where $I_{c,ref} = I_{c,sig}(\Phi_{sig})$, as sketched in the lower trace of Fig. 2.16b.

As for a ROS, the optimum relaxation frequency for a DROS is typically 1 GHz [41]. Typical values for the flux-to-voltage transfer are in the order of $\partial V/\partial \Phi_{sig} \approx 1$ mV/Φ_0 and the best intrinsic energy resolution reported for an uncoupled DROS is $\varepsilon = 13\,h$ (34 h in FLL) [46]. The best reported energy sensitivity of a DROS with an integrated input coil is $\varepsilon \approx 150\,h$ in FLL ($\varepsilon_{coupl} \approx 300\,h$) [47]. In chapter 4, the DROS will be discussed in more detail.

References

[1] M. Tinkham, *Introduction to superconductivity*, McGraw-Hill International Editions, New York etc., 2nd edition (1996).

[2] B.W. Petley, *An Introduction to the Josephson Effects*, Mills & Boon Ltd., London (1971).

[3] B.D. Josephson, "Possible new effects in superconductive tunneling", *Phys. Lett.* **1,** 251-253 (1962).

[4] W.C. Stewart, "Current-voltage characteristics of Josephson junctions", *Appl. Phys. Lett.* **12**, 277-280 (1968).

[5] D.E. McCumber, "Effect of ac impedance on dc voltage-current characteristics of superconductor weak-link junctions", *J. Appl. Phys.* **39**, 3113-3118 (1968).

[6] J.R. Waldram, A.B. Pippard and J. Clarke, "Theory of the current-voltage characteristics of SNS junctions and other superconducting weak links", *Phil. Trans. Roy. Soc. Lond.* A **268**, 265-287 (1970).

[7] H.H. Zappe, "Minimum current and related topics in Josephson tunnel junction devices", *J. Appl. Phys.* **44**, 1371-1377 (1972).

[8] A.T. Johnson, C.J. Lobb and M. Tinkham, "Effect of leads and energy gap upon the retrapping current of Josephson junctions", *Phys. Rev. Lett.* **65**, 1263-1266 (1990).

[9] C.D. Tesche and J. Clarke, "DC SQUID: noise and optimization", *J. Low Temp. Phys.* **29**, 301-331 (1977); J.J.P. Bruines, V.J. de Waal and J.E. Mooij, "Comment on: 'DC SQUID: noise and optimization' by Tesche and Clarke", *J. Low Temp. Phys.* **46**, 383-386 (1982).

[10] R.H. Koch, D.J. van Harlingen, J. Clarke, "Quantum-noise theory for the resistively shunted Josephson junction", *Phys. Rev. Lett.* **45**, 2132-2135 (1980).

[11] C.W. Gardner, *Quantum Noise*, Springer-Verlag, Berlin / Heidelberg (1991).

[12] Y. Zhang, N. Wolters, X.H. Zeng, J. Schubert, W. Zander, H. Soltner, M. Banzet, F. Rüders and A.I. Braginski, "Washer rf SQUID magnetometers with coplanar resonators at 77 K", in *extended abstracts ISEC'97 conference*, ed. H. Koch and S. Knappe, P.T.B. Braunschweig, 51-53 (1997).

[13] R.L. Peterson and C.A. Hamilton, "Analysis of threshold curves for superconducting interferometers", *J. Appl. Phys.* **50**, 8135-8142 (1979).

[14] C.D. Tesche and J. Clarke, "DC SQUID: current noise", *J. Low Temp. Phys.* **37**, 397-403 (1979).

[15] J. Clarke, "SQUID fundamentals", in *SQUID Sensors: Fundamentals, Fabrication and Applications*, ed. H. Weinstock, NATO ASI Series **329**, Kluwer Academic Publishers, Dordrecht / Boston / London (1996).

[16] R.H. Koch, J. Clarke, J.M. Martinis, W.M. Goubau, C.M. Pegrum and D.J. van Harlingen, "Investigation of 1/f noise in tunnel junction dc SQUIDs", *IEEE Trans. Magn.* **19**, 449-452 (1983).

[17] V. Foglietti, W.J. Gallagher, M.B. Ketchen, A.W. Kleinsasser, R.H. Koch, S.I. Raider and R.L. Sandstrom, "Low-frequency noise in low 1/f noise dc SQUID's", *Appl. Phys. Lett.* **49**, 1393-1395 (1986).

[18] M. Jeffery, T. Van Duzer, J.R. Kirtley and M.B. Ketchen, "Magnetic imaging of moat-guarded superconducting electronic circuits", *Appl. Phys. Lett.* **67**, 1769-1771 (1995).

[19] E. Dantsker, S. Tanaka and J. Clarke, "High-T_c superconducting quantum interference devices with slots or holes: Low 1/f noise in ambient magnetic fields", *Appl. Phys. Lett.* **70**, 2037-2039 (1997).

[20] J.M. Jaycox and M.B. Ketchen, "Planar coupling scheme for ultra low noise dc SQUIDs", *IEEE Trans. Magn.* **17**, 400-403 (1981).

[21] M.B Ketchen, “Design considerations for dc SQUIDs fabricated in deep sub-micron technology”, *IEEE Trans. Magn.* **27**, 2916-2919 (1991).
[22] R. Cantor, “DC SQUIDs: design, optimization and practical applications”, in *SQUID Sensors: Fundamentals, Fabrication and Applications*, ed. H. Weinstock, NATO ASI Series **329**, Kluwer Academic Publishers, Dordrecht / Boston / London (1996).
[23] J.H. Claassen, “Coupling considerations for SQUID devices”, *J. Appl. Phys.* **46**, 2268-2275 (1975).
[24] J. Knuutila, M. Kajola, H. Seppä, R. Mutikainen and J. Salmi, “Design, optimization, and construction of a dc SQUID with complete flux transformer circuits”, *J. Low Temp. Phys.* **71**, 369-392 (1988).
[25] K. Enpuku, K. Sueoka, K. Yoshida and F. Irie, “Effect of damping resistance on voltage versus flux relation of a dc SQUID with large inductance and critical current”, *J. Appl. Phys.* **57**, 1691-1697 (1985).
[26] K. Enpuku, R. Cantor and H. Koch, “Modeling the direct current superconducting quantum interference device coupled to the multiturn input coil. II.”, *J. Appl. Phys.* **71**, 2338-2346 (1992).
[27] R.H. Ono, J.A. Koch, A. Steinbach, M.E. Huber and M.W. Cromar, “Tightly coupled dc SQUIDs with resonance damping”, *IEEE Trans. Appl. Supercond.* **7**, 2538-2541 (1997).
[28] I. Jin, A. Amar and F.C. Wellstood, “Distributed microwave damping filters for superconducting quantum interference devices”, *Appl. Phys. Lett.* **70**, 2186-2188 (1997).
[29] R.H. Koch, J.R. Rozen, P. Wöltgens, T. Picunko, W.J. Goss, D. Gambrel, D. Lathrop, R. Wiegert and D. Overway, “High performance superconducting quantum interference device feedback electronics”, *Rev. Sci. Instrum.* **67**, 2968-2976 (1996).
[30] R.D. Penny, D.K. Lathrop, B.D. Thorson, B.R. Whitecotton, R.H. Koch and J.R. Rozen, “Wideband front end for high-frequency SQUID electronics”, *IEEE Trans. Appl. Supercond.* **7**, 2323-2326 (1997).
[31] N.E. Booth and D.J. Goldie, “Superconducting particle detectors”, *Supercond. Sci. Technol.* **9**, 493-516 (1996).
[32] R.P. Welty and J.M. Martinis, “Two-stage integrated SQUID amplifier with series array output”, *IEEE Trans. Appl. Supercond.* **3**, 2605-2608 (1993).
[33] HYPRES Inc., 175 Clearbrook Road, Elmsford, NY 10523, U.S.A.
[34] http://www.hypres.com/~masoud/array.shtml
[35] D. Drung and H. Koch, “An integrated dc SQUID magnetometer with variable additional positive feedback”, *Supercond. Sci. Technol.* **7**, 242-245 (1993).
[36] H. Seppä, A. Ahonen, J. Knuutila, J. Simola and V. Vilkman, “DC SQUID electronics based on adaptive positive feedback: experiments”, *IEEE Trans. Magn.* **27**, 2488-2490 (1991).
[37] D. Drung, “Advanced SQUID read-out electronics”, in *SQUID Sensors: Fundamentals, Fabrication and Applications*, ed. H. Weinstock, NATO ASI Series **329**, Kluwer Academic Publishers, Dordrecht / Boston / London (1996).
[38] D. Drung, T. Radic, H. Matz and H. Koch, “A 2-channel wideband SQUID system for high-frequency geophysical applications”, *IEEE Trans. Appl. Supercond.* **7**, 3283-3286 (1997).
[39] D. Drung, H. Matz and H. Koch, “A 5-MHz bandwidth SQUID magnetometer with additional positive feedback”, *Rev. Sci. Instrum.* **66**, 3008-3015 (1995).
[40] M.J. van Duuren, D.J. Adelerhof, G.C.S. Brons, J. Kawai, G. Uehara, H. Kado, J. Flokstra and H. Rogalla, “Frequency readout of relaxation oscillation superconducting quantum interference devices in the GHz regime”, *J. Appl. Phys.* **80**, 4164-4173 (1996).
[41] D.J. Adelerhof, H. Nijstad, J. Flokstra and H. Rogalla, “(Double) relaxation oscillation SQUIDs with high flux-to-voltage transfer: Simulations and experiments”, *J. Appl. Phys.* **76**, 3875-3886 (1994).

[42] M. Mück, H. Rogalla and C. Heiden, “A frequency-modulated read-out system for dc SQUIDs”, *Appl. Phys.* A **47**, 285-289 (1988).
[43] M. Mück and C. Heiden, “Simple dc SQUID system based on a frequency modulated relaxation oscillator”, *IEEE Trans. Magn.* **25**, 1151-1153 (1989).
[44] G. Uehara, T. Morooka, J. Kawai, N. Mizutani and H. Kado, “Characteristics of the relaxation oscillating SQUID with tunnel junctions”, *IEEE Trans. Appl. Supercond.* **3**, 1866-1869 (1993).
[45] S.A. Gudoshnikov, Y.V. Maslennikov, V.K. Semenov, O.V. Snigirev and A.V. Vasiliev, “Relaxation-oscillation-driven dc SQUIDs”, *IEEE Trans. Magn.* **25**, 1178-1181 (1989).
[46] D.J. Adelerhof, J. Kawai, G. Uehara and H. Kado, “High sensitivity double relaxation oscillation superconducting quantum interference devices”, *Appl. Phys. Lett.* **65**, 2606-2608 (1994).
[47] M.J. van Duuren, G.C.S. Brons, D.J. Adelerhof, J. Flokstra and H. Rogalla, “Double relaxation oscillation superconducting quantum interference devices with gradiometric layout”, *J. Appl. Phys.* **82**, 3598-3606 (1997).

Chapter 3

Relaxation Oscillation SQUIDs

In the previous chapter, the relaxation oscillation SQUID (ROS) was introduced as a flux-to-frequency converter, and its operation was illustrated with a simple model. However, the actual behaviour of a ROS can deviate considerably from this model, especially at high relaxation frequencies. This is mainly due to the dynamic behaviour of the Josephson junctions, which was not taken into account in the discussion of section 2.5.3.

In this chapter, a more thorough study of the ROS dynamics is presented. In section 3.1, numerical simulations are used to study the operation of a ROS in more detail. The sensitivity of the ROS is the subject of section 3.2. As the theoretical discussion in that section will show, the sensitivity of a ROS is comparable to that of a standard non-hysteretic dc SQUID if the relaxation frequency is about 1 GHz. In order to verify the models developed in sections 3.1 and 3.2, the experimental characteristics of more than ten different ROSs have been recorded. These measurements and the subsequent model verification are described in section 3.3. In the same section, a flux locked loop based on frequency readout of ROSs is presented. This chapter is concluded with a discussion concerning the practical feasibility of SQUID systems based on ROSs.

3.1 Extended ROS model

3.1.1 The ROS in the single junction approximation

In this section, the dynamics of the ROS will be studied by means of numerical simulations. Figure 3.1a shows a schematic overview of a ROS. In order to reduce the complexity of the calculations, the hysteretic dc SQUID was modeled as a single RCSJ-junction with a capacitance $C_{sq} = 2C_j$, C_j being the

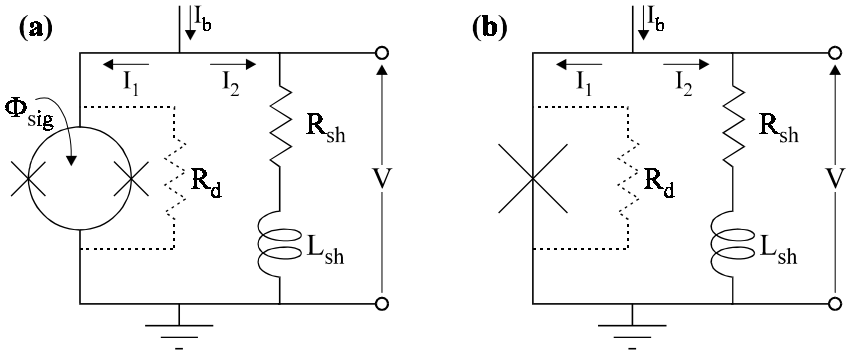

Figure 3.1 **(a)** *Schematic representation of a ROS and* **(b)** *the model of a ROS in the single junction approximation.*

capacitance of one junction, and with a critical current $I_c = I_c(\Phi_{sig})$. This *single junction approximation* is allowed when the phases of the two Josephson junctions are tightly coupled, which is the case in the limit $\beta_L \rightarrow 0$. In reference [1], it is shown that the single junction approximation can be used for practical engineering purposes if $\beta_L < 2/\pi$. Even for larger values of β_L, the deviations remain small.

The scheme of Fig. 3.1b, representing a ROS in the single junction approximation, was implemented in the simulation program JSIM [2]. A typical simulation result is shown in Fig. 3.2a. The simulation parameters are listed in the figure caption. In contrast to the simple model which was presented in the previous chapter, the switching process from the voltage state to the superconducting state is no longer well defined due to resonances in the L-C circuit constituted by L_{sh} and C_{sq}. As a result of these L_{sh}-C_{sq} resonances, the current I_1 is swept through zero at such a high rate that the junction fails to lock to the zero-voltage state immediately, a phenomenon known as *punchthrough* [3,4].

As the simulations in Fig. 3.2a show, the number of L_{sh}-C_{sq} swings before switching back to the superconducting state varies from cycle to cycle, which is caused by the random phase difference between the L_{sh}-C_{sq} oscillations and the Josephson oscillations. Obviously, the spread in the relaxation frequency caused by this stochastic switching behaviour limits the sensitivity of a ROS.

Figure 3.2b displays one of the relaxation pulses in detail. In this particular cycle, the junction switches back to the superconducting state only the third time the voltage crosses zero. The corresponding path in the I_1-V characteristic (inset 1 of Fig. 3.2b) shows this effect as consecutive swings around the origin. The plasma oscillations after entering the superconducting state are also clearly visible in Fig. 3.2b. At the onset of the next relaxation oscillation cycle, the plasma oscillations have not faded away completely, which causes the junction to switch to the voltage state already at $I_1 < I_c$. This effect also induces noise in the relaxation oscillation scheme.

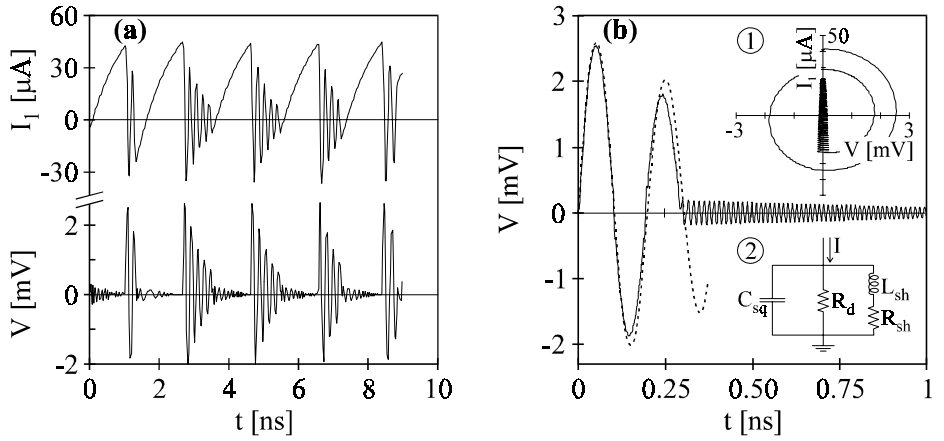

Figure 3.2 **(a)** *Numerical simulation of the relaxation oscillations in a ROS without damping resistor R_d. Simulation parameters: L_{sh} = 2 nH, R_{sh} = 2 Ω, C_{sq} = 0.5 pF, I_c = 45 μA, V_g = 2.75 mV and I_b = 70 μA. The dc SQUID was modeled as a single junction.* **(b)** *Enlargement of one of the pulses in figure (a). The dotted line gives the step response of the equivalent circuit shown in inset 2. Inset 1 shows the I_1-V path which is followed during the relaxation oscillations.*

To investigate the L_{sh}-C_{sq} resonances in more detail, the ROS was modeled with the L-C-R circuit depicted in inset 2 of Fig. 3.2b. This circuit describes the system during the voltage state, neglecting the ac Josephson current. The resistor R_d represents the subgap resistance of the Josephson junction, which was 750 Ω in the present simulation. In this L-C-R system, the transition from the superconducting to the normal state can be modeled as a current step from $I = I_b - I_c$ to $I = I_b$, with initial condition $V = 0$. The calculated voltage response of the L-C-R circuit is plotted with a dotted line in Fig. 3.2b.

3.1.2 ROS with additional damping resistor

The random switching process from the voltage state to the zero-voltage state, observed in the simulations of section 3.1.1, limits the sensitivity of a ROS. Therefore, damping of the L_{sh}-C_{sq} resonances, for instance with an additional damping resistor R_d shunting the dc SQUID as shown in Fig. 3.1, is crucial. If

$$\frac{\left(R_{sh}R_dC_{sq}+L_{sh}\right)^2}{4L_{sh}C_{sq}R_d\left(R_d+R_{sh}\right)} \approx \frac{L_{sh}}{4C_{sq}R_d^2} > 1 \quad \Leftrightarrow$$

$$D = \frac{L_{sh}}{4C_{sq}R_d^2} > 1\,, \tag{3.1}$$

the circuit is overdamped and L_{sh}-C_{sq} resonances can not occur. Typically, $R_d > R_{sh}$ and $R_d C_{sq} < L_{sh}/R_{sh}$, which justifies the approximation in Eq. (3.1). The dimensionless parameter D introduced in Eq. (3.1) is the *damping parameter* of the ROS. Figures 3.3a and 3.3b show numerical simulations of the same ROS as that of Fig. 3.2, but now with a damping resistor of $R_d = 25\ \Omega$ ($D = 1.6$). In this well damped ROS, the switching process to the zero-voltage state occurs in a much more controlled way.

Not only the L_{sh}-C_{sq} resonances, but also the plasma oscillations after the transition to the superconducting state are damped by R_d. As the inset of Fig. 3.3b shows, in the damped ROS, the plasma oscillations have faded away completely before the next relaxation oscillation cycle starts. Hence, the transition to the voltage state occurs exactly at $I_1 = I_c = 45\ \mu A$ and not at a current slightly smaller than I_c, as in the underdamped case of Fig. 3.2. This side effect of the damping resistor R_d also contributes positively to the sensitivity of the ROS.

The dotted line in Fig. 3.3b indicates the step response of the equivalent L-C-R circuit. The circuit no longer oscillates and the voltage decays exponentially to a value V_∞, given by

$$V_\infty = I_b \frac{R_{sh} R_d}{R_{sh} + R_d} \approx I_b R_{sh} . \tag{3.2}$$

But, before $V = V_\infty$, the voltage reaches the minimum return voltage V_{min} [Eq. (2.8b)] and the ROS switches back to the zero-voltage state. Since I_1 does not decay entirely to zero, but to $I_1 = I_{min}$ [Eq. (2.8a)], the duration of the zero-

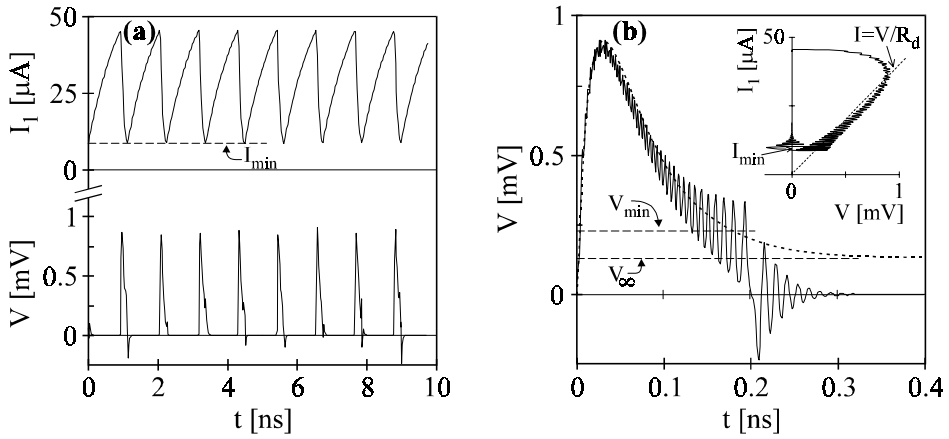

Figure 3.3 **(a)** *Numerical simulation of the relaxation oscillations in a ROS with a damping resistor $R_d = 25\ \Omega$ ($D = 1.6$). The other simulation parameters are as in Fig. 3.2.* **(b)** *Detailed view of one of the pulses in figure (a). The dotted line indicates the step response of the L-C-R circuit of inset 2 in Fig. 3.2b.*

voltage state, T_0, is shorter than the value obtained from Eq. (2.22a). The adjusted expression for T_0 is [5]

$$T_0 = \frac{L_{sh}}{R_{sh}} \ln\left(\frac{I_b - I_{min}}{I_b - I_c\left(\Phi_{sig}\right)}\right). \tag{3.3a}$$

In the simple model of section 2.5.3, it was assumed that the voltage across the ROS was either zero or V_g. As Fig. 3.3 shows, this is not valid for a well damped ROS operating at an elevated relaxation frequency. Therefore, the expression for the duration of the voltage state as given by Eq. (2.22b) is not applicable in this case. Recognizing that each voltage pulse in a moderately damped ROS is just half a cycle of the L_{sh}-C_{sq} oscillation, T_V can be approximated with

$$T_V \approx \pi\sqrt{L_{sh}C_{sq}}\,. \tag{3.3b}$$

According to Eqs. (3.3a) and (3.3b), variations in Φ_{sig} or I_b mainly affect T_0, whereas T_V remains about constant.

3.1.3 Operation range

The persistence of the relaxation oscillations depends on a number of parameters. In this section, an operation criterion for ROSs will be derived. The critical stage in the relaxation oscillation scheme is the switching process from the voltage state to the superconducting state. As was shown in the previous section, the voltage pulses generated by a well damped ROS decay exponentially to the asymptotic value $V_\infty \approx I_b \cdot R_{sh}$. Before this voltage is reached, the hysteretic dc SQUID should have switched back to the superconducting state, otherwise the relaxation oscillations stop in the situation where almost all of the bias current flows through the L_{sh}-R_{sh} branch of the ROS, the current through the SQUID being just large enough to prevent a transition to the superconducting state. If $V_\infty < V_{min}$, this stable state does not exist, which leads to the following operation criterion for a ROS:

$$V_\infty = I_b \frac{R_{sh}R_d}{R_{sh}+R_d} \approx I_b R_{sh} < V_{min} = \frac{4}{\pi}\sqrt{\frac{I_c\Phi_0}{2\pi C_{sq}}} \quad \Leftrightarrow$$

$$\beta_C^* \cdot \left(\frac{I_b}{I_c}\right)^2 < \frac{16}{\pi^2} \approx 1 \qquad \text{with} \quad \beta_C^* = \frac{2\pi I_c R_{sh}^2 C_{sq}}{\Phi_0}. \tag{3.4}$$

The β_C^* parameter introduced in Eq. (3.4) is the *effective McCumber parameter* for relaxation oscillation SQUIDs.

For ROSs with a damping parameter $D < 1$, the parasitic L_{sh}-C_{sq} resonances can help to overcome the stable state in the subgap. Hence, underdamped ROSs can also operate outside the margins of Eq. (3.4). Moreover, thermal fluctuations in the junctions can increase the minimum return voltage V_{min}, which also enlarges the maximum bias current at which a ROS can operate. This is in agreement with the experimental results, which showed that the maximum bias current of a ROS decreases at lower temperatures.

The definition of β_C^* is similar to that of β_C in a non-hysteretic dc SQUID, R_{sh} being the equivalent of the shunt resistors across the junctions. Just like a conventional dc SQUID should have $\beta_C < 1$, Eq. (3.4) implies that for a ROS β_C^* should be below unity to ensure proper operation. Hence, the value of the resistor R_{sh} in a ROS has to be of the same order as the junction shunt resistors in a conventional dc SQUID. Therefore, the voltage modulation depth and the flux-to-voltage transfer of a ROS, used with voltage readout, are comparable to those of a resistively shunted dc SQUID.

3.1.4 Output power

For a ROS with frequency readout, only the frequency and not the amplitude of the output pulses is of interest. Nevertheless, the output power should be sufficient for frequency detection. Approximating the output signal of a ROS by a series of delta pulses, the power P which is supplied to an external resistive load Z_{load} at the fundamental frequency f_{RO} can be calculated as [5]

$$P = \frac{2 f_{RO}^2 A^2}{Z_{load}} \qquad \text{with} \quad A = \int_{one\ pulse} V(t)\,dt, \tag{3.5}$$

where A represents the area of one relaxation pulse in the V-t diagram. This area can be estimated by modeling the relaxation pulses as triangles of height $I_c R_d$ and duration $T_V \approx \pi\sqrt{(L_{sh} C_{sq})}$ [Eq. (3.3b)], yielding $A \approx \frac{1}{2}\pi \cdot I_c R_d \cdot \sqrt{(L_{sh} C_{sq})}$. By means of numerical simulations, A can be evaluated more accurately. Taking $Z_{load} = 50\ \Omega$, numerical simulations yield for instance $A \approx 100$ fV·s for the ROS of Fig. 3.3. According to Eq. (3.5), this corresponds to a high frequency output power of $P = 0.32$ nW (= -65 dBm), which is sufficient for detection with room temperature electronics.

The effect of impedance matching [6] can be studied by decreasing the load impedance Z_{load}. If $Z_{load} \approx R_d$, the load affects the ROS dynamics considerably, e.g. by decreasing the amplitude of the voltage pulses. For instance, with $Z_{load} = 10\ \Omega$, numerical simulations yield $A = 55$ fV·s for the same ROS as above, which corresponds to a slight increase of the output power to $P = 0.87$ nW (= -61 dBm). Simulations with other parameters yielded similar power levels. In conclusion, impedance matching can increase the output power of a ROS slightly, but the influence of the load impedance on the ROS dynamics can not be neglected for small values of Z_{load}.

3.2 Noise sources in the ROS

Apart from parasitic L_{sh}-C_{sq} resonances, which, as shown in section 3.1.2, can be suppressed adequately with a damping resistor R_d, also other noise sources exist in the relaxation oscillation SQUID. In this section, the most important noise mechanisms, viz. the thermally induced critical current fluctuations of the dc SQUID and the Johnson noise generated by the resistors R_{sh} and R_d, will be discussed.

The discussion will be restricted to white noise, although, like conventional dc SQUIDs, ROSs also suffer from 1/f noise. However, this 1/f noise is not intrinsic to the relaxation oscillation scheme, but rather caused by material properties, like the junction quality and the composition of the SQUID body [7].

3.2.1 Thermally induced fluctuations of the critical current

Thermally induced fluctuations of the critical current [1,8] lead to variations in the relaxation frequency and thus cause noise. In this section, the single junction approximation will be used to evaluate the effect of these thermal fluctuations [9,10,11,12].

In the washboard model, discussed in section 2.2.3, the depth ΔE of the potential wells in which the ball can be captured is given by:

$$\Delta E = \frac{I_0 \Phi_0}{\pi} \cdot \left(\sqrt{1 - \left(\frac{I}{I_0} \right)^2} - \frac{I}{I_0} \arccos\left(\frac{I}{I_0} \right) \right). \tag{3.6}$$

If the ball is trapped in one of the potential wells, the thermal energy fluctuations of the order of $k_B T$ cause Brownian motion of the ball. This random motion can cause escape out of the local potential minimum at a current well below the critical current. If the current I is much smaller than I_0, the depth of the potential well is $\Delta E \approx I_0 \Phi_0 / \pi$, which is large compared to the thermal fluctuations - provided that the noise rounding parameter $\Gamma \ll 1$ [cf. Eq. (2.9)]. Therefore, the escape probability is small at low bias currents. On the other hand, if I is only slightly below I_0, $\Delta E \approx 0$, and thermal fluctuations can easily cause escape across the barrier.

The *attempt frequency* for escape out of the potential well is approximately given by the plasma frequency f_p [Eq. (2.6)]. Actually, for damped Josephson junctions, the attempt frequency differs slightly from f_p, but this deviation is not large [13]. The average lifetime τ of the superconducting state is given by [8]

$$\tau^{-1} = f_p \exp\left(-\Delta E / k_B T \right). \tag{3.7}$$

When the current through the junction is swept from zero towards the critical current, the probability W that a thermally activated transition to the voltage state has not occurred between time $t = 0$ and $t = \mathrm{T}$ is given by:

$$W = \exp\left(-\int_0^{\mathrm{T}} \frac{dt}{\tau(t)}\right). \tag{3.8}$$

Because I is changed in time, τ in Eq. (3.8) is also a function of time via Eqs. (3.6) and (3.7). Equation (3.8) can be evaluated numerically, a typical result of such a numerical calculation is shown in Fig. 3.4 [9].

The probability that the junction switches to the voltage state in a current interval between I and $I+\Delta I$ is given by $W(I) - W(I+\Delta I) \approx -[\partial W(I)/\partial I]\cdot\Delta I = P(I)\cdot\Delta I$. The distribution function of the critical current $P(I) = -\partial W(I)/\partial I$ is also plotted in Fig. 3.4.

The spread on the critical current, ΔI_0, is defined in Fig. 3.4 as the full width at half-maximum of the probability distribution P. This spread ΔI_0 depends on the sweep rate of the current through the junction (i.e. on the relaxation frequency of the ROS), on the temperature, on the critical current and on the junction capacitance. For a junction capacitance around 1 pF, a critical current of the order of 10 μA and a relaxation frequency of about 1 GHz, the thermal spread on the critical current can be approximated with [9,14,15]

$$\Delta I_0 = \alpha \cdot I_0^{1/3} \quad , \quad \alpha \approx 2.5 \cdot 10^{-5}\ \mathrm{A}^{2/3} \ @\ 4.2\ \mathrm{K}\,. \tag{3.9}$$

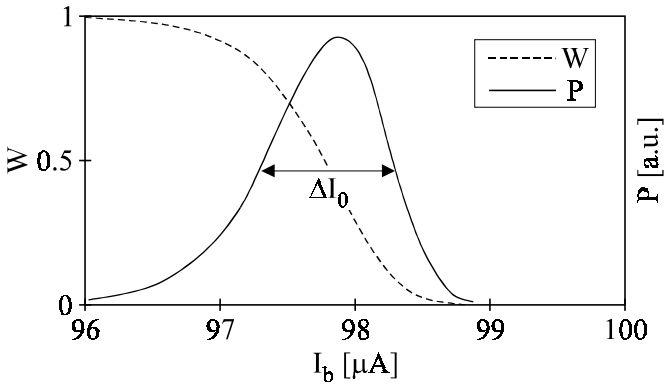

Figure 3.4 *Theoretical distribution P of the critical current of a Josephson tunnel junction with a critical current of $I_0 = 100\ \mu A$ and a capacitance of $C_j = 1$ pF. The sweep rate $\partial I/\partial t$ of the current through the junction is about $5\cdot10^7\ I_0/s$ and the temperature is 4.2 K. The dashed line indicates the probability W that the junction has not switched to the voltage state at a certain bias current. Data from ref. [9].*

According to ref. [16], α scales with temperature as $T^{2/3}$. Equation (3.9) is a fit to numerically calculated data, and is reasonably accurate for a wide range of junction parameters. For extreme parameter values, however, Eq. (3.9) does not hold. For example, according to Fig. 6.8 in ref. [9], ΔI_0 is below the value given by Eq. (3.9) for Josephson junctions with a small capacitance and a small critical current.

In a ROS, the critical current $I_c(\Phi_{sig})$ is sampled f_{RO} times per second. If the standard deviation per sample is $\sigma(I_c)$, the resulting flux noise spectral density at frequencies much lower than f_{RO} is given by

$$S_\Phi = \frac{1}{f_{RO}} \cdot \frac{\sigma^2(I_c)}{\left(\partial I_c/\partial \Phi_{sig}\right)^2} . \tag{3.10a}$$

Approximating $\sigma(I_c)$ with $\Delta I_c/3$ [9,15], and evaluating ΔI_c with the single junction expression of Eq. (3.9), Eq. (3.10a) can be rewritten to

$$S_\Phi \approx \chi_{ros} \cdot \frac{\left(1+\beta_L\right)^2 \cdot \Phi_0^2}{f_{RO} \cdot I_0^{4/3}} \quad ,$$

$$\chi_{ros} \approx \frac{\alpha^2}{110} = 5.7 \cdot 10^{-12}\ \mathrm{A}^{4/3}\ @\ 4.2\ \mathrm{K} , \tag{3.10b}$$

where $\partial I_c/\partial \Phi_{sig}$ was calculated with [9]

$$\left| \frac{\partial I_c}{\partial \Phi_{sig}} \right|_{\Phi_{sig}=\frac{1}{4}\Phi_0} \approx \frac{4.4}{1+\beta_L} \cdot \frac{I_0}{\Phi_0} . \tag{3.11}$$

In Eqs. (3.10b) and (3.11), I_0 represents the critical current of one junction. The temperature dependence of χ_{ros} follows as $\chi_{ros} \propto \alpha^2 \propto T^{4/3}$ [11,16].

As Eq. (3.10b) shows, the sensitivity of a ROS improves with increasing relaxation frequency. However, apart from practical problems, f_{RO} can not be increased infinitely to enhance the sensitivity. At high relaxation frequencies, the relaxation oscillations and the plasma oscillations of the junctions start to interfere, which causes unpredictable transitions between the voltage state and the superconducting state [6,17,18,19,20]. This effect is illustrated by the numerical simulations in Fig. 3.5. Figure 3.5a displays the same numerical simulation as Fig. 3.3a, whereas Fig. 3.5b shows a numerical simulation with the same ROS parameters, only L_{sh} was changed from 2 nH to 50 pH in order to increase the relaxation frequency. The plasma frequency of the junctions is ~83 GHz. Obviously, the random behaviour shown in Fig. 3.5b is disastrous for the sensitivity of the ROS.

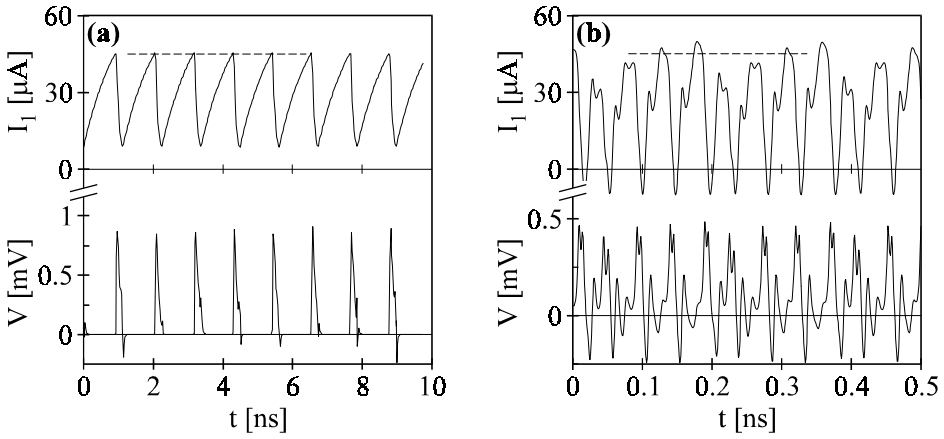

Figure 3.5 *Numerical simulations of a ROS with the same parameters as the ROS in Fig. 3.3.* **(a)** L_{sh} *= 2 nH,* f_{RO} *= 0.9 GHz.* **(b)** L_{sh} *= 50 pH,* $f_{RO} \approx$ *25 GHz. The horizontal dashed lines indicate the critical current, which is 45 μA.*

The ROS of Fig. 3.5b has a relaxation frequency of f_{RO} = 20 .. 25 GHz. At this very high relaxation frequency, the effect of the interaction between the plasma oscillations and the relaxation oscillations is evident. Numerical simulations indicate that the interference between the plasma oscillations in the junctions and the relaxation oscillations already starts to limit the sensitivity when f_{RO} exceeds ~1% of the plasma frequency [18]. For most practical devices $f_p \approx 100$ GHz, which implies an optimum relaxation frequency of $f_{RO} \approx 1$ GHz [11,12,15].

According to Eq. (3.10b), the thermally induced critical current spread causes a white flux noise of $\sqrt{S_\Phi} \approx 0.2\ \mu\Phi_0/\sqrt{\text{Hz}}$ in a 1 GHz ROS with a SQUID inductance of L_{sq} = 35 pH and a junction critical current of I_0 = 30 μA (β_L = 1). This is comparable to the flux noise of a conventional dc SQUID with resistively shunted tunnel junctions.

The preceding discussion only holds in the *thermal limit*, where thermal fluctuations are the dominating mechanism for escape out of the potential wells. In the *quantum limit*, macroscopic quantum tunneling through the barrier dominates the escape rate. In ref. [21], a cross-over temperature between the thermal and the quantum regime of $T_{cr} = hf_p/(20k_B)$ is reported. The devices in this thesis are based on Josephson junctions with a plasma frequency not exceeding a few hundred GHz, implying a cross-over temperature of $T_{cr} \approx 0.5$ K. As all measurements were performed in the temperature range 1.6 K < T < 4.2 K, the thermal noise largely dominated the quantum effects.

3.2.2 Johnson noise

Besides the thermal fluctuations on the critical current, also the Johnson noise generated in the resistors R_{sh} and R_d affects the ultimate sensitivity of a ROS. The Johnson noise causes a noise current $I_{n,Rsh}$ respectively $I_{n,Rd}$ through the dc SQUID, which can cause premature switching from the superconducting to the voltage state. In order to estimate the significance of the Johnson noise, the magnitude of the additional critical current spread due to $I_{n,Rsh}$ and $I_{n,Rd}$ should be compared with the thermally induced spread ΔI_c, which, according to Eq. (3.9), amounts to ~1 μA for a ROS with a typical critical current of $I_c = 2I_0 = 60$ μA.

The Johnson noise generated by R_{sh} is low pass filtered by the L-R circuit constituted by L_{sh} and R_{sh}. Hence, the effective bandwidth of $I_{n,Rsh}$ is of the order of the relaxation frequency, leading to a root mean square (rms) value of

$$I_{n,Rsh}(\text{rms}) \approx \sqrt{\frac{4k_B T}{R_{sh}}} \cdot \sqrt{f_{RO}} \,. \tag{3.12}$$

Substituting a typical value of $R_{sh} = 2\ \Omega$, Eq. (3.12) yields $I_{n,Rsh}$ (rms) ≈ 0.3 μA for a 1 GHz ROS operating at $T = 4.2$ K. This is well below the above-mentioned spread of about 1 μA due to thermal fluctuations. This example shows that in most practical cases the Johnson noise generated by R_{sh} only has a minor contribution to the overall noise.

As the Johnson noise generated by the damping resistor R_d is not filtered by an L-R circuit, its effective bandwidth is approximately the plasma frequency of the Josephson junctions, which implies an rms value of

$$I_{n,Rd}(\text{rms}) \approx \sqrt{\frac{4k_B T}{R_d}} \cdot \sqrt{f_p} \tag{3.13}$$

for the Johnson noise originating from R_d. With typical values for f_p and R_d (100 GHz respectively 25 Ω), Eq. (3.19) yields $I_{n,Rd}$ (rms) ≈ 1 μA, which is equal to the thermally induced critical current spread. This example indicates that thermal noise from the damping resistor R_d can be a serious source of excess noise.

Therefore, the design value for R_d should be a trade-off between acceptable Johnson noise - requiring a high resistance - and sufficient damping of parasitic L_{sh}-C_{sq} resonances - requiring a low resistance.

3.3 Experimental ROS characteristics

3.3.1 ROS layout

In order to investigate the behaviour of ROSs operating at relaxation frequencies in the GHz range, ROSs with L_{sh}/R_{sh} = 1 ns (1 GHz ROSs) and L_{sh}/R_{sh} = 0.1 ns (10 GHz ROSs) were designed and fabricated by Adelerhof *et al.* at the Superconducting Sensor Laboratory [22] in Japan. The design parameters of these ROSs are listed in Table 3.1.

Figure 3.6 shows micrographs and schemes of the 1 GHz and the 10 GHz ROS designs. The 2 x 2 μm² Nb/Al,AlO_x/Nb tunnel junctions, the other Nb structures and the SiO_2 insulating layer were patterned with reactive ion etching in CF_4. The resistors were structured in an Al thin film by wet chemical etching in a NaOH solution. The junction critical current amounts to $I_0 \approx 30$ μA and the junction capacitance is estimated to be ~0.25 pF per junction.

The inductance of the square Nb shunt inductor in the 1 GHz ROSs was calculated with [23]

$$L_{sh} = \frac{2}{\pi}\mu_0 a \ln\left(\frac{2a}{b}\right) \qquad (a \gg b), \tag{3.14}$$

with a and b as indicated in Fig. 3.6. For the 1 GHz ROSs, three different values of L_{sh} were designed: 0.9 nH (a = 280 μm, b = 10 μm), 1.7 nH (a = 470 μm, b = 10 μm) and 3.0 nH (a = 750 μm, b = 10 μm).

The shunt inductance of the 10 GHz ROSs was designed symmetrically around the dc SQUID in order to avoid distortion of the ROS characteristics due to magnetic coupling between L_{sh} and the SQUID [24,25]. In this configuration, L_{sh} was calculated as half the inductance of one of the two parallel loops. The design values for L_{sh} in the 10 GHz ROSs were 0.16 nH (a = 150 μm, b = 20 μm) and 0.30 nH (a = 260 μm, b = 30 μm).

In order to keep the layout as symmetric as possible, the damping resistance was distributed over two parallel meander-shaped resistors with a resistance of $2R_d$ each. For the 1 GHz ROSs, three different values for the damping

	L_{sh}= 3 nH			L_{sh}= 1.7 nH			L_{sh}= 0.9 nH			L_{sh}= 0.3 nH			L_{sh}= 0.16 nH		
D	R_{sh}	R_d	β_C^*	R_{sh}	R_d	β_C^*	R_{sh}	R_d	β_C^*	R_{sh}	R_d	β_C^*	R_{sh}	R_d	β_C^*
0.1	3	123	0.82	1.7	92	0.26	0.9	70	0.07	3	39	0.82	1.7	29	0.26
1	3	39	0.82	1.7	29	0.26	0.9	22	0.07	3	12.3	0.82	1.7	9.2	0.26
10	3	12.3	0.82	1.7	9.2	0.26	0.9	7	0.07	...	...	...	...	...	...

Table 3.1 *Design parameters of the investigated ROSs. The columns with L_{sh} = 0.3 nH and L_{sh} = 0.16 nH represent the 10 GHz ROSs, in the other columns, the parameters of the 1 GHz ROSs are listed. (R_{sh} and R_d in Ω).*

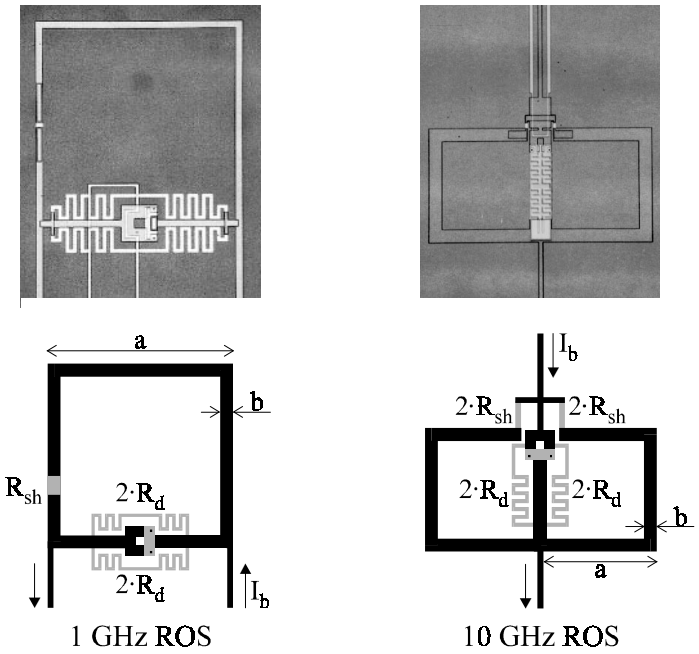

Figure 3.6 *Micrographs and schemes of the ROSs which were used in the experiments. In the 10 GHz ROS design, the meander-shaped damping resistors are covered by a Nb film, electrically insulated from the resistors with a SiO_2 layer.*

parameter were designed: $D = 10$, 1 and 0.1. In the case of the 10 GHz ROS, only $D = 1$ and 0.1 were implemented. For $D = 10$, R_d should be ~ 3 Ω, causing non-hysteretic junction behaviour because $\beta_C < 1$.

The washer-type hysteretic dc SQUIDs have a hole dimension of 13 µm and an outer width of 50 µm. The signal flux is applied by means of an integrated half-turn input coil. From the experimental critical current modulation depth, the SQUID inductance L_{sq} was determined to be 30 .. 35 pH ($\beta_L \approx 1$). This is more than the expected value of 20 pH [from Eq. (2.19)], which is probably due to the small outer dimensions of the SQUID washers.

3.3.2 Characterization setup

A schematic diagram of the setup that was used for the characterization of the ROSs is displayed in Fig. 3.7. The devices were cooled down in a stainless steel ^{4}He bath cryostat. To prevent disturbances due to external electromagnetic noise, the ROSs were enclosed by a superconducting niobium shield with a length of 19 cm and a diameter of 6 cm. For additional shielding, the entire cryostat was surrounded by a cylindrical µ-metal shield.

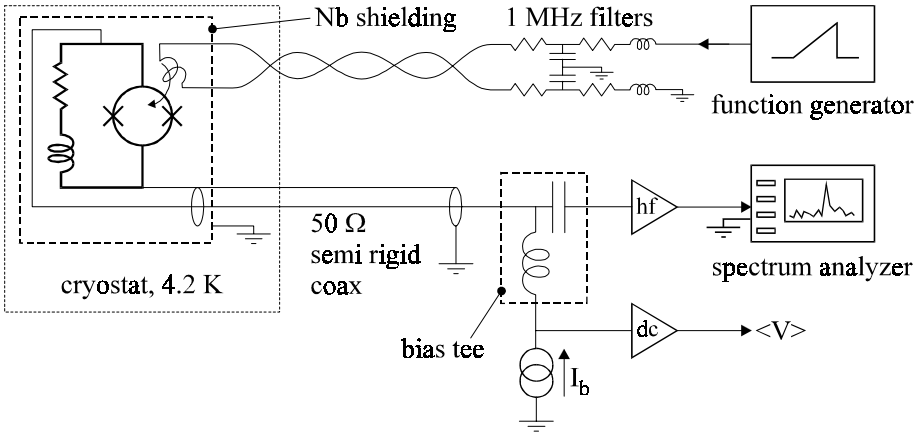

Figure 3.7 *The ROS characterization setup.*

Four ROSs were glued on an epoxy printed circuit board (PCB) and cooled down simultaneously. The electric contacts between the ROSs and the copper transmission lines on the PCB were made by ultrasonic bonding of 25 μm thick Al wires with a length of approximately 5 mm. According to ref. [23], the parasitic inductance of these bonding wires is 10 to 20 nH. By means of subminiature A (SMA) connectors, the transmission lines on the PCB were connected to 50 Ω semi-rigid coaxial cables. Optionally, 50 Ω surface mounted device (SMD) resistors could be connected in series with the ROSs in order to study the effect of transmission line reflections.

The coaxial cables were used both to supply the dc bias current I_b to the ROSs and to transfer the high frequency output signal from the ROSs to the room temperature electronics. For this purpose, a *bias tee* (Mini-Circuits ZFBT-6G [26]) was used to split the ac and dc signals. After pre-amplification with a Hewlett Packard 83006A microwave system amplifier (gain ~25 dB), the high frequency ROS output was coupled to a HP 8563E spectrum analyzer. For ground isolation, the home made bias current source was battery powered, and the ground potential for the whole setup was determined by the spectrum analyzer.

The time-averaged voltage $\langle V \rangle$ across the ROS was measured with a low noise differential dc amplifier. As this is a two-point measurement, the raw readout voltage had to be corrected for the resistance of the bias tee, the coaxial cable and the bonding wires, summing up to about 3.5 Ω.

The input coils of the ROSs were connected to a function generator by means of twisted manganin wires, shielded by a stainless steel tube. These wires were low pass filtered at the top of the cryostat in order to prevent degradation of the ROS characteristics due radio frequency interference (RFI) [27].

3.3.3 Voltage readout

In Fig. 3.8a, the experimental *I*-*V* characteristic of a 1 GHz ROS is shown. During the recording of this graph, the signal flux was swept with an amplitude of several Φ_0 at a frequency considerably higher then the sweep rate of the bias current. Figure 3.8b shows the V-Φ_{sig} characteristics of the same ROS for 11 different bias currents. Both plots have been corrected for offset voltages due to the two-point measurement via the semi-rigid coaxial cable.

Figure 3.8a shows modulation for bias currents up to about 225 μA. For larger bias currents, the ROS does not oscillate anymore, as has been discussed in section 3.1.3. In this case, the voltage across the ROS is given by $V = V_\infty \approx I_b \cdot R_{sh}$, which gives a direct method to determine the value of R_{sh}, as illustrated by the dashed line in Fig. 3.8a. Using Eq. (2.14), the SQUID inductance of the devices was determined from the critical current modulation $I_{c,max} - I_{c,min}$, as presented in the inset of Fig. 3.8a.

For large bias currents, the V-Φ_{sig} characteristics became irregular. For all ROSs with $D = 1$, except those having $R_{sh} \approx 1\ \Omega$, the bias current at which the first irregularities appeared was slightly larger than the theoretical maximum bias current as calculated with Eq. (3.4). Only for the ROSs with $R_{sh} \approx 1\ \Omega$, the experimental maximum bias current (~150 μA) was smaller than the calculated value of 225 μA. The maximum operation current was also dependent on the value of the damping parameter D. In general, the ROSs with $D = 0.1$ had a somewhat larger maximum bias current than their counterparts with $D = 1$. This is because the parasitic L_{sh}-C_{sq} resonances can help to overcome the stable

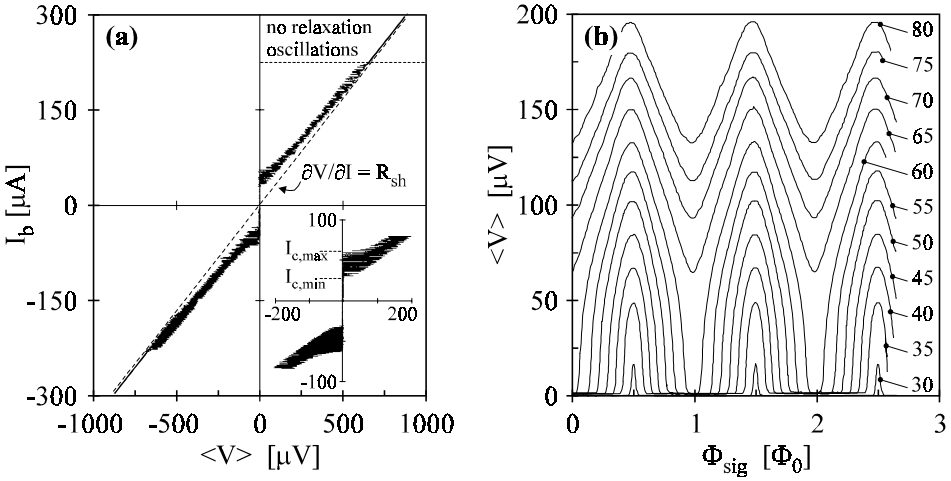

Figure 3.8 **(a)** *I_b-<V> characteristic of a 1 GHz ROS with design parameters L_{sh} = 3 nH, R_{sh} = 3 Ω and D = 0.1. The inset shows a detailed view of the curve near the origin.* **(b)** *<V>-Φ_{sig} characteristics of the same ROS for 11 different bias currents, indicated at the right in μA.*

state in the subgap of the SQUID. Accordingly, the devices with $D = 10$ had a slightly smaller maximum bias current than those with $D = 1$.

The flux-to-voltage transfer of the V-Φ_{sig} traces in Fig. 3.8b is about 200 $\mu V/\Phi_0$ for bias currents slightly above $I_{c,max}$. According to Eq. (2.16), a comparable non-hysteretic dc SQUID with junction shunt resistors of 3 Ω ($\beta_C = 0.2$), has the same flux-to-voltage transfer. This is an experimental confirmation of the statement that ROSs are not particularly suited for voltage readout. In literature, ROSs with much higher values for $\partial V/\partial\Phi_{sig}$ have been reported [15]. However, these high transfers originated mainly from parasitic magnetic coupling between L_{sh} and the SQUID, causing an APF-like deformation of the V-Φ_{sig} characteristics. From the horizontal shift of the V-Φ_{sig} characteristics at different bias currents, the parasitic coupling between L_{sh} and L_{sq} was determined to be only 1 .. 2 pH for the present 1 GHz ROSs. Due to their symmetric layout, the 10 GHz ROSs showed an even smaller magnetic coupling between L_{sh} and the SQUID.

3.3.4 Frequency readout

In Fig. 3.9, the power spectral density S of the fundamental harmonic of a current biased 1 GHz ROS is shown for four different values of Φ_{sig}. The scale of the vertical axis has not been corrected for the gain of the pre-amplifier (~25 dB). The measured power level of the ground harmonic was typically 10 to 20 dB below the theoretical value calculated with Eq. (3.5). Probably, this is caused by transmission line losses; especially the connection between the ROSs

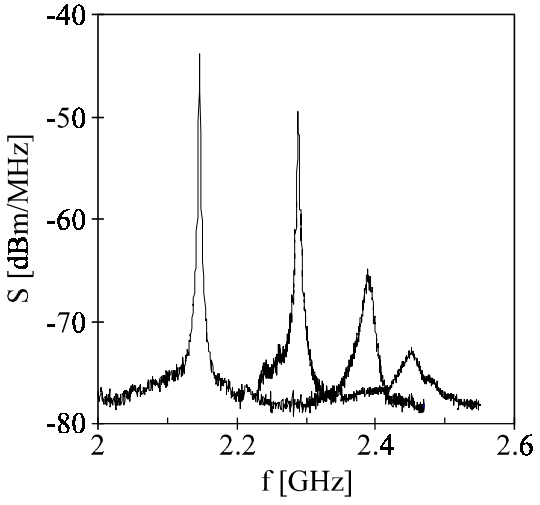

Figure 3.9 *Spectra of the output voltage of the ROS of Fig. 3.8, measured at a fixed bias current for four different values of Φ_{sig}. The vertical scale has not been corrected for the gain of the pre-amplifier, which is about 25 dB.*

and the coaxial cables is not ideally suited for high frequencies due to the parasitic inductance of the bonding wires.

Due to the spectral impurity of the relaxation oscillation frequency, the output power is spread over a considerable bandwidth, often hundreds of MHz. In Fig. 3.9, this effect causes the peak width to increase and the peak height to decrease at higher relaxation frequencies. This behaviour is typical [25], and in practice it often caused the output signal of the ROS to drown in the system noise at high relaxation oscillation frequencies. The experimental output power was smaller for ROSs with larger damping parameters D (i.e. small R_d), which is to be expected as the damping resistor R_d decreases the amplitude of the voltage pulses at the output. Similarly, the output power also decreased for ROSs with a smaller shunt resistor R_{sh}. In the 1 GHz ROS with $R_{sh} = 0.9\ \Omega$ and $D = 10$, both effects add, and consequently, the output power was too small for detection with the present setup. The output of all 10 GHz ROSs was difficult to measure due to the high relaxation frequencies and the associated large transmission line losses.

The shape of the peaks did not change qualitatively when a 50 Ω metal film SMD resistor was connected between the ROSs and the coaxial cable, apart from a small reduction of the peak height. This indicates that the ROS dynamics is not severely influenced by the readout system. No clear relation could be found between the spectral width of the peaks and the ROS parameters. Moreover, resonances, occurring either in the ROS or in the readout system, caused the peak width to vary with the relaxation frequency. As a result, the output spectrum showed narrow peaks for certain combinations of I_b and Φ_{sig}. However, at these points, the flux-to-frequency transfer $\partial f_{RO}/\partial\Phi_{sig}$ was also rather low. Therefore, an estimation of the flux noise based on the spectral impurity of the relaxation oscillation signal, as given in ref. [28], is doubtful.

Figure 3.10 shows the experimental f_{RO}-Φ_{sig} characteristics of two different 1 GHz ROSs. The characteristics were automatically recorded by a personal computer which was interfaced to the spectrum analyzer for frequency detection and to an analogue-to-digital converter for measuring the signal flux. The β_C^* parameter of the ROS in Fig. 3.10b is smaller than that of the ROS in Fig. 3.10a (design values 0.07 respectively 0.82). Therefore, the ROS in Fig. 3.10b can operate at larger bias currents [see Eq. (3.4)], and thus at higher relaxation frequencies, than the ROS in Fig. 3.10a.

The solid lines in Fig. 3.10 are theoretical fits to the f_{RO}-Φ_{sig} measurements. In these fits, f_{RO} was calculated as $1/(T_0+T_V)$, with T_0 from Eq. (3.3a) and with T_V a constant fit parameter. The value of L_{sh} was also a fit parameter. All other parameters were fixed: L_{sq} was determined from the critical current modulation, R_{sh} was derived from the I-V characteristic, and for R_d and C_{sq} the design values were taken. The flux dependence of the critical current of the dc SQUID was calculated numerically [29], taking into account the magnetic coupling between L_{sh} and L_{sq}, which was determined from the V-Φ_{sig} characteristics.

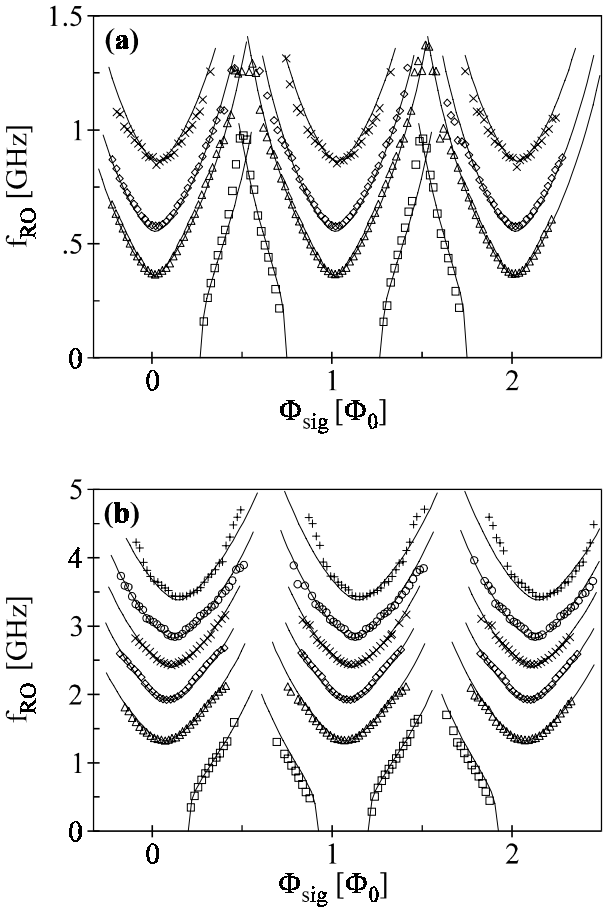

Figure 3.10 *Experimental f_{RO}-Φ_{sig} characteristics (markers) with theoretical fits (solid lines) of two 1 GHz ROSs. All fit values are listed in Table 3.2.*
(a) *ROS with a designed shunt inductance of L_{sh} = 3 nH, the value used for the theoretical fits is 3.25 nH. The ROS was biased at four different bias currents: I_b = 45 μA (□), I_b = 65 μA (△), I_b = 75 μA (◇) and I_b = 95 μA (×).*
(b) *ROS with a designed shunt inductance of L_{sh} = 0.9 nH, the value used for the theoretical fits is 0.95 nH. The ROS was biased at six different bias currents: I_b = 55 μA (□), I_b = 80 μA (△), I_b = 100 μA (◇), I_b = 120 μA (×), I_b = 140 μA (○) and I_b = 170 μA (+).*

Fits as shown in Fig. 3.10 have been made for all the characterized ROSs. For the 1 GHz ROSs, all configurations with the same design value for L_{sh} were confined to one common fit value for L_{sh}, whereas for the 10 GHz ROSs small differences were permitted. The reason for allowing these small (< 3%) differences for the 10 GHz ROSs is that, due to the smaller dimensions of the

D	L_{sh} [nH]		R_{sh} [Ω]	T_V [ps]	$I_{c,max}$ [μA]	$f_{RO,max}$ [GHz]
Design	Design	Fit	Meas.	Fit	Meas.	Meas.
0.1 [d]	3	3.25	3.0	133	61	2.6
1 [b]	3	3.25	2.8	120	59	1.4
10	3	3.25	2.5	113	53	1.4
0.1	1.7	1.70	2.0	169	69	2.6
1	1.7	1.70	1.6	141	57	1.8
10	1.7	1.70	2.0	173	56	1.7
0.1 [c]	0.9	0.95	2.0	96	61	5.0
1	0.9	0.95	1.6	125	70	2.1
10	0.9	[a]	1.5	[a]	62	[a]
0.1	0.3	0.35	2.0	50	66	6.8
1	0.3	0.34	1.6	39	72	5.6
0.1	0.16	0.19	1.0	26	71	5.6
1	0.16	0.19	1.1	35	71	5.8

[a] Output signal too weak for f_{RO}-Φ_{sig} measurements.
[b] f_{RO}-Φ_{sig} fit is shown in Fig. 3.10a.
[c] f_{RO}-Φ_{sig} fit is shown in Fig. 3.10b.
[d] characteristics are shown in Figs. 3.8, 3.9 and 3.12.

Table 3.2 *Measured and designed ROS parameters. For each ROS, the maximum observed relaxation frequency is indicated in the last column.*

shunt inductor, the value of L_{sh} is rather sensitive to small variations in the fabrication process. The resulting fit values of T_V and L_{sh} are listed in Table 3.2. If T_V and L_{sh} were changed by 10%, the f_{RO}-Φ_{sig} fits clearly worsened. This suggests that the fit accuracy is better than 10%. The good correspondence between the fit and design values of L_{sh} is obvious. The fit values for T_V are also plausible as they are of the order of $\pi\sqrt{(L_{sh}C_{sq})}$, as was to be expected from Eq. (3.3b). The maximum observed relaxation frequency $f_{RO,max}$ and the maximum critical current $I_{c,max}$ are also tabulated for each ROS in Table 3.2.

3.3.5 Flux locked loop operation

For flux locked loop (FLL) operation, the output signal of the ROS has to be FM demodulated. For relaxation frequencies below a few hundred MHz, this frequency-to-voltage conversion can be implemented with standard radio electronics [30,31]. For relaxation frequencies in the GHz range, however, the FM demodulation is not straightforward, especially when the center frequency of the demodulator should be adjustable over a range of several GHz.

In order to construct a simple frequency-to-voltage converter, we band pass filtered the ROS output signal around an adjustable center frequency f_c. The amount of rf power after the band pass filter was converted to a voltage V_{bp}. Both the band pass filtering and the power measurement were performed with the HP 8563E spectrum analyzer. As the voltage V_{bp} increases when f_{RO} approaches f_c, it depends on the relaxation frequency of the ROS. Obviously, this is not a strict FM demodulation because not only *frequency* variations, but also *amplitude* variations at the demodulator input induce changes in V_{bp}. An *amplitude limiter* in front of the band pass filter could improve the AM rejection considerably, but this option has not been implemented in the present experiments.

Figure 3.11 gives a schematic overview of the used FLL configuration. The FM demodulated ROS output V_{bp} is fed to an integrator with an adjustable input offset. The output of the integrator supplies the feedback flux to the ROS. The variable feedback resistor R_{fb} was adjusted to give a flux locked loop transfer of $\partial V_{FLL}/\partial\Phi_{sig} = 1\ \mathrm{V}/\Phi_0$. Hence, the output range of the integrator of ±10 V corresponds to a feedback range of $\pm 10\ \Phi_0$. The time constant of the integrator could be varied between 10^{-9} and 10^{-4} s. A test signal V_{test} was added to the feedback signal in order to test the flux locking (switch S closed), or to measure the open loop characteristics of the system (switch S opened).

Figure 3.12 shows the open loop characteristics of a 1 GHz ROS. The two lower traces represent the time-averaged output voltage (corrected for the offset voltage due to the resistance in the readout circuit) and the relaxation frequency as a function of the applied flux. The two upper traces show the output of the FM demodulator, V_{bp}, for $f_c = 1300$ MHz respectively $f_c = 650$ MHz. The trace with $f_c = 650$ MHz shows that the setup works properly since V_{bp} shows maxima when $f_{RO} = f_c = 650$ MHz. The demodulator output with $f_c = 1300$ MHz shows peaks if $f_{RO} = 1300$ MHz, but also if $f_{RO} = 650$ MHz. The latter peaks are caused by the second harmonic in the ROS output if

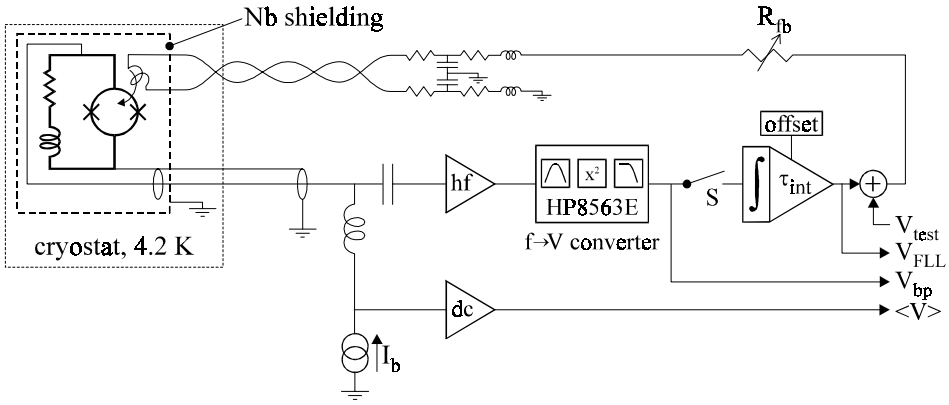

Figure 3.11 *The ROS flux locked loop setup.*

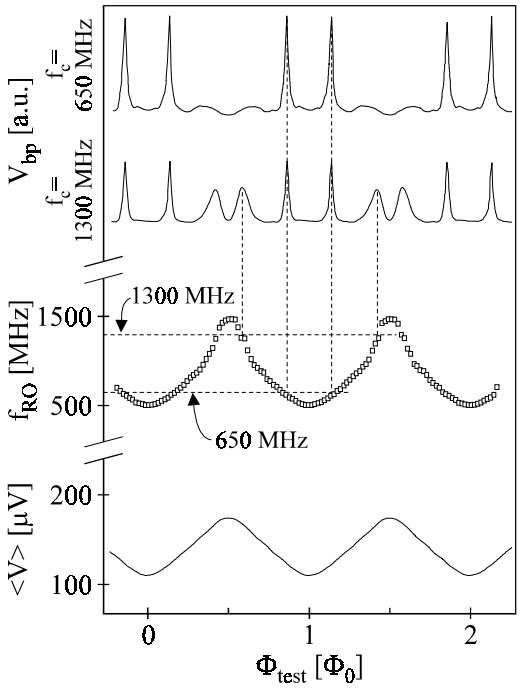

Figure 3.12 *<V>, f_{RO}, $V_{bp}(f_c$=650MHz) and $V_{bp}(f_c$=1300MHz) as function of the applied signal flux Φ_{sig} in open loop configuration for the ROS marked with [d] in Table 3.2. The bias current of the ROS was 75 μA.*

f_{RO} = 650 MHz. Since this peak is more pronounced than the peak caused by the oscillation at f_{RO} = 1300 MHz, flux locking at f_{RO} = 1300 MHz is not stable as the system easily unlocks and relocks to the second harmonic of the f_{RO} = 650 MHz oscillation. Generally, for a given bias current, optimum FLL performance was obtained for f_c slightly larger than the minimum relaxation frequency at that bias current.

All ROSs were operated in the FLL setup of Fig. 3.11. Stable flux locking at relaxation frequencies in the GHz range was achieved for all of them. The bandwidth of the FLL was more than 100 kHz. The flux noise was determined by probing the FLL output with a HP 3562A FFT spectrum analyzer. The 1 GHz ROS with L_{sh} = 3 nH, R_{sh} = 3 Ω and D = 0.1, i.e. the ROS with the largest high frequency output power, had the best white flux noise, $\sqrt{S_\Phi} \approx 2.5\ \mu\Phi_0/\sqrt{\text{Hz}}$ at a locking frequency of f_c = 2.15 GHz. This flux noise corresponds to an energy sensitivity of $\varepsilon = S_\Phi/2L_{sq} \approx 600\ h$. Generally, ROSs with a smaller output power showed higher flux noise levels. Therefore, the 10 GHz ROSs, which theoretically have a better sensitivity, but also a weaker output signal, had a higher flux noise than the 1 GHz ROSs. The best measured white flux noise for

a 10 GHz ROS operated in FLL was $\sqrt{S_\Phi} \approx 4\ \mu\Phi_0/\sqrt{\text{Hz}}$ ($\varepsilon \approx 1500\ h$) at $f_c = 5$ GHz. In all cases, the 1/f corner frequency was below 10 Hz.

3.4 Discussion and conclusions

The operation of a ROS as a flux-to-frequency converter is described very well by the model presented in section 3.1, which is demonstrated by the f_{RO}-Φ_{sig} fits in Fig. 3.10. The model was verified for relaxation frequencies up to 7 GHz, higher relaxation frequencies could not be detected due to transmission line losses. For all characterized devices, the fit values for L_{sh} were very close to the design values.

The voltage readout measurements in section 3.3.3 show that, as expected, the typical flux-to-voltage transfer coefficient of a ROS equals that of a resistively shunted non-hysteretic dc SQUID. Therefore, voltage readout of a ROS has no significant advantages in comparison with the conventional dc SQUID readout scheme. This is confirmed by measurements reported in the literature. In ref. [15], for instance, 100 MHz ROSs were operated in a non-modulated FLL with direct voltage readout. The best observed energy resolution was $\varepsilon \approx 1500\ h$. Reference [32] reports a resolution of around 600 h for a 1 GHz ROS, operated with voltage readout in a flux modulated FLL. These noise levels are significantly above those of non-hysteretic dc SQUIDs.

In section 3.3.5, a FLL based on frequency readout in the GHz range was presented. The best obtained energy sensitivity of $\varepsilon \approx 600\ h$ is better than the sensitivity of 2500 .. 3000 h which has previously been reported in the literature for a flux locked 10 MHz ROS [30]. However, it exceeds the theoretical sensitivity given by Eq. (3.10b) by more than two orders of magnitude. There are two indications that the surplus noise originates mainly from the non-ideal FM demodulator that was used. First, *D*ROSs with an analogous layout showed intrinsic energy resolutions as low as 13 h [33,34], which is close to the theoretical expectation (see chapter 4). Second, a correlation was observed between the output power of the ROSs and the noise performance. This suggests that spurious AM components in the output signal of the ROS cause significant fluctuations at the output of the frequency-to-voltage converter.

A cryogenic high electron mobility transistor (HEMT) high frequency pre-amplifier, as used for the readout of contemporary rf SQUIDs [35], could improve the sensitivity significantly. Another advantage of this configuration would be the decoupling of the ROS and the coaxial transmission line, which prevents degradation of the ROS characteristics due to transmission line resonances. However, such a cryogenic pre-amplifier would increase the complexity of the system. Moreover, the number of wires from room temperature to the cryogenic environment would be increased, as is the power dissipation at 4.2 K. This is in contradiction with the primary aim of the work in this thesis, which is to reduce the complexity of dc SQUID systems.

The need for high frequency transmission lines between the ROS and the electronics at room temperature is another drawback in comparison with other second generation dc SQUID systems, e.g. the dc SQUID array, the dc SQUID with APF or the DROS. These schemes can be operated with simple twisted wires for readout. In a multi-channel ROS system, the number of coaxial cables could be reduced by connecting several ROSs in series, each ROS being flux locked at a different relaxation frequency. However, in this configuration, the maximum number of ROSs per transmission line is still limited because the output signals of the different ROSs should not overlap in the frequency domain. Moreover, if one ROS unlocks, its output frequency is not determined anymore, and therefore it can also cause the other ROSs to unlock.

References

[1] M. Klein and A. Mukherjee, "Thermal noise induced switching of Josephson logic devices", *Appl. Phys. Lett.* **40**, 744-747 (1982).

[2] Simulation software: JSIM 2.1, developed by E.S. Fang, University of California, Berkeley, CA 94720, U.S.A.

[3] T.A. Fulton, "Punchthrough and the tunneling cryotron", *Appl. Phys. Lett.* **19**, 311-313 (1971).

[4] T.A. Fulton and R.C. Dynes, "Switching to zero voltage in Josephson tunnel junctions", *Solid State Comm.* **9**, 1069-1073 (1971).

[5] M.J. van Duuren, D.J. Adelerhof, G.C.S. Brons, J. Kawai, G. Uehara, H. Kado, J. Flokstra and H. Rogalla, "Frequency readout of relaxation oscillation superconducting quantum interference devices in the GHz regime", *J. Appl. Phys.* **80**, 4164-4173 (1996).

[6] A.D. Smith, R.D. Sandell, A.H. Silver and J.F. Burch, "Chaos and bifurcation in Josephson voltage-controlled oscillators", *IEEE Trans. Magn.* **23**, 1267-1270 (1987).

[7] J. Clarke, "SQUID fundamentals", in *SQUID Sensors: Fundamentals, Fabrication and Applications*, ed. H. Weinstock, NATO ASI Series **329**, Kluwer Academic Publishers, Dordrecht / Boston / London (1996).

[8] T.A. Fulton and L.N. Dunkleberger, "Lifetime of the zero-voltage state in Josephson tunnel junctions", *Phys. Rev. B* **9**, 4760-4768 (1974).

[9] D.J. Adelerhof, *Second generation dc SQUID magnetometers: (Double) Relaxation Oscillation SQUIDs*, Ph.D. thesis University of Twente, Enschede (1993).

[10] J. Kadlec, "Noise margins for Josephson logic and memory devices", *IEEE Trans. Magn.* **19**, 1213-1216 (1983).

[11] N. Fujimaki, H. Tamura, T. Imamura and S. Hasuo, "Thermal noise-limited sensitivity of the pulse-biased SQUID magnetometer", *J. Appl. Phys.* **65**, 1626-1630 (1989).

[12] O.V. Snigirev, "Ultimate sensitivity of the dc SQUIDs using unshunted Josephson tunnel junctions", *IEEE Trans. Magn.* **19**, 584-586 (1983).

[13] J.D. Feder, M. Klein and C.J. Anderson, "Thermal noise in Josephson devices", *IEEE Trans. Appl. Supercond.* **3**, 2760-2764 (1993).

[14] D.J. Adelerhof, J. Flokstra and H. Rogalla, "Noise in (double) relaxation oscillation SQUIDs", *Physica B* **194-196**, 141-142 (1994).

[15] D.J. Adelerhof, H. Nijstad, J. Flokstra and H. Rogalla, "(Double) relaxation oscillation SQUIDs with high flux-to-voltage-transfer: Simulations and experiments", *J. Appl. Phys.* **76**, 3875-3886 (1994).

[16] J. Kurkijärvi, “Intrinsic fluctuations in a superconducting ring closed with a Josephson junction”, *Phys. Rev. B* **6**, 832-835 (1972).
[17] S.A. Gugoshnikov, O.V. Kaplunenko, Y.V. Maslennikov and O.V. Snigirev, “Noise in relaxation-oscillation driven SQUIDs”, *IEEE Trans. Magn.* **27**, 2439-2441 (1991).
[18] D.J. Adelerhof, M.J. van Duuren, J. Flokstra and H. Rogalla, “High sensitivity magnetic flux sensors with direct voltage readout: Double relaxation oscillation SQUIDs”, *IEEE Trans. Appl. Supercond.* **5**, 2160-2163 (1995).
[19] C.B. Whan and C.J. Lobb, “Complex dynamical behaviour in RCL-shunted Josephson junctions”, *IEEE Trans. Appl. Supercond.* **5**, 3094-3097 (1995).
[20] P.M. Marcus, Y. Imry and E. Ben-Jacob, “Characteristic modes and the transition to chaos of a resonant Josephson circuit”, *Solid State Comm.* **41**, 161-166 (1982).
[21] L.D. Jackel, J.P. Gordon, E.L. Hu, R.E. Howard, L.A. Fetter, D.M. Tennant, R.W. Epworth and J. Kurkijärvi, “Decay of the zero-voltage state in small-area, high-current-density Josephson junctions”, *Phys. Rev. Lett.* **47**, 697-700 (1981).
[22] Superconducting Sensor Laboratory, 2-1200 Muzaigakuendai Inzai, Chiba 270-13, Japan.
[23] F.W. Grover, *Inductance calculations, working formulas and tables*, Dover Publications Inc., New York (1962).
[24] D.J. Adelerhof, M.J. van Duuren, J. Flokstra and H. Rogalla, “Second generation dc SQUID sensors: ROS with frequency readout and DROS with voltage readout”, in *Superconductive Devices and Circuits*, ed. R.A. Buhrman, J. Clarke, K. Daly, R.H. Koch, J.A. Luine and R.W. Simon, proc. SPIE **2160**, 142-153 (1994).
[25] J. Kawai, G. Uehara and H. Kado, “The effects of the self-magnetic fields in relaxation oscillation SQUIDs”, in *Superconductive Devices and Circuits*, eds. R.A. Buhrman, J. Clarke, K. Daly, R.H. Koch, J.A. Luine and R.W. Simon, proc. SPIE **2160**, 154-162 (1994).
[26] Mini-Circuits, P.O. Box 350166, Brooklyn, NY 11235, U.S.A.
[27] R.H. Koch, V. Foglietti, J.R. Rozen, K.G. Stawiasz, M.B. Ketchen, D.K. Lathrop, J.Z. Sun and W.J. Gallagher, “Effects of radio frequency radiation on the dc SQUID”, *Appl. Phys. Lett.* **65**, 100-102 (1994).
[28] G. Uehara, T. Morooka, J. Kawai, N. Mizutani and H. Kado, “Characteristics of the relaxation oscillating SQUID with tunnel junctions”, *IEEE Trans. Appl. Supercond.* **3**, 1866-1869 (1993).
[29] R.L. Peterson and C.A. Hamilton, “Analysis of threshold curves for superconducting interferometers”, *J. Appl. Phys.* **50**, 8135-8142 (1979).
[30] M. Mück and C. Heiden, “Simple dc SQUID system based on a frequency modulated relaxation oscillator”, *IEEE Trans. Appl. Magn.* **25**, 1151-1153 (1989).
[31] M. Mück, H. Rogalla and C. Heiden, “A frequency-modulated read-out system for dc SQUIDs”, *Appl. Phys.* A **47**, 285-289 (1988).
[32] S.A. Gudoshnikov, Yu.V. Maslennikov, V.K. Semenov, O.V. Snigirev and A.V. Vasiliev, “Relaxation-oscillation-driven dc SQUIDs”, *IEEE Trans. Magn.* **25**, 1178-1181 (1989).
[33] D.J. Adelerhof, J. Kawai, G. Uehara and H. Kado, “High sensitivity double relaxation oscillation superconducting quantum interference devices”, *Appl. Phys. Lett.* **65**, 2606-2608 (1994).
[34] D.J. Adelerhof, J. Kawai, G. Uehara and H. Kado, “High sensitivity double relaxation oscillation superconducting quantum interference devices with large transfer from flux to voltage”, *Rev. Sci. Instrum.* **66**, 2631-2637 (1995).
[35] G. Fontana, R. Mezzena, S. Vitale, M. Cerdonio, M. Mück, G. Hallmanns and C. Heiden, “Improved sensitivity of planar microwave biased rf SQUIDs using a cryogenic HEMT preamplifier”, *IEEE Trans. Appl. Supercond.* **3**, 1820-1823 (1993).

Chapter 4

Double Relaxation Oscillation SQUIDs

Unlike the relaxation oscillation SQUID (ROS), the *double* relaxation oscillation SQUID (DROS) is used with voltage readout instead of frequency readout. Therefore, simple twisted wires can be used for its readout, as opposed to the coaxial transmission lines which are required for the readout of a ROS. The large flux-to-voltage transfer of a DROS, typically $\partial V/\partial \Phi_{sig} = 1$ mV/Φ_0, enables direct voltage detection with a room temperature dc amplifier without degradation of the sensitivity. Thus, flux modulation techniques and resonant impedance matching circuitry are not required and the flux locked loop electronics can be simple and compact, which is an important feature, especially in multi-channel SQUID systems. Moreover, wide bandwidth operation is easier to accomplish with a non-modulated readout scheme and the crosstalk between adjacent channels is also reduced.

The principle of operation of the DROS has already been treated roughly in section 2.5.4. A more thorough discussion will be given in section 4.1. Like for ROSs, the optimum relaxation frequency for DROSs is also in the lower GHz range. As has been confirmed experimentally [1,2], the sensitivity of a DROS with this relaxation frequency is of the same order as that of a comparable non-hysteretic dc SQUID with resistively shunted tunnel junctions.

To demonstrate the practical applicability of DROSs, we constructed a number of DROS-based measuring systems, which will be presented in this chapter. First, in section 4.2, a three-channel DROS gradiometer with wire-wound pickup coils will be discussed. Operated inside a superconducting shielding, this first-order gradiometer system had a white magnetic field noise of $\sqrt{S_B} = 4$ fT/$\sqrt{}$Hz (10 fT/$\sqrt{}$Hz @ 1 Hz) [3]. For comparison, a magnetic field noise level of 10 fT/$\sqrt{}$Hz in a frequency band between 1 Hz and 1 kHz is generally considered to be sufficient for bio-magnetic measurements, such as magneto-encephalography (MEG) [4]. Next, in section 4.3, a DROS with a gradiometric

signal SQUID will be presented. Connected to an external planar first-order gradiometer, this device had a magnetic field sensitivity better than 2 fT/√Hz (~10 fT/√Hz @ 1 Hz) inside a magnetically shielded room [5]. The third example of a practical DROS system is the 8 x 8 mm² directly coupled multi-loop DROS magnetometer which is discussed in section 4.4. Unlike the systems presented in sections 4.2 and 4.3, this device did not require an external superconducting flux transformer to enlarge its effective pickup area. Inside a superconducting shielding, the white magnetic field noise of the directly coupled DROS was 7 fT/√Hz [6].

In section 4.5, a DROS is used as a current sensor with a sensitivity better than 2 pA/√Hz. To demonstrate this sensitivity, the subgap *I-V* characteristic of a voltage biased Nb/Al,AlO_x/Al/Nb tunnel junction was measured. This type of measurement is for instance of relevance for the readout of X-ray spectrometers based on superconducting tunnel junctions or hot electron bolometers. In section 4.6, the results of this chapter are summarized.

4.1 Operation theory of the DROS

A DROS consists of two hysteretic dc SQUIDs in series, shunted by an inductor L_{sh} and a resistor R_{sh}, as shown in the scheme of Fig. 4.1a. If the device is biased with an appropriate dc bias current I_b, relaxation oscillations are generated according to the same conditions which hold for a ROS, cf. Eq. (3.4).

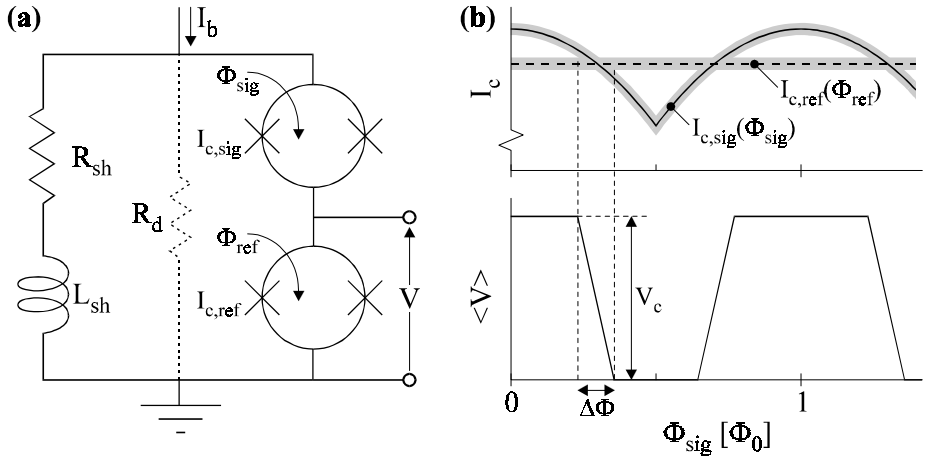

Figure 4.1 **(a)** *Schematic representation of a DROS.* **(b)** *Schematic I_c-Φ_{sig} and <V>-Φ_{sig} characteristics of a DROS. The shaded region around the I_c-Φ_{sig} traces represents the thermal critical current noise of both hysteretic dc SQUIDs.*

As for a ROS, parasitic resonances in the L-C-R circuit constituted by the shunt inductor (L_{sh}), the capacitance of the SQUIDs (C_{sq}) and the shunt resistor (R_{sh}) can be suppressed with an optional damping resistor R_d. For adequate damping of the L_{sh}-C_{sq} resonances, the resistor R_d should be dimensioned such that the damping parameter D, defined in Eq. (3.1), is larger than unity.

The signal flux Φ_{sig} is applied to the upper SQUID, the *signal SQUID*, whereas a constant reference flux Φ_{ref} is used to adjust the critical current of the other SQUID, the *reference SQUID*, to a value in the middle of the critical current modulation range of the signal SQUID. This is indicated in the schematic I_c-Φ_{sig} plot of Fig. 4.1b.

Basically, in each relaxation oscillation cycle, the critical currents of the two hysteretic dc SQUIDs are compared. If $I_{c,sig}(\Phi_{sig}) < I_{c,ref}$, only the signal SQUID participates in the relaxation oscillations and the reference SQUID remains superconducting. Consequently, in this situation, the output voltage of the DROS, which is measured across the reference SQUID, is equal to zero. On the other hand, for values of the signal flux giving $I_{c,sig}(\Phi_{sig}) > I_{c,ref}$, only the reference SQUID oscillates, and the DROS output consists of voltage pulses at the relaxation frequency. Since the bandwidth of the readout amplifier is smaller than the relaxation frequency typically by a few orders of magnitude, the pulsed nature of the output voltage is not observed, and only the time-averaged voltage $\langle V \rangle$ is measured. Thus, depending on the value of Φ_{sig}, the time-averaged DROS output equals either zero or has a certain value, labeled V_c. The transition between these two states at $I_{c,sig}(\Phi_{sig}) = I_{c,ref}$ is very sharp, resulting in a large flux-to-voltage transfer, as illustrated by the schematic $\langle V \rangle$-Φ_{sig} characteristic in Fig. 4.1b.

4.1.1 Voltage modulation depth

The theoretical maximum bias current $I_{b,max}$ at which a DROS still operates correctly can be determined from the operation criterion of Eq. (3.4), substituting $I_c = 2I_0$:

$$I_{b,max} = \frac{2I_0}{\sqrt{\beta_C^*}} = \frac{1}{R_{sh}} \cdot \sqrt{\frac{I_0 \Phi_0}{\pi C_{sq}}} \quad \text{with} \quad \beta_C^* = \frac{2\pi \cdot 2I_0 \cdot R_{sh}^2 \cdot C_{sq}}{\Phi_0}. \tag{4.1}$$

In Eq. (4.1), I_0 represents the critical current of one Josephson junction and C_{sq} is the SQUID capacitance. To ensure proper operation, β_C^* is designed much smaller than unity in most practical DROSs. Hence, in practice, $I_{b,max} \approx 2I_0$. This is in contrast with conventional dc SQUIDs, which are generally biased at a bias current slightly above $2I_0$.

If the reference SQUID oscillates, the time-averaged output voltage of the DROS equals that of a ROS with identical parameters. The ROS I-V characteristic of Fig. 3.8a shows that $\langle V \rangle$ approaches $I_b \cdot R_{sh}$ for $I_b \approx 2I_0$. For smaller bias currents, $\langle V \rangle$ is somewhat below this asymptotic value, and at

$I_b \approx I_{b,max}$, $\langle V \rangle = (0.5 \,..\, 0.75) \cdot I_b \cdot R_{sh}$ [2]. Combined with Eq. (4.1), this yields the following expression for the theoretical maximum output voltage swing of a DROS:

$$V_{c,max} = (0.5 \,..\, 0.75) \cdot I_{b,max} \cdot R_{sh} = (0.5 \,..\, 0.75) \cdot \sqrt{\frac{I_0 \Phi_0}{\pi C_{sq}}} \,. \tag{4.2}$$

Equation (4.2) shows that the modulation depth of the V-Φ_{sig} characteristic does not depend on the signal SQUID inductance, at least when noise effects are not taken into consideration.

4.1.2 Flux-to-voltage transfer

At 4.2 K, where the thermal limit applies, the flux-to-voltage transfer of a well damped DROS is limited by the thermally induced critical current spread of both SQUIDs. In Fig. 4.1b, this spread is symbolized by the shaded region around the traces. Assuming a linear transition between $\langle V \rangle = 0$ and $\langle V \rangle = V_c$, the flux-to-voltage transfer is given by

$$\frac{\partial V}{\partial \Phi_{sig}} = \frac{V_c}{\Delta \Phi}, \tag{4.3a}$$

where $\Delta\Phi$ represents the width of the transition, as indicated in Fig. 4.1b. The transition width $\Delta\Phi$ is related to the spread in the critical currents via

$$\Delta \Phi = \frac{\Delta I_{c,ref} + \Delta I_{c,sig}}{\left(\partial I_{c,sig} / \partial \Phi_{sig} \right)}, \tag{4.3b}$$

where $\Delta I_{c,ref}$ and $\Delta I_{c,sig}$ are the thermal spreads of the critical currents of the reference SQUID respectively the signal SQUID. Evaluating these spreads with the single junction approximation, by substituting a critical current of $2I_0$ in Eq. (3.9), Eq. (4.3a) can be rewritten as

$$\frac{\partial V}{\partial \Phi_{sig}} = g \cdot \frac{I_0^{2/3}}{\left(1 + \beta_{L,sig} \right)} \cdot \frac{V_c}{\Phi_0}, \quad g \approx \frac{1.7}{\alpha} = 7 \cdot 10^4 \ \mathrm{A}^{-2/3} \ @ \ 4.2 \ \mathrm{K}, \tag{4.3c}$$

where Eq. (3.11) has been used to calculate $\partial I_{c,sig} / \partial \Phi_{sig}$. The parameter α was previously introduced in Eq. (3.9) and has a $T^{2/3}$ temperature dependence. Therefore, the parameter g in Eq. (4.3c) varies as $T^{-2/3}$ with temperature.

Thus, at $T = 4.2$ K, a DROS with $I_0 = 10$ μA, $\beta_{L,sig} = 1$ and a SQUID capacitance of 1 pF theoretically has an output voltage swing of ~50 μV [from Eq. (4.2)] and a flux-to-voltage transfer of approximately 800 $\mu V / \Phi_0$ [from Eq. (4.3c)]. For comparison, a non-hysteretic dc SQUID with the same

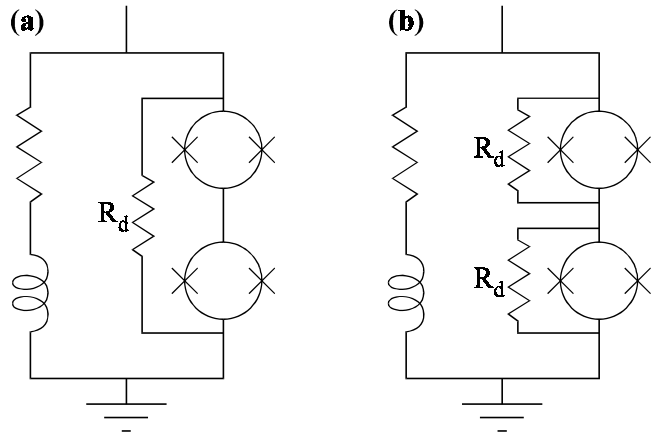

Figure 4.2 *Two possible damping configurations for a DROS.*

critical current and inductance, having junction shunt resistors of 4 Ω (β_C = 0.25), has a flux-to-voltage transfer coefficient of only ~80 μV/Φ_0, according to Eq. (2.16).

For some DROSs, we experimentally observed a degradation of the flux-to-voltage transfer due to the Johnson noise of R_d [6]. The magnitude of this reduction of $\partial V/\partial\Phi_{sig}$ depends on the exact layout of the damping circuit. As an example, Fig. 4.2 shows two possible configurations. In Fig. 4.2a, one damping resistor shunts both SQUIDs, and in Fig. 4.2b, each SQUID is shunted by a separate damping resistor.

In the configuration of Fig. 4.2a, the Johnson noise generated in R_d flows through both SQUIDs, and consequently the additional noise currents through both SQUIDs are correlated. Therefore, the relative switching probabilities of the SQUIDs are hardly influenced and a severe degradation of $\partial V/\partial\Phi_{sig}$ is not likely. In the configuration of Fig. 4.2b, however, the Johnson noise currents through both SQUIDs are not correlated. This results in an additional spread of the critical currents of both SQUIDs, superimposed on the thermal spread. According to Eqs. (4.3a) and (4.3b), this increased critical current spread decreases the flux-to-voltage transfer $\partial V/\partial\Phi_{sig}$. In section 4.4.2, this negative side effect of the damping resistors will be discussed in more detail.

4.1.3 Sensitivity

The maximum flux-to-voltage transfer is obtained at those values of Φ_{sig} where the critical currents of the reference SQUID and of the signal SQUID are equal. At these points, both SQUIDs have a switching probability of 50% in each relaxation cycle. Consequently, the average voltage over a time span $\Delta t \gg 1/f_{RO}$ is $\frac{1}{2}V_c$, with a standard deviation of $\frac{1}{2}V_c/\sqrt{(f_{RO}\cdot\Delta t)}$. For frequencies much lower than the relaxation frequency, this implies a voltage noise at the DROS output of

$$S_V = \frac{V_c^2}{4 f_{RO}}. \tag{4.4a}$$

From Eqs. (4.4a) and (4.3c), the equivalent flux noise can be calculated:

$$S_\Phi = \frac{S_V}{\left(\partial V / \partial \Phi_{sig}\right)^2} \approx \chi_{dros} \cdot \frac{\left(1+\beta_{L,sig}\right)^2 \cdot \Phi_0^2}{f_{RO} \cdot I_0^{4/3}} \quad ,$$

$$\chi_{dros} = \frac{1}{4g^2} \approx 5.1 \cdot 10^{-11}\ \mathrm{A}^{4/3}\ @\ 4.2\ \mathrm{K}\ . \tag{4.4b}$$

As $g \propto T^{-2/3}$, Eq. (4.4b) implies that, according to the present model, the flux noise S_Φ of a DROS scales with temperature as $T^{4/3}$. This is close to the $T^{6/5}$ temperature dependence which was derived analytically in ref. [7].

Equation (4.4b) shows a strong analogy with Eq. (3.10b), expressing the sensitivity of a ROS. As for a ROS, the sensitivity of a DROS also improves at higher relaxation frequencies. However, the sensitivity can not be improved infinitely by taking increasingly higher values for the relaxation frequency. Numerical simulations show that the flux-to-voltage transfer decreases below the thermally limited value of Eq. (4.3c) when f_{RO} exceeds a few percent of the plasma frequency of the junctions [8], which impedes a further reduction of the flux noise level. With a typical plasma frequency of 100 GHz, the optimum relaxation frequency is therefore about 1 GHz for most practical DROSs. According to Eq. (4.4b), at T = 4.2 K, a DROS with f_{RO} = 1 GHz, $\beta_{L,sig}$ = 1 and I_0 = 10 μA has a thermally limited flux noise of $\sqrt{S_\Phi}$ = 1 $\mu\Phi_0/\sqrt{\mathrm{Hz}}$ (ε = 30 h).

The sensitivity of a DROS is also influenced by the Johnson noise generated by the resistors R_{sh} and R_d. As was discussed in section 4.1.2, the Johnson noise from the damping resistance R_d may decrease the flux-to-voltage transfer. As Eq. (4.4b) implies that the flux noise spectral density is inversely proportional to $(\partial V/\partial \Phi_{sig})^2$, this reduction of the transfer function of the DROS directly results in a worse sensitivity.

The Johnson noise of R_{sh} causes a voltage noise of $S_V = (4k_B T/R_{sh}) \cdot R_{dyn}^2$ at the output, with R_{dyn} the dynamic resistance $\partial V/\partial I_b$ of the DROS. Using the approximation $R_{dyn} \approx R_{sh}$, a shunt resistor with a typical value of R_{sh} = 1 Ω contributes to the output voltage noise by an amount of only 15 $\mathrm{pV}/\sqrt{\mathrm{Hz}}$. This is much less than the contribution of other noise sources, such as the input voltage noise of the pre-amplifier, which is of the order of 1 $\mathrm{nV}/\sqrt{\mathrm{Hz}}$. From this example, one can conclude that the Johnson noise generated by R_{sh} is not a major noise source in a DROS. Furthermore, the Johnson noise of R_{sh} is low pass filtered by the L-R circuit constituted by L_{sh} and R_{sh}, which prevents degradation of the DROS performance due to downmixing with the Josephson oscillations in the junctions.

4.1.4 Experimental verification

In order to verify the theory discussed in the previous sections, Adelerhof *et al.* [1,2] have fabricated and characterized DROSs with various parameters at the Superconducting Sensor Laboratory in Japan [9]. In this section, their main results are summarized.

The layout and design parameters of the DROSs were equivalent to the 1 GHz and 10 GHz ROSs presented and discussed in chapter 3. Like these ROSs, they did not have multi-turn input coils, and the signal flux was applied by means of a half-turn input coil. The average experimental $\partial V/\partial\Phi_{sig}$ of the nine characterized 1 GHz DROSs was 4.2 mV/Φ_0 (standard deviation: 1.1 mV/Φ_0), which is close to the theoretical value of ~5 mV/Φ_0 [from Eqs. (4.3c) and (4.2)]. The flux-to-voltage transfer of the 10 GHz DROSs was somewhat smaller: 2.6 mV/Φ_0 on the average. This is probably caused by the interaction between the relaxation oscillations and the plasma oscillations at elevated relaxation frequencies.

For the 1 GHz DROSs, the value of the damping parameter D had a clear influence on the sensitivity. Generally, the energy resolution improved by a factor of 2 to 3 when D was increased from 0.1 to 10. This clearly indicates the positive effect of damping of the L_{sh}-C_{sq} resonances. For the 10 GHz DROSs, however, the amount of damping did not change the sensitivity significantly. This is another indication that the sensitivity of the 10 GHz devices is limited by interference of the plasma oscillations and the relaxation oscillations.

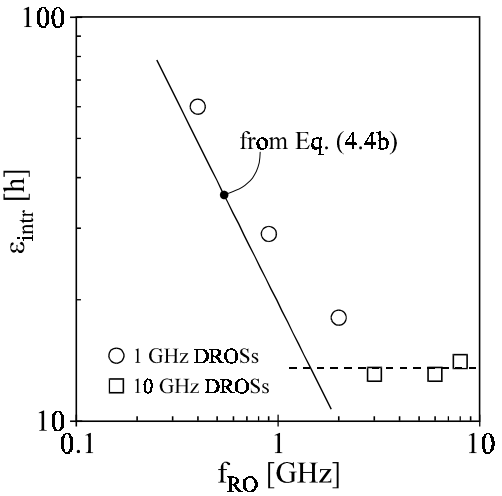

Figure 4.3 *Theoretical (solid line) and experimental (markers) intrinsic energy sensitivity of 1 GHz and 10 GHz DROSs versus the calculated relaxation frequency. Data from ref. [2].*

Figure 4.3 shows the intrinsic energy resolution ε_{intr} of three 1 GHz DROSs and three 10 GHz DROSs as a function of the calculated relaxation frequency f_{RO} [2]. The intrinsic noise was measured in open loop, subtracting the pre-amplifier noise. The solid line in Fig. 4.3 was calculated with Eq. (4.4b). For relaxation frequencies below approximately 2 GHz, the difference between theory and experiment is only about 10 h. At higher relaxation frequencies, the measured sensitivity levels off at 13 .. 14 h. These results show that the theory in the previous sections is reasonably accurate as long as the relaxation frequency does not exceed ~1% of the plasma frequency.

Due to the noise of the room-temperature amplifier (1.5 nV/√Hz in the white region), the energy sensitivity of the DROSs in flux locked loop (FLL) was worse than the intrinsic sensitivities depicted in Fig. 4.3. The best measured energy resolution in FLL was 34 h, at f_{RO} = 1 .. 2 GHz.

As already mentioned, the DROSs used in these experiments had no tightly coupled multi-turn input coils. In the next sections, some DROS designs with multi-turn input coils will be discussed.

4.2 A three-channel DROS gradiometer

In this section, the construction and operation of a three-channel DROS first-order gradiometer system with wire-wound pickup coils is discussed. The DROSs in this system are identical to those used in a single-channel planar gradiometer system that was constructed by Adelerhof *et al.* [10] at the Superconducting Sensor Laboratory. With that system, which had a white magnetic field sensitivity of $\sqrt{S_B}$ = 5 fT/√Hz, magneto-encephalograms (MEG) of auditory evoked responses were measured in a magnetically shielded room. This proves the applicability of DROSs for bio-magnetic measurements. However, the results obtained with this single-channel system do not make clear whether interference between relaxation oscillations in adjacent DROSs, caused by crosstalk via the flux transformers, could lead to a degradation of the sensitivity in multi-channel DROS magnetometer systems. The three-channel gradiometer system which is discussed here was primarily constructed to examine this aspect of multi-channel DROS magnetometry.

4.2.1 DROS layout

A micrograph and the corresponding circuit of the DROSs are shown in Fig. 4.4. The Nb/Al,AlO_x/Nb Josephson tunnel junctions, the Nb structures and the SiO_2 insulating layer were patterned by reactive ion etching in a CF_4 plasma. The Al resistors were defined by wet chemical etching in a NaOH solution.

The size of the hole in the signal SQUID washer is 100 µm, which corresponds to an inductance of ~160 pH according to Eq. (2.19). The actual SQUID inductance, determined from the experimental critical current modulation depth, was $L_{sq,sig}$ = 240 pH. It is realistic to attribute the difference

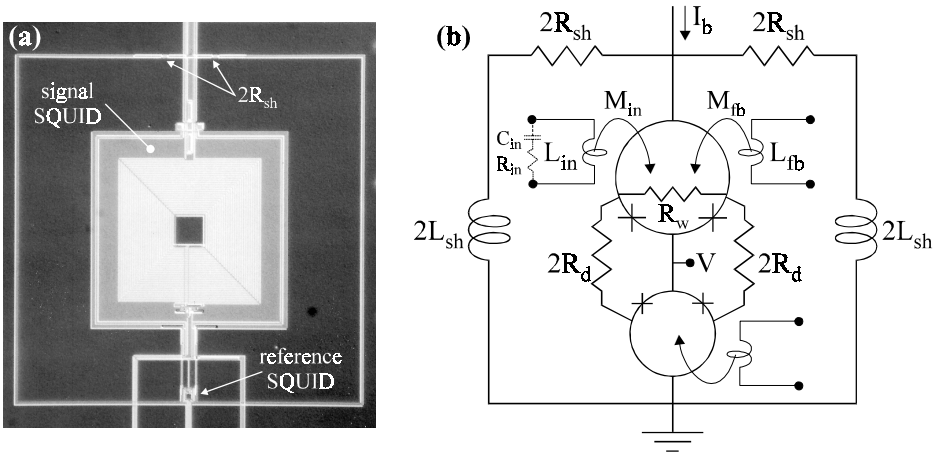

Figure 4.4 **(a)** *Micrograph and* **(b)** *scheme of the DROSs used in the three-channel gradiometer system. The bonding pads are not shown on the photograph. The chip size, including the bonding pads, is 2.5 x 4 mm².*

of 80 pH to the parasitic inductance of the double 2-µm-wide and 250-µm-long slit in the washer [11]. The 25-turns input coil on top of the signal SQUID has a designed inductance of L_{in} = 100 nH [from Eq. (2.20a)]. The experimentally determined mutual inductance between the input coil and the signal SQUID is M_{in} = 4.1 nH. This corresponds to a coupling coefficient of $k = M_{in}/\sqrt{(L_{sq} \cdot L_{in})} = 0.84$, if the design value of 100 nH is substituted for L_{in}. The mutual inductance between L_{sq} and the single-turn feedback coil at the edge of the washer was measured to be M_{fb} = 220 pH. The 2 x 2 µm² Josephson junctions, located at the outer side of the washer, have a critical current of I_0 = 5.5 µA and an estimated capacitance of C_j = 0.25 pF per junction.

The Josephson junctions of the reference SQUID are slightly larger than the junctions of the signal SQUID (2.2 x 2.2 µm² instead of 2 x 2 µm²), and therefore have a larger critical current, viz. 6.5 µA per junction. The small design value of the reference SQUID inductance, $L_{sq,ref}$ = 32 pH, gives $\beta_{L,ref} \approx 0.2$. This small value of β_L ensures that the modulation range of $I_{c,ref}$ covers the modulation range of $I_{c,sig}$ completely. The reference flux is applied via a single-turn input coil on top of the reference SQUID.

The inductive shunt, having an estimated value of L_{sh} = 1 .. 1.5 nH, is distributed over two branches in order to reduce the magnetic coupling with the SQUIDs. In each branch, a resistor of 2 Ω is implemented, making R_{sh} = 1 Ω. With this shunt resistance, Eq. (4.1) yields an effective McCumber parameter of β_C^* = 0.017 and a theoretical maximum bias current of $I_{b,max}$ = 85 µA. The time constant L_{sh}/R_{sh} of about 1 ns implies a relaxation frequency of about 1 GHz. According to Eq. (4.4b), the theoretical flux noise level at f_{RO} = 1 GHz is 1.7 $\mu\Phi_0/\sqrt{\text{Hz}}$.

Signal SQUID			**Reference SQUID**		
junction size	2 x 2	μm^2	junction size	2.2 x 2.2	μm^2
$2I_0$	11	μA [b]	$2I_0$	13	μA [b]
C_{sq}	0.5	pF [a]	hole size	20	μm
hole size	100	μm	$L_{sq,ref}$	32	pH [a]
$L_{sq,sig}$	240	pH [b]	$\beta_{L,ref}$	~0.2	[a]
$\beta_{L,sig}$	~1.3	[b]			
R_w	3	Ω [a]			
Input coil			**Relaxation circuit**		
# turns	25		L_{sh}	1 .. 1.5	nH [a]
line width	4	μm	R_{sh}	1	Ω [b]
L_{in}	100	nH [a]	β_{C^*}	0.017	[a]
M_{in}	4.1	nH [b]	R_d	15	Ω [a]
k	0.84		D	2 .. 3	[a]

[a] Design / calculated value.
[b] Experimental value.

Table 4.1 *Main parameters of the DROSs used in the three-channel gradiometer system.*

Resonances between L_{sh} and C_{sq} are suppressed with two parallel resistors of 30 Ω each. The resulting damping resistance of $R_d = 15\ \Omega$ implies a damping parameter of $D \approx 2.5$, which indicates sufficient suppression of L_{sh}-C_{sq} resonances. To avoid L-C resonances in the signal SQUID - between the SQUID inductance and the capacitance of the Josephson junctions - the SQUID inductance is shunted with a resistor $R_w = 3\ \Omega$ [12]. This resistance is a trade-off between sufficient damping - requiring $R_w < \sqrt{(L_{sq}/2C_j)} = 22\ \Omega$ - and acceptable additional flux noise due to the Johnson noise, $L_{sq}\cdot\sqrt{(4k_BT/R_w)} = 1\ \mu\Phi_0/\sqrt{\text{Hz}}$ for $R_w = 3\ \Omega$.

The main parameters of the DROSs are summarized in Table 4.1.

4.2.2 Characterization of the DROSs without pickup coils

Before being connected to the pickup coils, the DROSs were characterized without flux transformers in a stainless steel ^{4}He bath cryostat. The scheme of the characterization setup is given in Fig. 4.5. Up to four samples were mounted on an epoxy printed circuit board (PCB) with GE-7031 varnish. The samples were shielded from external noise sources by a superconducting Nb can with a length of 19 cm and a diameter of 6 cm. Moreover, the entire cryostat was surrounded by a cylindrical μ-metal shield at room temperature.

Twisted pairs, shielded by a grounded stainless steel tube, were used to connect the DROSs to the room temperature electronics. At the top of the insert, L-C-R low pass filters prevented degradation of the DROS performance

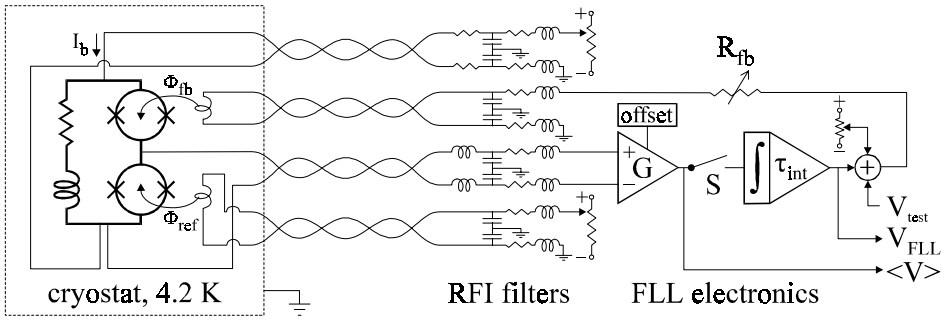

Figure 4.5 *Scheme of the DROS flux locked loop electronics.*

due to radio frequency interference (RFI) [13]. The filters in the wires for the bias current and the reference flux had a cutoff frequency below 25 kHz. To enable wide bandwidth operation, the cutoff frequency of the RFI filters in the voltage readout and feedback flux lines was about 1 MHz. The optimum filter configuration was determined by trial and error. The application of additional cooled filters close to the DROSs did not improve the characteristics.

The output voltage of the DROSs was measured directly with a room temperature differential pre-amplifier, having a bandwidth of about 250 kHz. The white input voltage noise of this amplifier, based on LT 1028 op-amps [14], was e_n = 1.8 nV/√Hz (5 nV/√Hz @ 1 Hz), and the gain was adjustable between $G = 2 \cdot 10^2$ and $G = 2 \cdot 10^5$. The white current noise of the amplifier amounted to i_n = 2 pA/√Hz and below approximately 500 Hz, it increased with a 1/f character to ~30 pA/√Hz at 1 Hz. To minimize the noise contribution of i_n, the resistance of the voltage readout circuit was reduced by using copper wiring (instead of manganin, which was used for the other leads) and low-ohmic RFI filters.

The time constant of the integrator was adjustable to $\tau_{int} = 10^{-2}$, 10^{-3} or 10^{-4} s, and the feedback resistor R_{fb} was tuned to yield a flux locked loop transfer function of $\partial V_{FLL}/\partial \Phi_{sig} = R_{fb}/M_{fb} = 1\ \mathrm{V}/\Phi_0$. For testing purposes, a test signal V_{test} could be added to the output of the integrator. With switch S opened, V_{test} was used to record the open loop V-Φ_{sig} characteristics of the DROSs. The test input was also used to check the locking when the FLL was closed.

For signals not exceeding the maximum slew rate $(\partial \Phi_{sig}/\partial t)_{max}$, given by

$$\left(\frac{\partial \Phi_{sig}}{\partial t}\right)_{max} = \frac{V_c \cdot G \cdot M_{fb}}{2 \cdot \tau_{int} \cdot R_{fb}}, \tag{4.5}$$

the bandwidth f_{max} of the FLL is

$$f_{max} = \frac{G \cdot M_{fb}}{2\pi \cdot \tau_{int} \cdot R_{fb}} \cdot \left(\frac{\partial V}{\partial \Phi_{sig}}\right)_{DROS}. \tag{4.6}$$

Equations (4.5) and (4.6) do not take into account “parasitic” phase shifts, e.g. due to the delay times in the leads, and do therefore not hold at elevated signal frequencies. In ref. [15], a thorough discussion of the dynamics of a FLL with direct voltage readout is given. For APF SQUIDs operated in a FLL comparable to that of Fig. 4.5, a bandwidth of 11 MHz has been reported [16].

During the first experiments, it appeared that both the flux-to-voltage transfer and the flux noise of the DROSs improved considerably when an external R_{in}-C_{in} shunt was connected across the input coil [10]. This is very likely due to attenuation of input coil resonances [17]. In Fig. 4.4b, this input coil shunt circuit, which was implemented with surface mounted devices (SMD), is indicated with dotted lines. The best results were obtained with $R_{in} = 150\ \Omega$ and $C_{in} = 1$ nF. With these values, the flux-to-voltage transfer increased by a factor of 3 and the flux noise decreased by a factor of 1.5. When R_{in} was reduced below 150 Ω, the low frequency flux noise increased despite the dc blocking capacitor C_{in}. This may be caused by downmixing of high frequency Johnson noise generated by R_{in}. All subsequent measurements were performed with a shunt of $R_{in} = 150\ \Omega$ and $C_{in} = 1$ nF across the input coil.

The minimum flux noise in FLL was obtained for bias currents around 100 μA, which is close to the theoretical maximum operation current of 85 μA. At $I_b \approx 100$ μA, the output voltage modulation depth ranged from 60 to 80 μV and the experimental values for the flux-to-voltage transfer were between 0.5 and 1 mV/Φ_0. This is in good agreement with Eq. (4.3c), which predicts a transfer coefficient of $\partial V/\partial\Phi_{sig} \approx 0.7$ mV/Φ_0. At larger bias currents, the DROSs still operated, and the flux-to-voltage transfer even increased to ~4 mV/Φ_0 at $I_b \approx 150$ μA, as shown in the experimental V-Φ_{sig} characteristic of Fig. 4.6. However, at such large bias currents, the flux noise of the devices was considerably worse than at $I_b \approx 100$ μA.

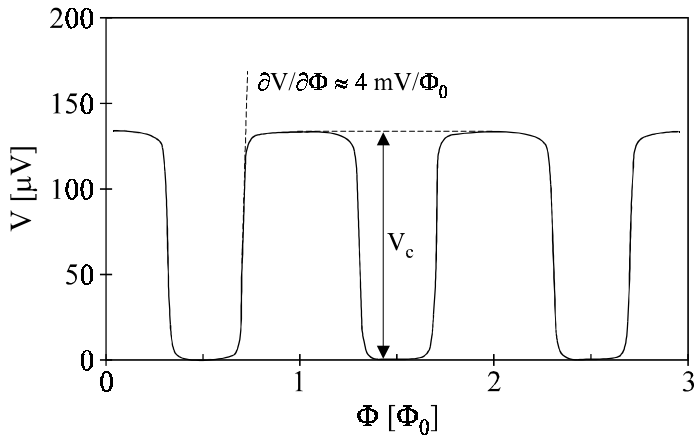

Figure 4.6 *Measured V-Φ_{sig} characteristic of one of the DROSs of the three-channel system at a bias current of approximately 150 μA.*

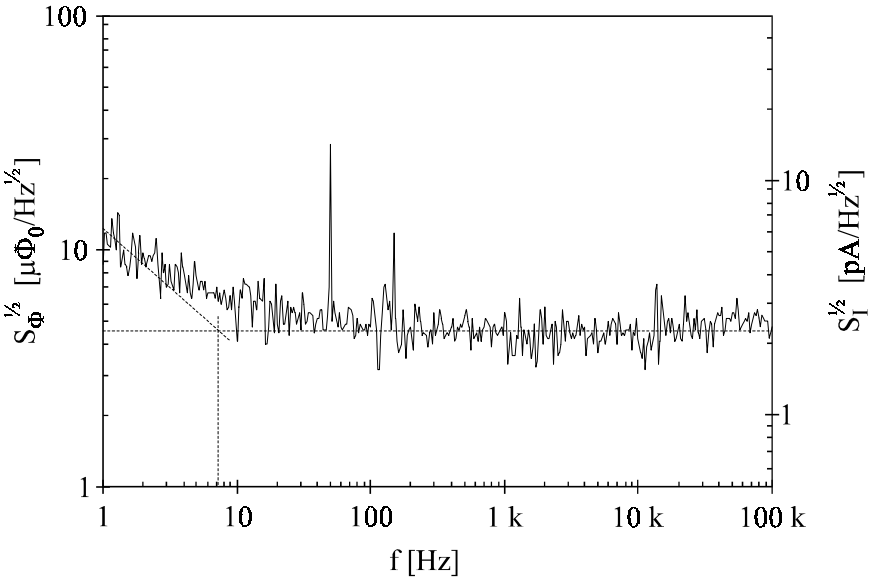

Figure 4.7 *Flux noise spectrum of a DROS operated in flux locked loop. The left vertical axis represents the flux noise, whereas the right vertical axis gives the equivalent current noise, referred to the input coil.*

A typical noise spectrum in FLL is shown in Fig. 4.7. The spectrum was recorded with a HP 3562A spectrum analyzer. The white noise level of $\sqrt{S_\Phi} = 4.5\ \mu\Phi_0/\sqrt{\text{Hz}}$ corresponds to an energy sensitivity of $\varepsilon = S_\Phi/2L_{sq,sig} = 275\ h$. At lower frequencies, the flux noise increases with a 1/f character and at 1 Hz, $\sqrt{S_\Phi} \approx 10\ \mu\Phi_0/\sqrt{\text{Hz}}$. The 1/f corner frequency of about 7 Hz is indicated in Fig. 4.7. The right vertical axis of Fig. 4.7 gives the equivalent current noise, referred to the input coil, $\sqrt{S_I} = \sqrt{S_\Phi}/M_{in}$. In the white region, the current sensitivity is about 2.3 pA/√Hz (5.5 pA/√Hz @ 1 Hz), and the coupled energy sensitivity, given by Eq. (2.21), amounts to $\varepsilon_{coupl} \approx 400\ h$.

4.2.3 Design of the flux transformers and the three-channel insert

After characterization, the DROSs were mounted in a three-channel insert. This insert, made of textile reinforced epoxy, was designed for use in a fiber glass liquid helium cryostat with a neck diameter of 5 cm [18]. The three wire-wound first-order pickup coils were arranged in a triangular configuration with an intermediate spacing of less than 1 mm, which is small compared to the pickup coil diameter of 20 mm. The pickup coils touched the bottom of the cryostat, and axial mechanical tensions during cool-down were prevented by the telescopic structure of their suspension.

The first-order gradiometric pickup coils consisted of 100 µm thick Nb wires, wound around a textile reinforced epoxy core with a diameter of 20 mm. A

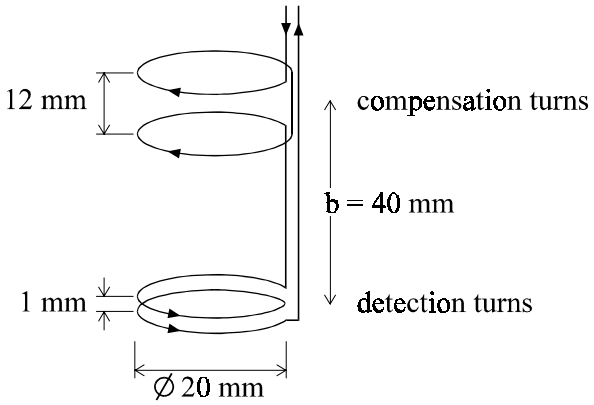

Figure 4.8 *Scheme of one of the wire-wound gradiometers of the three-channel DROS system.*

schematic picture of one pickup coil is given in Fig. 4.8. The calculated self inductance of the pickup coils is L_{pu} = 0.35 µH, the baseline is b = 40 mm, and the geometric sensing area amounts to A_{pu} = 6.3 cm^2.

Unshielded twisted Nb wires (∅ 100 µm) were used to connect the pickup coils to the input coils of the DROSs, which were mounted about 15 cm above the pickup section in three separate cylindrical Nb/Pb shielding modules. Inside these modules, the Nb wires from the pickup coils were fixed with screws to small Nb blocks. The superconducting contacts between these blocks and the input coils of the DROSs were made with 50 µm thick Nb wires which were ultrasonically bonded to the contact pads of the input coils. In order to enable bonding, the Nb wires were annealed under vacuum conditions [19]. The SMD R_{in}-C_{in} input coil shunts, located close to the DROSs inside the shielding modules, not only damped the resonances in the input coil, but also constituted low pass filters with a cutoff frequency of 250 to 300 MHz. In this way, the radio frequency magnetic noise sensed by the pickup coils was attenuated.

The *effective area*, A_{eff}, of the flux transformer circuit is given by

$$A_{eff} = \frac{\partial \Phi_{sig}}{\partial B} = \frac{A_{pu} \cdot M_{in}}{L_{in} + L_{pu} + L_{par}}, \tag{4.7}$$

with A_{pu} the geometric sensing area of the pickup coils (6.3 cm^2) and L_{par} the parasitic inductance in the transformer circuit. This parasitic inductance is mainly caused by the 15-cm-long twisted wires between the pickup coils and the DROSs. In Eq. (4.7), B represents the difference between the magnetic field sensed by the detection turns and the magnetic field sensed by the compensation turns of the gradiometers.

The three DROSs were connected to the room temperature FLL electronics with twisted wires, shielded by stainless steel capillaries and equipped with low pass RFI filters at room temperature. Each channel had its own FLL electronics in a separate aluminium box on top of the cryostat. The whole system was operated in a magnetically shielded room (MSR) [20]. To reduce the amount of radio frequency radiation inside the shielded room, the shields of all coaxial cables entering the room were grounded to the wall of the MSR. One common power supply, outside the MSR, was used for the three channels. In order to prevent excessive 50 Hz noise due to ground loops, the power lines for the three electronic boxes were split inside the MSR.

4.2.4 Characterization of the three-channel DROS gradiometer

During the first tests of the system, the pickup coils were shielded with a superconducting Pb can. A typical V-Φ_{sig} characteristic, measured with this configuration, is plotted as trace (a) in Fig. 4.9. The horizontal scale of Fig. 4.9 is not in units of flux, but in terms of the current through the feedback coil, I_{fb}. As a reference, the V-Φ_{sig} characteristic of the bare DROS without pickup coil is plotted in trace (b). Because trace (a) was measured at a bias current of about 100 μA, the modulation depth and the flux-to-voltage transfer are smaller than those of trace (b), which was recorded at $I_b \approx 150$ μA.

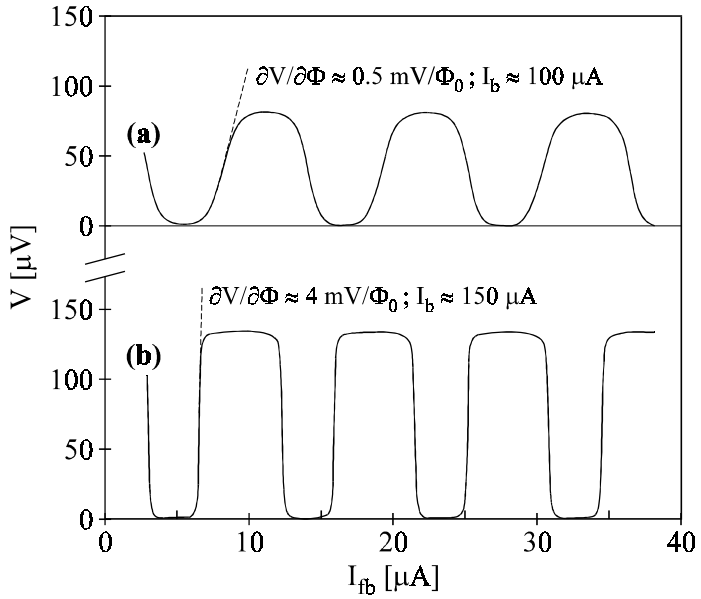

Figure 4.9 **(a)** *V-Φ_{sig} characteristic of a DROS after connecting the input coil to a shielded pickup coil.* **(b)** *V-Φ_{sig} characteristic before connection of the pickup coil. The horizontal axis gives the current through the feedback coil of the DROS.*

From the periodicity of the V-Φ_{sig} characteristics, it can be deduced that M_{fb}, the mutual inductance between the feedback coil and the signal SQUID, decreased from M_{fb} = 220 pH to M_{fb} = 183 pH when the pickup coil was connected. This is due to the reduction of the effective signal SQUID inductance which is *screened* by the closed superconducting input circuitry. The occurrence of this screening effect at low frequencies demonstrates that all contacts in the flux transformer circuit are superconducting.

Figure 4.10 shows the flux noise spectrum of one of the channels, still with shielded pickup coils. For reference, the flux noise of the same DROS, but without pickup coil, is also plotted. Notwithstanding the superconductive shielding, the white flux noise of the system was degraded by a factor of two after the connection of the pickup coils, and amounted to $\sqrt{S_\Phi}$ = 10 $\mu\Phi_0/\sqrt{\text{Hz}}$. In spite of all precautions, this degradation is probably caused by RFI, picked up by the unshielded twisted wires between the pickup coils and the input coils of the DROSs.

After removing the Pb shielding around the pickup coils, the white flux noise increased to more than 30 $\mu\Phi_0/\sqrt{\text{Hz}}$. In section 4.3.3, it will be demonstrated that this additional noise is probably due to Johnson noise in the radiation shields of the cryostat. This is confirmed by the observation that the flux noise decreased significantly when the pickup coils were lifted a few centimeters above the bottom of the cryostat.

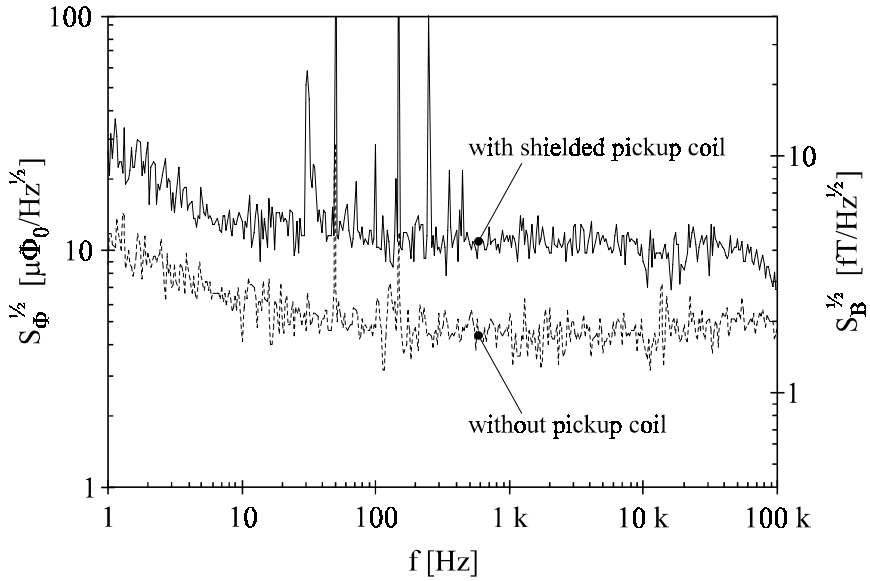

Figure 4.10 *Noise spectra of a DROS in the three-channel system before and after connecting the input coil to a shielded pickup coil. The left vertical axis gives the flux noise, whereas the right axis represents the magnetic field noise. The spike at ~30 Hz in the upper trace is due to a mechanical vibration.*

By measuring the response to the magnetic field of a small coil which was positioned at various distances below the gradiometric pickup coils and which carried an ac current, the field-to-flux transfer of the flux transformers was determined to be $\partial B/\partial\Phi_{sig} = 0.4$ nT/Φ_0 ($A_{eff} = 5.2$ mm^2). According to Eq. (4.7), this experimental field-to-flux transfer implies that $(L_{in} + L_{pu} + L_{par}) = 0.5$ µH. By substituting the design values of $L_{in} = 0.1$ µH and $L_{pu} = 0.35$ µH, a realistic inductance of $L_{par} \approx 50$ nH for the 15-cm-long twisted leads between the pickup coils and the DROSs is deduced.

The right vertical axis of Fig. 4.10 gives the noise in terms of the magnetic field sensitivity, using the experimentally determined value of $\partial B/\partial\Phi_{sig}$. As can be seen, the white magnetic field noise of the shielded gradiometer system is $\sqrt{S_B} = 4$ fT/$\sqrt{\text{Hz}}$ (10 fT/$\sqrt{\text{Hz}}$ @ 1 Hz), which corresponds to a gradiometer noise of 1 fT/cm/$\sqrt{\text{Hz}}$ (2.5 fT/cm/$\sqrt{\text{Hz}}$ @ 1 Hz).

As a direct consequence of the small spacing of less than 1 mm between the three pickup coils, we clearly observed a low frequency crosstalk when the gradiometer channels were operated simultaneously. If the feedback flux of one channel was changed by 1 Φ_0, the other two channels detected a flux change of $5{\cdot}10^{-3}$ Φ_0. This crosstalk of 5‰ could possibly degrade the sensitivity of the DROSs as the relaxation oscillations in one DROS induce a high frequency ripple on the signal flux of another DROS. Even with R_{in}-C_{in} shunts across the input coils of the DROSs, the amplitude of this ripple can be hundreds of µΦ_0.

Fortunately, we did not observe any degradation of the sensitivity when the channels were operated simultaneously. This could possibly be attributed to the fact that the spectral impurity of the relaxation frequencies of the DROSs spreads the crosstalk signals over such a large bandwidth that the additional noise completely drowns in the “normal” flux noise of the DROSs.

4.2.5 Summary

In this section, a three-channel DROS system with wire-wound first-order axial gradiometers was discussed. Typically, the bare DROSs had a white flux noise of 4.5 µΦ_0/$\sqrt{\text{Hz}}$ when operated in FLL. This corresponds to an energy sensitivity of $\varepsilon = S_\Phi/2L_{sq,sig} \approx 275\ h$. Owing to the large typical flux-to-voltage transfer of 0.5 to 1 mV/Φ_0, simple room temperature FLL electronics, based on direct readout of the output voltage of the DROSs, could be used without degrading the sensitivity. When the input coils of the DROSs were connected to the wire-wound pickup coils, the white flux noise rose to about 10 µΦ_0/$\sqrt{\text{Hz}}$, despite a superconducting Pb shield around the pickup coils. This increase may be due to RFI. Nevertheless, the magnetic field sensitivity of $\sqrt{S_B} = 4$ fT/$\sqrt{\text{Hz}}$ is amply sufficient for a variety of bio-magnetic measurements. The sensitivity of the system decreased when the superconducting shield around the pickup coils was removed, which is caused by the Johnson noise in the radiation shields of the cryostat.

The most important result, however, is that crosstalk at the relaxation frequency did not decrease the sensitivity of the DROSs, which proves the feasibility of multi-channel DROS magnetometer systems.

4.3 A planar first-order DROS gradiometer

Using the experience acquired with the development of the three-channel DROS gradiometer, DROSs with a new layout were designed. The main improvements with respect to the DROSs of the three-channel system were the gradiometric layout of the signal SQUID, which minimizes the response to homogeneous magnetic fields and thus relaxes the shielding requirements, and the implementation of a reference junction instead of a reference SQUID. In such a configuration, a single junction with an appropriate critical current replaces the reference SQUID. In this way, the number of wires from room temperature to the DROS is decreased by two, since the application of the reference flux is not required anymore. A possible disadvantage of a DROS with a reference junction could be that $I_{c,ref}$ can no longer be tuned for noise optimization. Fortunately, the experimental results in this section show that this does not lead to a serious reduction of the sensitivity.

4.3.1 Layout of the gradiometric DROSs

DROSs with a reference junction as well as with a reference SQUID were fabricated in order to be able to compare their respective performance. In the remainder of this chapter, the DROSs with a reference junction will be referred to as “RJ DROSs”, whereas the devices with a reference SQUID will be named “RS DROSs”. Figure 4.11 shows a micrograph and the equivalent scheme of a gradiometric RS DROS. The Nb/Al,AlO_x/Al/Nb Josephson junctions were defined by reactive ion etching in an SF_6 plasma, whereas all other structures - i.e. the 300 nm thick rf sputtered SiO_2 insulating layer, the Pd resistors and the Nb wiring - were patterned with the lift-off technique.

The signal SQUID consists of two washer-shaped inductors, arranged in a gradiometric “figure-8” configuration. As the washers are connected in series with the Josephson junctions, homogeneous magnetic fields do not induce large screening currents in the washers, which would be the case if both washers were connected in parallel to the junctions [21]. The size of the hole in both washers is 50 µm, which corresponds to a total inductance of ~160 pH. From the measured critical current modulation depth, the actual SQUID inductance appeared to be significantly larger: $L_{sq,sig}$ = 550 pH. The additional inductance is due to the inductance of the double 5-µm-wide and 375-µm-long slit in each washer, to the inductance of the connections between the washers and the Josephson junctions, and to the mutual inductance between the two washers. The 2 x 4 μm^2 Josephson junctions of the signal SQUID each have a critical current of 2 to 2.5 µA, implying that $\beta_{L,sig} \approx 1.2$. The estimated junction capacitance is 0.25 pF.

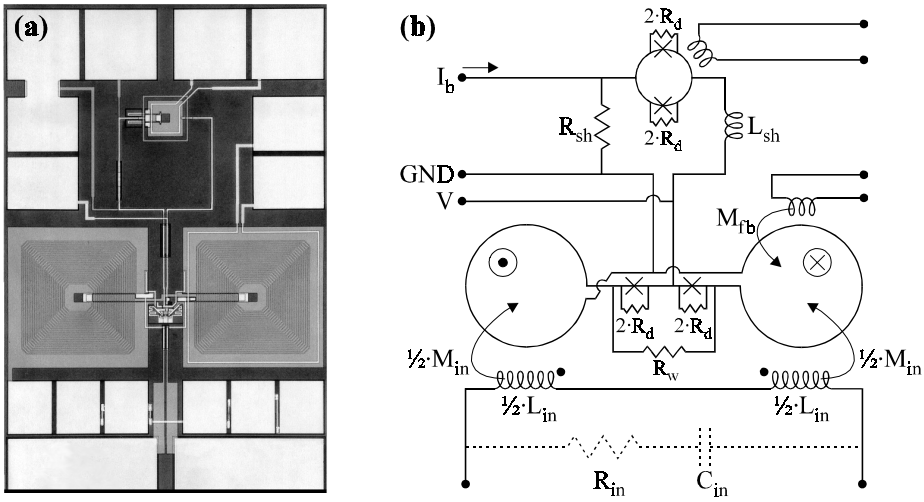

Figure 4.11 (a) *Micrograph and* **(b)** *scheme of a gradiometric DROS with a reference SQUID. The on-chip resistive input coil shunt can be connected with the six small bonding pads at the bottom of figure (a). The actual chip size, including the bonding pads, is 2 x 3.3 mm².*

The series-connected 25-turns input coils on top of the washers have a total inductance of $L_{in} \approx 150$ nH and their coupling with the signal SQUID was measured to be $M_{in} = 6.7$ nH, which implies a coupling coefficient of $k = 0.74$. The measured mutual inductance between $L_{sq,sig}$ and the single-turn feedback coil, on top of the right SQUID washer in Fig. 4.11, is $M_{fb} = 220$ pH.

To minimize the coupling to stray fields, the washer-type reference SQUID is enclosed by a superconducting shielding loop. The hole size of the reference SQUID is 50 µm, which, according to Eq. (2.19), corresponds to $L_{sq,ref} \approx 80$ pH. The resulting $\beta_{L,ref}$ of about 0.2 ensures a large modulation range for $I_{c,ref}$. A single-turn input coil on top of the reference SQUID is implemented to apply the reference flux. In the RJ devices, the reference SQUID is replaced by a single 2 x 6 µm² junction. The critical current of this junction, 3 to 3.5 µA, is in the middle of the modulation range of $I_{c,sig}(\Phi_{sig})$.

The square shunt inductor, which has a line width of 10 µm and a side length of 530 µm, has a designed inductance of $L_{sh} = 1.8$ nH [22]. The gradiometric layout of the signal SQUID minimizes the parasitic magnetic coupling between the shunt inductor and the signal SQUID. The shunt resistor R_{sh} has a resistance of 2 Ω, which yields an effective McCumber parameter of $\beta_C^* = 0.027$. According to Eq. (4.1), this value of β_C^* implies a theoretical maximum bias current of $I_{b,max} = 27$ µA. As the time constant L_{sh}/R_{sh} is about 1 ns, the relaxation frequency is of the order of 1 GHz. At $f_{RO} = 1$ GHz, Eq. (4.4b) gives a theoretical white flux noise of $\sqrt{S_{\Phi,theory}} = 2.9\ \mu\Phi_0/\sqrt{\text{Hz}}$.

Signal SQUID			**Reference SQUID**		
junction size	4 x 2	μm²	junction size	4 x 2	μm²
$2I_0$	4 .. 5	μA [b]	$2I_0$	4 .. 5	μA [b]
C_{sq}	0.5	pF [a]	$\beta_{L,ref}$	~0.2	[a]
hole size	2 x 50	μm			
$L_{sq,sig}$	~550	pH [b]	**Reference junction**		
$\beta_{L,sig}$	~1.2	[b]	junction size	6 x 2	μm²
R_w	6	Ω [a]	I_0	3 .. 3.5	μA [a]
Input coil			**Relaxation circuit**		
# turns	2 x 25		L_{sh}	1.8 [a] / 2.1 [b]	nH
line width	4	μm	R_{sh}	2	Ω [a,b]
L_{in}	150	nH [b]	β_C^*	0.027	[a]
M_{in}	6.7	nH [b]	R_d	20	Ω [a]
k	0.74		D	2.3	[a]

[a] Design / calculated value.
[b] Experimental value.

Table 4.2 *Main parameters of the gradiometric DROSs.*

To avoid L_{sh}-C_{sq} resonances, every single junction is shunted with a resistor of 40 Ω. Since these shunt resistors do not decrease the β_C parameter of the junctions below unity ($\beta_C \approx 3$), the junction hysteresis is not eliminated. The resulting R_d of 20 Ω implies a damping parameter of $D = 2.3$, which indicates sufficient damping of the L_{sh}-C_{sq} resonances. Like in the DROSs of the three-channel system, the signal SQUID inductance is shunted with a resistor $R_w = 6\ \Omega$ to damp L-C resonances between the SQUID inductance and the capacitances of the Josephson junctions.

Motivated by the positive effect of external R_{in}-C_{in} shunts across the input coils in the three-channel system, an optional on-chip resistive input coil shunt was implemented. By means of aluminium bonding wires, the resistance R_{in} of this shunt could be varied between 7.5 Ω and 60 Ω in steps of 7.5 Ω. The capacitor C_{in} was not integrated because of its large area and the associated high probability of shorts through the insulating SiO_2 layer.

Unlike the DROSs which have been discussed until now, the output voltage of the gradiometric DROSs was not measured across the reference SQUID or junction, but across the signal SQUID. As will be explained below, this leads to a slightly larger output voltage swing. The time-averaged voltage $\langle V \rangle$ across the reference SQUID or junction is either zero (if $I_{c,sig}(\Phi_{sig}) < I_{c,ref}$) or V_c (if $I_{c,sig}(\Phi_{sig}) > I_{c,ref}$). This is indicated schematically by the dashed V-Φ_{sig} curve in Fig. 4.12. The time-averaged voltage across the signal SQUID is either zero (if $I_{c,sig}(\Phi_{sig}) > I_{c,ref}$) or it *modulates* with Φ_{sig} (if $I_{c,sig}(\Phi_{sig}) < I_{c,ref}$), since $I_{c,sig}$ varies with Φ_{sig}. The resulting V-Φ_{sig} characteristic is sketched with a solid line in the lower graph of Fig. 4.12. The additional ROS-like modulation which is

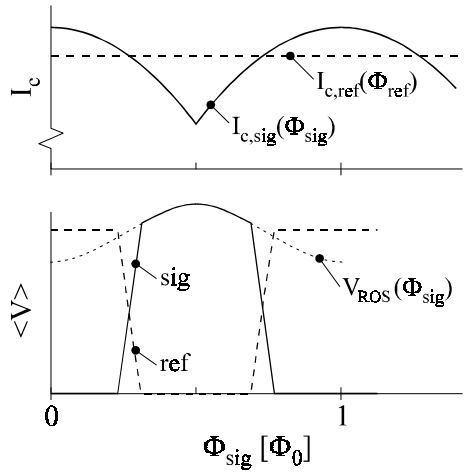

Figure 4.12 *Schematic I_c-Φ_{sig} curves (upper graph) and the corresponding V-Φ_{sig} characteristics (lower graph) of a DROS, if the output voltage is measured across the signal SQUID (solid line, marked "sig") respectively across the reference SQUID (dashed line, marked "ref"). The dotted line marked "$V_{ROS}(\Phi_{sig})$" indicates the V-Φ_{sig} characteristic of a ROS.*

superposed on the DROS V-Φ_{sig} characteristic increases the voltage modulation depth by a few microvolts.

The main parameters of the gradiometric DROSs are summarized in Table 4.2.

4.3.2 Experimental characteristics of the gradiometric DROSs

The DROSs were characterized using the setup of Fig. 4.5. In the preliminary experiments, the effect of external R_{in}-C_{in} shunts across the input coils was investigated. The value of C_{in} was fixed to 1 nF while R_{in} was varied. The best results were obtained for $R_{in} \leq 50\ \Omega$. In this case, both the flux-to-voltage transfer and the white flux noise improved by a factor of 2, compared to the situation without R_{in}-C_{in} shunt.

The on-chip input coil shunt resistors were not as effective as the external shunt circuits. Due to the lack of the dc blocking capacitor C_{in}, the low frequency Johnson noise generated by the integrated resistors directly flows through the input coil, generating a flux noise as high as $M_{in}\cdot\sqrt{(4k_BT/R_{in})} = 7\ \mu\Phi_0/\sqrt{\text{Hz}}$ for $R_{in} = 50\ \Omega$. Therefore, we used external SMD input coil shunts with $R_{in} = 50\ \Omega$ and $C_{in} = 1$ nF in all succeeding experiments, unless otherwise specified.

Figures 4.13a and 4.13b show V-Φ_{sig} characteristics of an RS DROS respectively of an RJ DROS. In both graphs, the signal flux was applied via the feedback coils, and the input coils were shunted with external R_{in}-C_{in} circuits.

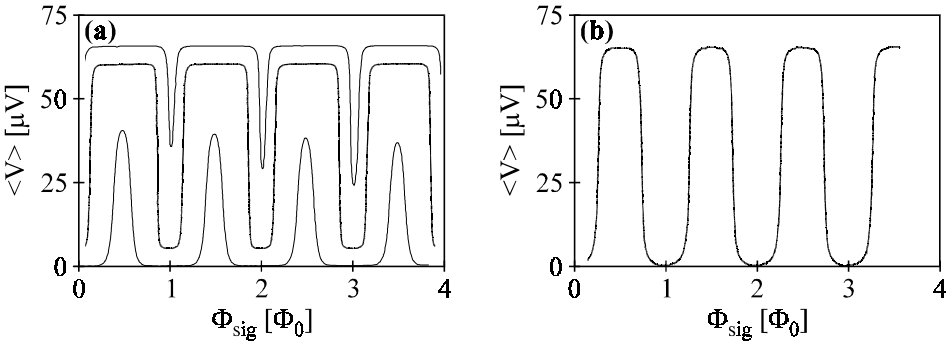

Figure 4.13 (a) *Experimental V-Φ_{sig} characteristics of a gradiometric RS DROS, plotted for three different values of the reference flux. For clarity, the three traces are shifted vertically.* **(b)** *Experimental V-Φ_{sig} characteristic of a gradiometric RJ DROS.*

For the RS device, the shape of the V-Φ_{sig} characteristics changes from the left to the right of the graph. This is due to the parasitic magnetic coupling between the non-gradiometric feedback coil and the reference SQUID. This coupling causes Φ_{ref}, and thus $I_{c,ref}$, to vary with Φ_{sig}. Apparently, the superconducting shielding loop around the reference SQUID is not adequate, which can lead to non-linear FLL characteristics for large values of Φ_{sig}. The RJ devices did not show this unintended effect, as the critical current of the reference junction is not affected by Φ_{sig}. This is another advantage of the RJ devices.

For both the RS DROSs and the RJ DROSs, the optimum bias current was around 50 μA, which is almost twice the theoretical expectation given by Eq. (4.1). At temperatures below 4.2 K, the optimum bias current decreased towards the theoretical value. This indicates that, at 4.2 K, thermal noise widens the operation range of the DROSs by increasing the minimum return voltage of the SQUIDs.

The typical modulation depth of the V-Φ_{sig} characteristics was 50 to 70 μV at $I_b \approx 50$ μA. The measured flux-to-voltage transfer functions ranged from 0.7 to 1 mV/Φ_0, and for some samples even higher values were measured. This is about twice the theoretical expectation of Eq. (4.3c). This could be due to the fact that Eq. (3.9) overestimates the thermal spread on the critical current of low-capacitance junctions with a small critical current [23,24].

Figure 4.14 shows the flux noise spectrum of an RS DROS, operated in FLL. The white flux noise level of 5 $\mu\Phi_0/\sqrt{\text{Hz}}$ corresponds to an energy sensitivity of $\varepsilon = S_\Phi/2L_{sq,sig} \approx 150\ h$. The 1/f noise corner frequency is about 15 Hz and at 1 Hz, $\sqrt{S_\Phi} \approx 15\ \mu\Phi_0/\sqrt{\text{Hz}}$. The right vertical axis of Fig. 4.14 indicates the equivalent current noise, referred to the input coils. The white current noise is $\sqrt{S_I} = 1.6$ pA/$\sqrt{\text{Hz}}$, increasing to ~5 pA/$\sqrt{\text{Hz}}$ at 1 Hz. The coupled energy sensitivity is $\varepsilon_{coupl} \approx 300\ h$. The contribution of the amplifier noise to the overall flux noise is also plotted in Fig. 4.14. This amplifier-related flux noise was

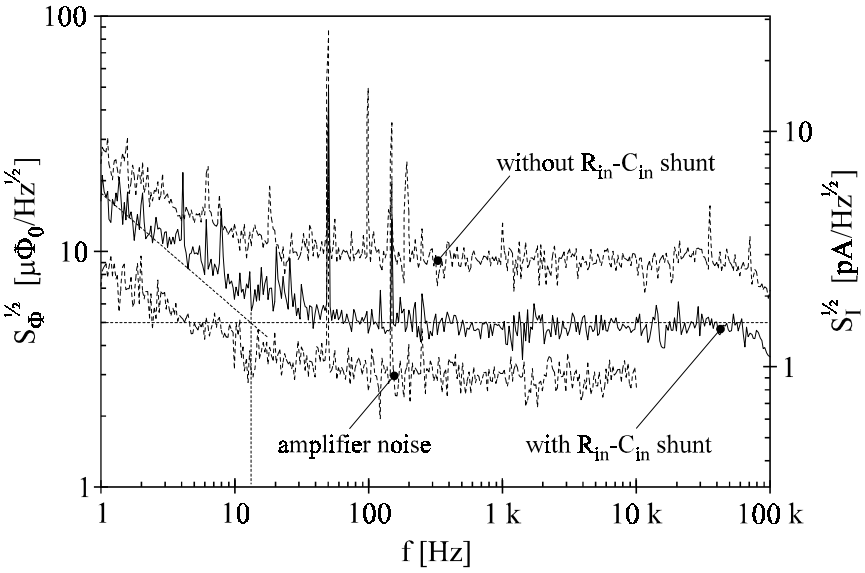

Figure 4.14 *Noise spectra of a gradiometric RS DROS. The left vertical axis represents the flux noise, the right vertical axis is in units of the equivalent current noise, referred to the input coils.*

calculated as $\sqrt{S_{\Phi,amp}} = e_n/(\partial V/\partial\Phi_{sig})$, with e_n the voltage noise of the amplifier and $\partial V/\partial\Phi_{sig}$ the flux-to-voltage transfer of the DROS at the working point. As a result of the large flux-to-voltage transfer of the DROS, the amplifier noise is not dominant. The upper trace of Fig. 4.14, giving the flux noise of the same DROS but now without the R_{in}-C_{in} shunt, clearly shows the benefit of the R_{in}-C_{in} shunt across the input coil.

The typical white flux noise of the RJ DROSs was 6 $\mu\Phi_0/\sqrt{Hz}$, which is marginally larger than that of the RS devices, 5 $\mu\Phi_0/\sqrt{Hz}$. The RJ devices were very easy to tune because their performance did not depend strongly on the settings of I_b and V_{offset}, which are the only adjustable parameters. The characteristics were identical after each cool-down.

For two RS DROSs, the value of R_d was changed in order to evaluate the effect of the damping resistors. This was done by cutting the Pd thin film resistors with a Ga^+ focused ion beam. The initial white flux noise of both DROSs was below 6 $\mu\Phi_0/\sqrt{Hz}$. For one sample, the damping resistors were removed partially to double their resistance. In this way, the damping parameter was reduced from $D = 2.3$ to $D = 0.6$. The result was an increase of the white flux noise to 8 $\mu\Phi_0/\sqrt{Hz}$. The damping resistors of the other sample were disconnected completely. This resulted in a flux noise as high as 14 $\mu\Phi_0/\sqrt{Hz}$, which is more than twice the initial value. These results clearly show the positive effect of the damping resistors on the sensitivity of the DROSs.

For an experimental determination of the value of L_{sh}, the relaxation frequency of a gradiometric ROS was measured. The layout of this ROS was identical to that of the DROSs, except of course for the lack of a reference SQUID or junction. Initially, we intended to measure the relaxation frequency as a function of the applied flux, using the setup and the procedure which was described in chapter 3. However, due to the low critical current of the junctions, the high frequency output power was below the detection limit of the setup. Therefore, gradiometric ROSs with a much larger critical current, $2I_0$ = 105 μA, were fabricated in a new production run. Figure 4.15a shows the output spectrum of such a ROS, oscillating at f_{RO} = 625 MHz. Besides the peak at the fundamental frequency, also the harmonics at ~1.3 GHz and at ~1.9 GHz are visible. Due to the large value of $\beta_{L,sig} \approx 30$, the relaxation frequency showed a very small modulation with Φ_{sig}. Therefore, L_{sh} was determined from f_{RO}-I_b measurements instead of f_{RO}-Φ_{sig} measurements.

The markers in Fig. 4.15b show the measured f_{RO}-I_b relation. The solid line is a fit, calculated via the method of section 3.3.4, using L_{sh} = 2.1 nH and T_V = 225 ps. The agreement between the fit value and the design value of L_{sh} is noticeable, especially if one considers that the experimental value of L_{sh} also comprises "parasitic" inductances, such as the SQUID inductance.

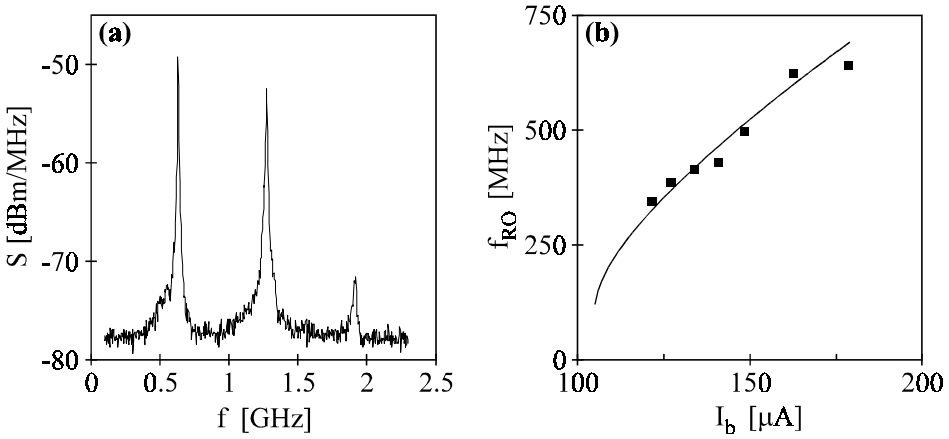

Figure 4.15 (a) *Spectrum of the high frequency output signal of a gradiometric ROS with $2I_0$ = 105 μA at a bias current of 163 μA. The frequency of the relaxation oscillations is 625 MHz. The vertical scale has not been corrected for the gain of the pre-amplifier, which is about 25 dB.* **(b)** *Experimental f_{RO} vs. I_b characteristic (markers) with theoretical fit (solid line). The fit value for L_{sh} is 2.1 nH.*

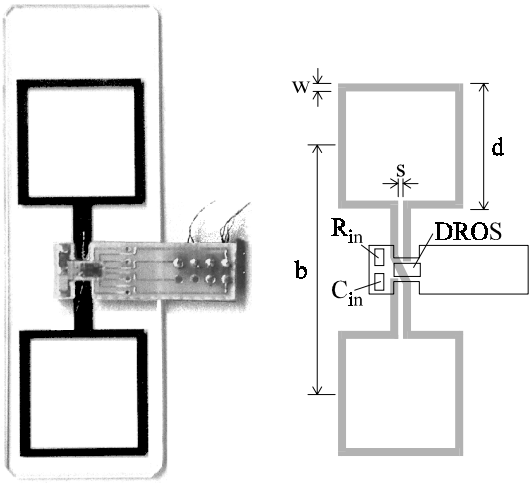

Figure 4.16 *Photograph of the assembled 2 x 2 cm² planar gradiometer.*

4.3.3 Gradiometric DROSs with external planar gradiometers

Using gradiometric RJ DROSs, two gradiometer systems with external planar pickup coils were realized. A photograph of one of the assembled gradiometers is shown in Fig. 4.16. The DROSs were glued to an epoxy printed circuit board (PCB) which also contained the SMD R_{in}-C_{in} input coil shunt. The PCB was fixed to the glass substrate of the pickup coils with TRZ 0004 epoxy [25]. The connections between the input coils and the pickup circuit were made with 50-µm-thick and 1-cm-long Nb bonding wires [19].

	2 x 2 cm²	**1 x 1 cm²**	
d	20	10	mm
w	1.2	0.56	mm
s	0.05	0.04	mm
b	40	40	mm
L_{pu}	100 [a)]	60 [a)]	nH
A_{pu}	352 [a)]	89 [a)]	mm²
$\partial B/\partial\Phi_{sig}$	0.23 [b)]	0.78 [b)]	nT/Φ_0
A_{eff}	9.0 [b)]	2.7 [b)]	mm²

[a)] Design / calculated value.
[b)] Experimental value.

Table 4.3 *Parameters of the planar gradiometric pickup coils that were connected to the gradiometric RJ DROSs.*

The planar first-order pickup coils consisted of a 500 nm thick dc magnetron sputtered Nb film on a glass substrate of 75 mm x 25 mm x 1 mm. Two gradiometers were constructed: one with d = 2 cm and one with d = 1 cm, with d as defined in Fig. 4.16. Both gradiometers had a baseline of b = 4 cm. The line width w of the pickup coils was calculated to maximize the effective area A_{eff} of the gradiometers. The parameters of the pickup coils are listed in Table 4.3.

The effective areas which are listed in Table 4.3 were determined by measuring the response of the gradiometers to the magnetic field of a long (~2 m) straight wire, carrying an alternating current. From the experimentally determined values of A_{eff}, the inductances in the flux transformer circuits could be calculated via Eq. (4.7). For the 2 x 2 cm² gradiometer, this resulted in $L_{in} + L_{par}$ = 162 nH, and the 1 x 1 cm² gradiometer yielded the almost identical value of $L_{in} + L_{par}$ = 164 nH. Estimating the parasitic inductance of the 1-cm-long Nb bonding wires to L_{par} = 10 .. 15 nH [26], these results imply an input coil inductance of $L_{in} \approx$ 150 nH, which value has been printed in Table 4.2.

The first noise measurements were carried out inside a superconducting Nb shielding. Figure 4.17 shows the noise characteristics of the gradiometer with 2 x 2 cm² pickup coils. The sensitivity of the DROS was not degraded by the

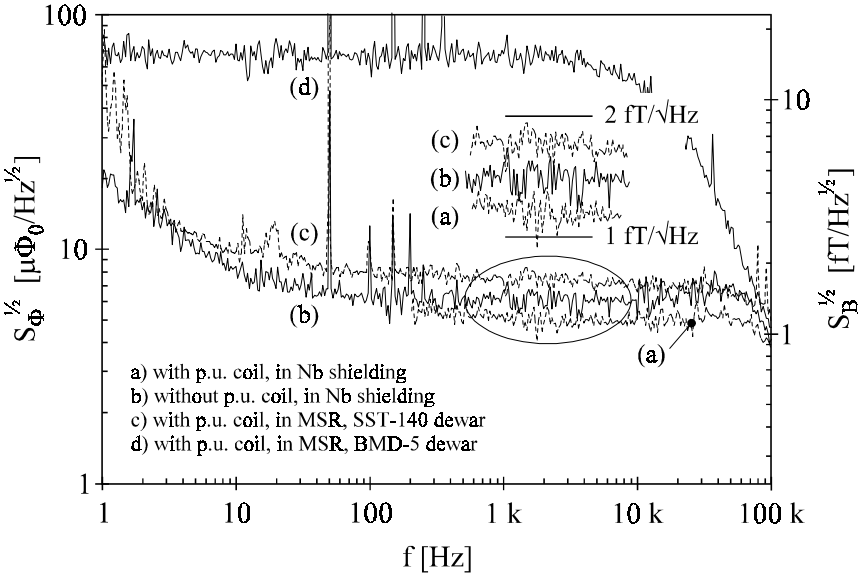

Figure 4.17 *Noise spectra of a gradiometric DROS with reference junction, coupled to an external 2 x 2 cm² planar gradiometer. The left vertical axis is in units of the flux noise, and the right vertical axis gives the equivalent magnetic field noise. The inset shows a part of the traces (a), (b) and (c) on an enlarged vertical scale.*

connection of the gradiometer, the white flux noise level even *decreased* from 6 $\mu\Phi_0/\sqrt{\text{Hz}}$ [trace (b)] to 5 $\mu\Phi_0/\sqrt{\text{Hz}}$ [trace (a)]. This is due to screening of $L_{sq,sig}$ by the superconducting flux transformer. The low frequency part of trace (a) is not shown since it was quite irregular due to mechanical vibrations and microphonics. The white flux noise of 5 $\mu\Phi_0/\sqrt{\text{Hz}}$ corresponds to a magnetic field resolution of $\sqrt{S_B}$ = 1.2 fT/$\sqrt{\text{Hz}}$ or, equivalently, a gradiometer noise of 0.3 fT/cm/$\sqrt{\text{Hz}}$.

After these preliminary measurements, the gradiometers were mounted in a non-magnetic fiberglass probe, and cooled down in the same BTI BMD-5 dewar which was used for the three-channel system. The noise spectrum of this configuration, measured in a magnetically shielded room [20], is plotted in trace (d) of Fig. 4.17. The noise increased drastically to $\sqrt{S_\Phi}$ = 65 $\mu\Phi_0/\sqrt{\text{Hz}}$ ($\sqrt{S_B}$ = 15 fT/$\sqrt{\text{Hz}}$). In this cryostat, the sensitivity of the three-channel system also degraded, and therefore the cryostat was suspected to be at the origin of the additional noise. To verify this hypothesis, we adapted the non-magnetic insert for use in a modern CTF SST-140 non-magnetic dewar. As trace (c) of Fig. 4.17 shows, the white flux noise in this "new" cryostat was significantly lower, 7 to 8 $\mu\Phi_0/\sqrt{\text{Hz}}$, corresponding to a magnetic field noise better than 2 fT/$\sqrt{\text{Hz}}$. This clearly indicates that the BMD-5 cryostat was the source of the excess noise.

At lower frequencies, trace (c) in Fig. 4.17 is somewhat irregular, which is probably due to residual noise in the MSR and to mechanical vibrations. Nevertheless, the magnetic field resolution at 1 Hz is still ~10 fT/$\sqrt{\text{Hz}}$. To demonstrate the operation of the system, some simple bio-magnetic measurements were carried out. An example of such a measurement is the magnetic heart signal which was shown in Fig. 1.1.

The gradiometer with 1 x 1 cm^2 pickup coils has also been characterized. As a direct result of its smaller effective area (A_{eff} = 2.7 mm^2 instead of 9 mm^2), the white magnetic field noise was larger than for the gradiometer with the 2 x 2 cm^2 pickup coils. Nevertheless, its white magnetic field resolution of about 4.5 fT/$\sqrt{\text{Hz}}$ is sufficient for bio-magnetic measurements.

4.3.4 Summary

In this section, the development of planar first-order gradiometers based on DROSs was described. To minimize the direct pickup of magnetic fields, the DROSs had a gradiometric signal SQUID. The white flux noise of the bare DROSs was about 5 $\mu\Phi_0/\sqrt{\text{Hz}}$ when operated in FLL, corresponding to an energy sensitivity of $\varepsilon \approx 150\ h$. Owing to the large flux-to-voltage transfer of the devices, 0.7 to 1 mV/Φ_0 typically, the amplifier noise did not dominate the overall flux noise. The coupled energy sensitivity of the devices was $\varepsilon_{coupl} \approx 300\ h$.

Besides DROSs with a reference SQUID, also DROSs with a reference junction were developed and characterized. The flux noise level of these devices, ~6 $\mu\Phi_0/\sqrt{\text{Hz}}$, was only slightly larger than that of the devices with a

reference SQUID. The devices with a reference junction were very user-friendly and easy to tune, and required two wires less for operation.

The characteristics of the DROSs did not degrade when the input coils were connected to external flux transformers. Coupled to an external planar gradiometric pickup coil with a coil size of 2 x 2 cm^2 and a baseline of 4 cm, the white magnetic field noise inside a superconducting shielding was only 1.2 fT/√Hz (7 fT/√Hz @ 1 Hz). Inside a magnetically shielded room, without additional shields around the gradiometer, the white field noise was still below 2 fT/√Hz (~10 fT/√Hz @ 1 Hz). This magnetic field resolution matches that of other state-of-the-art SQUID systems.

4.4 A directly coupled multi-loop DROS magnetometer

In sections 4.2 and 4.3, external pickup circuits were connected to the DROSs to increase the effective sensing area and thus the response to magnetic fields. Although such configurations work fine, they give rise to complications in multi-channel SQUID systems, for example because of the limited reliability of the superconducting contacts between the pickup coils and the input coils. Moreover, a system composed of many separate components is not well suited for mass production. A possible solution to overcome these limitations is the integration of the entire flux transformer on the same substrate as the DROS, as was demonstrated by Lee *et al.* [27]. Another configuration, the directly coupled multi-loop DROS magnetometer, is discussed in this section.

In a directly coupled SQUID, the magnetic field is sensed directly by the SQUID inductance, without intermediate flux transformer. Therefore, the geometry of the SQUID should combine two seemingly contradictory properties: a *large effective area* for optimum field-to-flux transfer and a *small inductance* in order to keep the β_L parameter reasonably small. By connecting several large loops in parallel, these two requirements can be combined. Multi-loop dc SQUIDs with APF circuits have been applied in several multi-channel bio-magnetometer systems [28,29], and in this section it will be shown that the multi-loop structure is also applicable for DROSs.

4.4.1 Layout of the multi-loop DROS magnetometer

A photograph and the scheme of the multi-loop DROS are printed in Fig. 4.18. The eight loops, arranged like the parts in a round pie, are connected in parallel in the central area of the device. The entire structure has a diameter of 8 mm. According to the theory of Drung *et al.* [22], the inductance of the multi-loop signal SQUID amounts to $L_{sq,sig}$ = 410 pH and its theoretical effective area is A_{eff} = 4.9 mm^2.

The damping resistors, the washer-type reference SQUID and the Josephson junctions of the signal SQUID are located in the center of the device. Two superconducting shielding loops prevent direct pickup of the magnetic field by the reference SQUID. The 4 x 4 µm^2 Nb/Al,AlO_x/Al/Nb Josephson

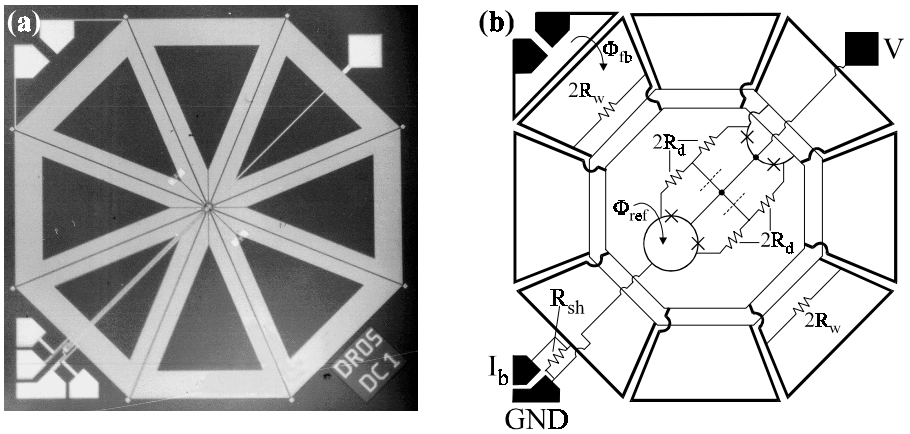

Figure 4.18 (a) *Micrograph and* **(b)** *scheme of the directly coupled multi-loop DROS magnetometer. The diameter of the entire structure is 8 mm. The dashed lines indicate the positions were the central connections of the damping resistors were cut with a Ga^+ focused ion beam. For clarity, the coil for applying the reference flux and the associated bonding pads are not indicated in figure (b).*

junctions have a critical current of 7 μA each, and their presumed capacitance is C_j = 0.5 pF. The β_L parameter of the signal SQUID is $\beta_{L,sig} \approx 2.8$.

The shunt resistor R_{sh} has a value of 2 Ω and is positioned at the lower left corner of Fig. 4.18. According to Eq. (4.1), the resulting value of $\beta_C^* = 0.17$ implies a theoretical maximum bias current of 34 μA. By connecting the bias current in the middle of one pickup loop, at the lower left of Fig. 4.18, an inductance of $\sim\frac{1}{4}\cdot L_{loop} \approx 0.8$ nH is introduced in the relaxation circuit. Therefore, no additional discrete shunt inductor L_{sh} is required. The time constant of the relaxation circuit, $L_{sh}/R_{sh} \approx 0.5$ ns, suggests a relaxation frequency of a few GHz.

Each junction is shunted by a resistor $2R_d$ = 20 Ω to damp the L_{sh}-C_{sq} resonances. The damping parameter of $D \approx 2$ indicates sufficient damping. In order to prevent L_{sq}-C_j resonances in the signal SQUID, the SQUID inductance is shunted at two sites with additional damping resistors of $2R_w$ = 20 Ω.

The feedback flux is applied by means of the small feedback coil in the upper left corner of the photograph. The main parameters of the multi-loop DROS are summarized in Table 4.4.

4.4.2 Experimental characteristics of the multi-loop DROS

The devices showed optimum performance at bias currents around 30 μA, which is in good agreement with the theoretical maximum bias current of 34 μA. Trace (a) in Fig. 4.19 shows a V-Φ_{sig} characteristic of a multi-loop DROS, measured in a superconducting Nb/Pb shielding. The typical voltage

Multi-loop signal SQUID			**Washer-type reference SQUID**		
diameter	8	mm	junction size	4 x 4	μm²
junction size	4 x 4	μm²	$2I_0$	16	μA [b]
$2I_0$	14	μA [b]	hole size	20	μm
C_{sq}	1	pF [a]	$L_{sq,ref}$	35	pH [b]
$L_{sq,sig}$	410	pH [a]	$\beta_{L,ref}$	~0.25	[b]
$\beta_{L,sig}$	2.8	[a]			
A_{eff}	4.9 [a] / 4.1 [b]	mm²	**Relaxation circuit**		
R_w	10	Ω [a]	L_{sh}	~0.8	nH [a]
			R_{sh}	2	Ω [b]
			β_{C^*}	0.17	[a]
			R_d	10	Ω [a]
			D	2	[a]

[a] Design / calculated value.
[b] Experimental value.

Table 4.4 *Main parameters of the multi-loop directly coupled DROS magnetometers.*

modulation depth of the devices was between 40 and 50 μV, which is in accordance with the theoretical expectation of Eq. (4.2). However, the experimental flux-to-voltage transfer of about 180 μV/Φ_0 is below the theoretical expectation of ~300 μV/Φ_0 almost by a factor of two.

When the temperature of the helium bath was decreased to about 2 K, the slopes of the V-Φ_{sig} characteristic became steeper, as shown in trace (b) of Fig. 4.19. This indicates that the reduction of the flux-to-voltage transfer is not due to external sources, e.g. RFI, but that it is caused by thermal effects in the DROS itself. The asymmetry in the V-Φ_{sig} curves at 2 K may be caused by a small "APF-effect" due to parasitic magnetic coupling between the different elements of the DROS.

To investigate whether the Johnson noise generated by the resistors $2R_w$ could be at the origin of the small value of $\partial V/\partial\Phi_{sig}$, we cut these two resistors with a Ga^+ focused ion beam (FIB). However, this had no effect on the slope of the V-Φ_{sig} curves. In a second attempt to find the cause of the reduced flux-to-voltage transfer, we changed the configuration of the damping resistors $2R_d$. The central connections were cut with the FIB at the positions indicated with dashed lines in Fig. 4.18b. As trace (c) in Fig. 4.19 shows, $\partial V/\partial\Phi_{sig}$ increased by about 50% as a result of this action. This clearly shows that the damping resistors $2R_d$ affect the flux-to-voltage transfer of the multi-loop DROS magnetometer.

A simple way to evaluate the effect of the Johnson noise generated by the damping resistors is to assume that it increases the spread on the critical currents of the reference SQUID and the signal SQUID. According to Eq. (3.9), at T = 4.2 K, the thermally induced critical current spread of both dc SQUIDs

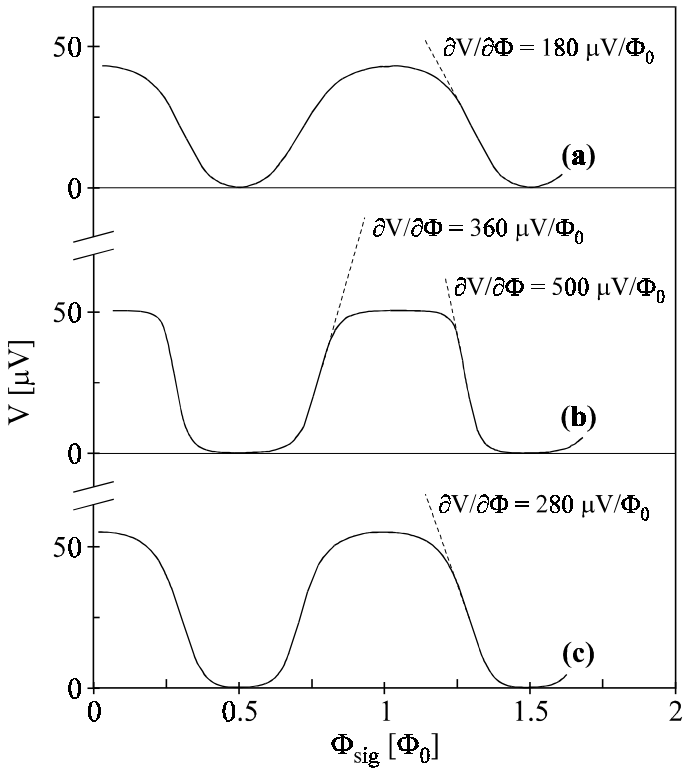

Figure 4.19 *V-Φ_{sig} characteristics of a multi-loop DROS recorded at a bias current of 30 μA in three different cases:* **(a)** *original configuration, T = 4.2 K;* **(b)** *original configuration, T ≈ 2 K;* **(c)** *central connection of the damping resistors removed with a Ga^+ focused ion beam, T = 4.2 K.*

amounts to $\Delta I_{c,thermal} = 0.60\ \mu A$. In the original configuration, each junction is shunted by a resistor of $2R_d = 20\ \Omega$, generating a Johnson noise of $\sqrt{S_I} = 3.4\ pA/\sqrt{Hz}$. The effective bandwidth of this Johnson noise can be approximated with the plasma frequency of the junctions, $f_p = 33\ GHz$. This leads to a root mean square (rms) value of $\Delta I_{c,Johnson} = 0.62\ \mu A$ for the critical current spread caused by the Johnson noise. Because the Johnson noise and the thermal critical current noise are not correlated, they should be added quadratically, resulting in $\Delta I_{c,total} = \sqrt{(0.62^2 + 0.60^2)} = 0.86\ \mu A$. With this value for the total spread on the critical currents of the SQUIDs, Eqs. (4.3b) and (4.3a) yield $\partial V/\partial\Phi_{sig} \approx 210\ \mu V/\Phi_0$ if $V_c = 45\ \mu V$ is substituted. This is in reasonable agreement with the experimentally observed flux-to-voltage transfer of $180\ \mu V/\Phi_0$.

In the multi-loop DROSs which were modified with the FIB, the value of the resistors was doubled to 40 Ω. The associated Johnson noise is now 2.4 pA/√Hz, causing an additional critical current noise of $\Delta I_{c,Johnson}$ = 0.44 μA. Then, the total critical current noise is $\Delta I_{c,total}$ = 0.74 μA per SQUID. Via Eqs. (4.3b) and (4.3a), this leads to $\partial V/\partial\Phi_{sig} \approx 250\ \mu V/\Phi_0$. Again, this is close to the experimentally observed value of 280 μV/Φ₀. Thus, this simple model gives realistic values for the flux-to-voltage transfer, both before and after changing the layout of the damping resistors with the FIB.

The effective area of the multi-loop DROSs was measured inside a magnetically shielded room [20] by positioning an ac magnetic dipole at various distances below the magnetometers. The result, A_{eff} = 4.1 mm² (i.e. $\partial B/\partial\Phi_{sig}$ = 0.5 nT/Φ₀), is below the theoretical value of 4.9 mm² which was obtained with the theory of Drung *et al*. The origin of this discrepancy is not clear. The experimentally determined value of the effective area could be verified by means of a setup with a Helmholtz coil instead of a magnetic dipole. However, this double-check has not been performed.

Due to the relatively low flux-to-voltage transfer of the multi-loop DROS magnetometers, their sensitivity was limited by the input voltage noise of the room temperature electronics, 3.3 nV/√Hz in the white region. This is considerably above the amplifier noise (1.8 nV/√Hz) because of the Johnson noise generated in the room temperature RFI-filters, which had a resistance of 450 Ω. The best white noise in FLL, $\sqrt{S_\Phi}$ = 14 μΦ₀/√Hz ($\sqrt{S_B}$ = 7 fT/√Hz), was obtained for the "FIB-DROSs", which had the highest flux-to-voltage transfer. The intrinsic noise was in the range $\sqrt{S_{\Phi,intr}}$ = 6 .. 8 μΦ₀/√Hz ($\sqrt{S_{B,intr}}$ = 3 .. 4 fT/√Hz), but the exact value was difficult to determine because of the large contribution of the amplifier noise to the total flux noise.

4.4.3 Summary

In this section, an eight-loop directly coupled DROS magnetometer was discussed. The large effective area of this device makes a separate flux transformer superfluous, which is a large advantage in multi-channel magnetometer systems. However, due to the Johnson noise generated by the damping resistors, the flux-to-voltage transfer of the devices was limited to $\partial V/\partial\Phi_{sig}$ = 180 μV/Φ₀. With a focused ion beam, the connections of the damping resistors were rearranged, resulting in a larger transfer coefficient of about 280 μV/Φ₀. A simple model, giving a quantitative explanation of these results, was presented. The - amplifier limited - magnetic field sensitivity of the directly coupled DROSs with the modified layout was $\sqrt{S_B}$ = 7 fT/√Hz in the white region. A thorough experimental and theoretical study of the effect of the Johnson noise generated in the damping resistors could lead to a further improvement of the DROS characteristics.

4.5 A DROS-based current gauge

Until now, only DROS-based systems for magnetometry have been discussed. Nevertheless, all physical quantities that can be converted to a magnetic flux - e.g. mechanical displacements or electric currents - can be measured with SQUIDs, which widens the field of applications considerably. In this section, a DROS is used as a very sensitive current gauge, which is demonstrated by measuring the subgap *I-V* characteristic of a voltage biased high quality Nb/Al,AlO_x/Al/Nb superconducting tunnel junction (STJ).

This type of measurement is for instance of relevance for the readout of X-ray spectrometers based on STJs [30]. The principle of operation of such spectrometers is based on the fact that the subgap current of a voltage biased tunnel junction rises momentarily when an X-ray photon is absorbed. The magnitude of this current rise, typically a few μA, is a measure for the energy of the incident photon. Since the signal only lasts for some microseconds, the current gauge which measures the subgap current should have a bandwidth of more than 1 MHz. For sufficient current resolution, its noise should not exceed a few pA/√Hz [31]. A last requirement for the current gauge is a low impedance for optimum voltage biasing of the STJ.

A standard non-hysteretic dc SQUID with an integrated superconducting input coil has the required current sensitivity. However, due to the flux modulated readout scheme, it is difficult - although not impossible [32,33] - to obtain the required FLL bandwidth of several MHz. Second generation SQUIDs like the dc SQUID array, the APF SQUID or the DROS have a non-modulated readout scheme, enabling high bandwidth operation with a relatively simple system layout [16,34].

Figure 4.20 shows the scheme of the setup that was used for the *I-V* measurements with a DROS. A gradiometric DROS with a reference junction, of the type which has been discussed in detail in section 4.3, was used to measure the current I_{stj} through the STJ, which was mounted on the same epoxy printed circuit board as the DROS. The room temperature flux locked loop electronics, identical to that of Fig. 4.5, is not indicated in Fig. 4.20. The STJ was voltage biased with a small SMD resistor R_x, located in the vicinity of the junction. We used two values for this resistor, 1.5 Ω and 3.7 Ω. Since R_x is much smaller than the dynamic resistance of the STJ, the junction is biased at a voltage $V = I_{b,x} \cdot R_x$. The bias voltage V_{stj} was measured with a room temperature differential amplifier, not indicated in Fig. 4.20. The DROS and the STJ were shielded from environmental electromagnetic noise with a Nb shield. All wires from room temperature to the cryogenic environment were RFI filtered, and in the lines which were connected to the input coil of the DROS, cooled series resistors of a few kΩ were mounted for additional filtering.

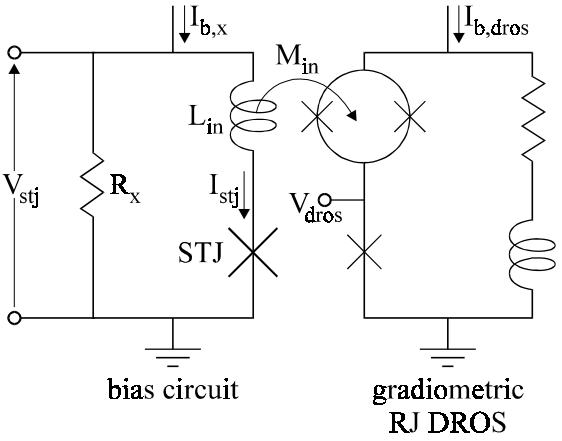

Figure 4.20 *Scheme of the setup which was used to measure the current versus voltage characteristic of a voltage biased superconducting tunnel junction (STJ) with a DROS.*

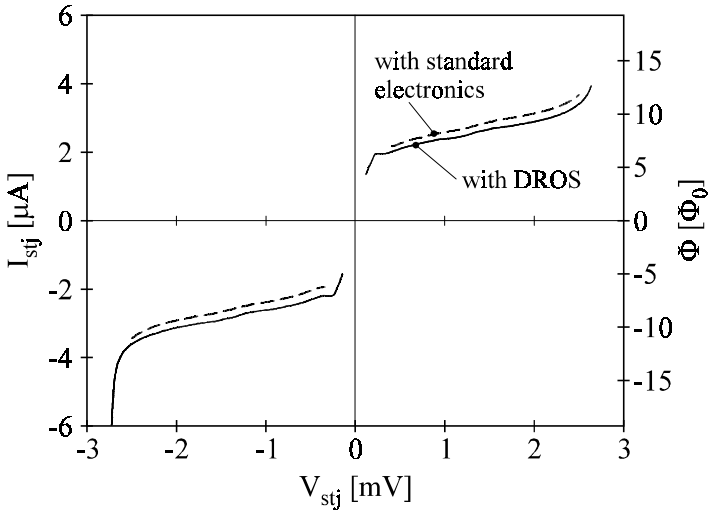

Figure 4.21 *Measured subgap I-V characteristics of a voltage biased STJ with a large excess current in the subgap. Solid line: measured with the DROS-based setup of Fig. 4.20. Dotted line: measured with standard I-V electronics. For clarity, the dotted line is shifted vertically by about 0.25 μA. The right vertical axis is in units of the flux coupled to the DROS.*

During the initial tests of the system, a low quality STJ with a large excess current in the subgap was used. The measured *I-V* characteristic of this STJ is plotted in Fig. 4.21. For comparison, the *I-V* characteristic which was measured with conventional *I-V* electronics is also plotted in the graph. The correspondence between the two traces is good, which demonstrates that the setup operates properly.

The STJ could be biased with high stability at voltages down to its minimum return voltage [Eq. (2.8b)] of a few hundred microvolts. At lower voltages, the bias circuit starts to act as a relaxation oscillator. The frequency of the relaxation oscillations in the bias circuit is determined by the time constant L_{in}/R_x, with L_{in} the inductance of the input coil of the DROS. In the present setup, this time constant is about 100 ns, which implies a relaxation frequency of approximately 10 MHz.

Experimentally, this relaxation oscillation effect was observed in two ways. First, at a bias voltage between 100 and 200 μV, the $I_{b,x}$-V_{stj} characteristic showed a discontinuity, marking the transition from the oscillating mode to the stable mode. Second, at bias voltages below ~150 μV, the *V*-Φ modulation of the DROS disappeared completely, because the relaxation oscillations generated in the bias circuit swept the input flux of the DROS over more than 100 Φ_0 at a frequency of about 10 MHz, wiping out the *V*-Φ modulation completely.

After the preliminary tests, the “bad” STJ was replaced by a high quality 10 x 10 μm² STJ. At 4.2 K, the critical current of this STJ was measured to be I_0 = 37 μA, and its quality parameter was V_m = 70 mV. Here, V_m is defined as $V_m = \pi/4 \cdot V_g/R_N \cdot 2\ \text{mV}/I_{2\text{mV}}$, with V_g = 2.8 mV the gap voltage, R_N = 42 Ω the normal resistance at $V \gg V_g$ and $I_{2\text{mV}}$ = 1.5 μA the subgap current at V = 2 mV.

In Fig. 4.22, measured current versus voltage characteristics of this STJ are plotted for different temperatures of the ^{4}He bath. Because a SQUID operated in FLL only measures flux changes and not absolute values, the vertical offsets in Fig. 4.22 are arbitrary, and different for each trace. As the STJ is voltage biased, also parts of the *I-V* trace with a negative dynamic resistance can be measured. Another advantage of the voltage biasing circuit is the elimination of the need for an external magnetic field to suppress the critical current of the STJ. Therefore, the subgap structure is not obscured by Fiske steps [35].

The peak at V = 260 μV in the 4.2 K trace is caused by the difference between the gap energy in the bottom and the top electrode of the STJ. The sensitivity of the DROS is demonstrated in the inset of Fig. 4.22, which shows an enlargement of a part of the 1.6 K trace. Small structures of less than 1 nA are revealed clearly, and the sharp rise of the subgap current at half the gap voltage is evident [36]. The measurements of Fig. 4.22 were reproduced in several subsequent cool-downs.

The bandwidth of the present flux locked loop setup is about 250 kHz. After upgrading the readout electronics to a higher bandwidth, the system will be applicable in the field of X-ray spectroscopy. DROSs are also good candidates for the readout of other types of cryogenic sensors, for instance micro-bolometers with a transition-edge sensor [37].

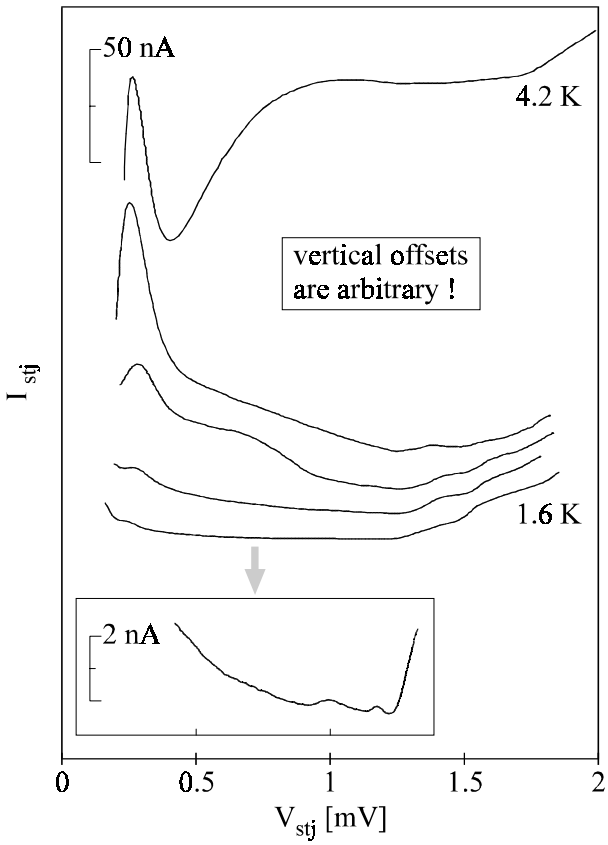

Figure 4.22 *Subgap I-V characteristics of a high quality STJ, measured at temperatures between 1.6 K and 4.2 K with the DROS-based setup of Fig. 4.20. The inset shows a part of the 1.6 K trace on a different current scale.*

4.6 Conclusions

In the first section of this chapter, the operation theory of the DROS was discussed, and in the subsequent sections various DROS-based measurement systems were presented. In section 4.2, a three-channel DROS gradiometer with wire-wound pickup coils of 2 cm diameter was discussed. This system had a white magnetic field sensitivity of $\sqrt{S_B}$ = 4 fT/√Hz (10 fT/√Hz @ 1 Hz). The noise level was not influenced by interference of the relaxation oscillations in adjacent channels, which unambiguously shows that DROSs can be used in multi-channel magnetometer systems.

In section 4.3, DROSs with a gradiometric signal SQUID were presented. Two versions of these gradiometric DROSs were fabricated: DROSs with a

reference SQUID (RS DROSs) and DROSs with a reference junction (RJ DROSs). The white flux noise of the RS DROSs ($\sqrt{S_\Phi}$ = 5 $\mu\Phi_0/\sqrt{\text{Hz}}$, $\varepsilon \approx 150\ h$) was slightly better than that of the RJ devices ($\sqrt{S_\Phi}$ = 6 $\mu\Phi_0/\sqrt{\text{Hz}}$, $\varepsilon \approx 200\ h$), but the RJ DROSs required less wires from the room temperature electronics to the cryogenic environment, and they were easier to operate. Moreover, the V-Φ_{sig} characteristics of the RJ DROSs were not distorted by parasitic coupling of the signal flux to the reference SQUID. With an external planar gradiometric pickup coil of 2 x 2 cm^2, a magnetic field sensitivity better than 2 fT/$\sqrt{\text{Hz}}$ was measured inside a magnetically shielded room.

In section 4.4, a directly coupled multi-loop DROS magnetometer was discussed. Owing to the multi-loop structure, this DROS combined a large effective area of 4.1 mm^2 with a moderate SQUID inductance of 410 pH. However, due to the Johnson noise generated in the damping resistors, the flux-to-voltage transfer of these devices was limited to $\partial V/\partial\Phi_{sig}$ = 180 $\mu V/\Phi_0$. After reconfiguration of the layout of the damping resistors, using a focused ion beam, the flux-to-voltage transfer increased to 280 $\mu V/\Phi_0$. A simple model was presented to explain this increase quantitatively. As a direct result of the limited flux-to-voltage transfer coefficient, the sensitivity of the multi-loop DROS magnetometer, $\sqrt{S_B}$ = 7 fT/$\sqrt{\text{Hz}}$, was limited by the noise of the readout amplifier at room temperature.

Finally, in section 4.5, a gradiometric RJ DROS was used to measure the current through a voltage biased Nb/Al,AlO_x/Al/Nb tunnel junction. The good current sensitivity of 2 pA/$\sqrt{\text{Hz}}$ allowed variations below 1 nA to be observed clearly in the subgap I-V characteristics of the tunnel junction. These results demonstrate that DROSs are promising candidates for the readout of cryogenic sensors.

References

[1] D.J. Adelerhof, J. Kawai, G. Uehara and H. Kado, “High sensitivity double relaxation oscillation superconducting quantum interference devices”, *Appl. Phys. Lett.* **65**, 2606-2608 (1994).

[2] D.J. Adelerhof, J. Kawai, G. Uehara and H. Kado, “High sensitivity double relaxation oscillation superconducting quantum interference devices with large transfer from flux to voltage”, *Rev. Sci. Instrum.* **66**, 2631-2637 (1995).

[3] M.J. van Duuren, Y.H. Lee, D.J. Adelerhof, J. Kawai, H. Kado, J. Flokstra and H. Rogalla, “Multichannel SQUID magnetometry using double relaxation oscillation SQUIDs”, *IEEE Trans. Appl. Supercond.* **6**, 38-44 (1996).

[4] J. Vrba, “SQUID gradiometers in real environments”, in *SQUID Sensors: Fundamentals, Fabrication and Applications*, ed. H. Weinstock, NATO ASI Series **329**, Kluwer Academic Publishers, Dordrecht / Boston / London (1996).

[5] M.J. van Duuren, G.C.S. Brons, D.J. Adelerhof, J. Flokstra and H. Rogalla, “Double relaxation oscillation superconducting quantum interference devices with gradiometric layout”, *J. Appl. Phys.* **82**, 3598-3606 (1997).

[6] D.J. Adelerhof, H. Wichers, C. Brons, M. van Duuren, D. Veldhuis, J. Flokstra and H. Rogalla, "Direct coupled multi-loop DROS magnetometer with direct voltage readout", in proc. *International Superconductive Electronics Conference* (ISEC), Nagoya, Japan, 371-373 (1995).
[7] G.H. Chen, H.Y. Zhai and Q.S. Yang, "Flux to voltage transfer function and noise in double relaxation oscillation SQUIDs", *IEEE Trans. Appl. Supercond.* **7**, 3477-3480 (1997).
[8] D.J. Adelerhof, M.J. van Duuren, J. Flokstra and H. Rogalla, "High sensitivity magnetic flux sensors with direct voltage readout: Double relaxation oscillation SQUIDs", *IEEE Trans. Appl. Supercond.* **5**, 2160-2163 (1995).
[9] Superconducting Sensor Laboratory, 2-1200 Muzaigakuendai Inzai, Chiba 270-13, Japan.
[10] D.J. Adelerhof, J. Kawai, K. Tsukada, G. Uehara and H. Kado, "Magnetometers based on double relaxation oscillation superconducting quantum interference devices", *Appl. Phys. Lett.* **66**, 2274-2276 (1995).
[11] M.B. Ketchen, "Design considerations for dc SQUIDs fabricated in deep sub-micron technology", *IEEE Trans. Magn.* **27**, 2916-2919 (1991).
[12] K. Enpuku, K. Sueoka, K. Yoshida and F. Irie, "Effect of damping resistance on voltage versus flux relation of a dc SQUID with large inductance and critical current", *J. Appl. Phys.* **57**, 1691-1697 (1985).
[13] R.H. Koch, V. Foglietti, J.R. Rozen, K.G. Stawiasz, M.B. Ketchen, D.K. Lathrop, J.Z. Sun and W.J. Gallagher, "Effects of radio frequency radiation on the dc SQUID", *Appl. Phys. Lett.* **65**, 100-102 (1994).
[14] The LT 1028 op-amp is manufactured by the Linear Technology Corporation, Milpitas (CA), U.S.A.
[15] D. Drung, "Advanced SQUID read-out electronics", in *SQUID Sensors: Fundamentals, Fabrication and Applications*, ed. H. Weinstock, NATO ASI Series **329**, Kluwer Academic Publishers, Dordrecht / Boston / London (1996).
[16] D. Drung, T. Radic, H. Matz and H. Koch, "A 2-channel wideband SQUID system for high-frequency geophysical applications", *IEEE Trans. Appl. Supercond.* **7**, 3283-3286 (1997).
[17] K. Enpuku, R. Cantor and H. Koch, "Modeling the direct current superconducting quantum interference device coupled to the multiturn input coil. II.", *J. Appl. Phys.* **71**, 2338-2346 (1992).
[18] BTI type BMD 5.
[19] W. Jaszczuk, H.J.M. ter Brake, J. Flokstra, D. Veldhuis, R. Stammis and H. Rogalla, "Bonding of a niobium wire to a niobium thin film", *Meas. Sci. Technol.* **2**, 1121-1122 (1991).
[20] Vacuumschmelze type AK-3B.
[21] M.B. Ketchen, "Integrated thin-film dc SQUID sensors", *IEEE Trans. Magn.* **23**, 1650-1657 (1987).
[22] D. Drung, S. Knappe and H. Koch, "Theory for the multiloop dc superconducting quantum interference device magnetometer and experimental verification", *J. Appl. Phys.* **77**, 4088-4098 (1995).
[23] D.J. Adelerhof, *Second generation dc SQUID magnetometers: (Double) Relaxation Oscillation SQUIDs*, Ph.D. thesis University of Twente, Enschede (1993).
[24] D.J. Adelerhof, H. Nijstad, J. Flokstra and H. Rogalla, "(Double) relaxation oscillation SQUIDs with high flux-to-voltage transfer: Simulations and experiments", *J. Appl. Phys.* **76**, 3875-3886 (1994).
[25] TRZ 0004 epoxy is manufactured by Oxford Instruments, Old Station Way, Eynsham, Witney, Oxon OX8 1TL, U.K.
[26] F.W. Grover, *Inductance calculations, working formulas and tables*, Dover Publications Inc., New York (1962).

[27] Y.H. Lee, H.C. Kwon, J.M. Kim, Y.K. Park and J.C. Park, "An integrated planar gradiometer based on a double relaxation oscillation SQUID", *Supercond. Sci. Technol.* **9**, A34-A37 (1996).

[28] D. Drung, "The PTB 83-SQUID system for biomagnetic applications in a clinic", *IEEE Trans. Appl. Supercond.* **5**, 2112-2117 (1995).

[29] K. Kazami, Y. Takada, G. Uehara, N. Matsuda and H. Kado, "Evaluation of Drung-type magnetometers for multi-channel systems", *Supercond. Sci. Technol.* **7**, 249-252 (1994).

[30] N.E. Booth and D.J. Goldie, "Superconducting particle detectors", *Supercond. Sci. and Technol.* **9**, 493-516 (1996).

[31] M. Frank, C.A. Mears, S.E. Labov, F. Azgui, M.A. Lindeman, L.J. Hiller, H. Netel, A. Barfknecht, "High resolution X-ray detectors with high-speed SQUID readout of superconducting tunnel junctions", *Nucl. Instr. and Meth. in Phys. Res.* **A370**, 41-43 (1996).

[32] R.H. Koch, J.R. Rozen, P. Wöltgens, T. Picunko, W.J. Goss, D. Gambrel, D. Lathrop, R. Wiegert and D. Overway, "High performance superconducting quantum interference device feedback electronics", *Rev. Sci. Instrum.* **67**, 2968-2976 (1996).

[33] R.D. Penny, D.K. Lathrop, B.D. Thorson, B.R. Whitecotton, R.H. Koch and J.R. Rozen, "Wideband front end for high-frequency SQUID electronics", *IEEE Trans. Appl. Supercond.* **7**, 2323-2326 (1997).

[34] D. Drung, H. Matz and H. Koch, "A 5-MHz bandwidth SQUID magnetometer with additional positive feedback", *Rev. Sci. Instrum.* **66**, 3008-3015 (1995).

[35] J.G. Gijsbertsen, E.P. Houwman, B.B.G. Klopman, J. Flokstra, H. Rogalla, D. Quenter and S. Lemke, "Field dependence of the Josephson current and Fiske resonances in specially shaped Josephson junctions", *Physica C* **249**, 12-24 (1995).

[36] T.M. Klapwijk, G.E. Blonder and M. Tinkham, "Explanation of subharmonic energy gap structure in superconducting contacts", *Physica B* **109**&**110**, 1657-1664 (1982).

[37] K.D. Irwin, G.C. Hilton, D.A. Wollman and J.M. Martinis, "X-ray detection using a superconducting transition-edge sensor microcalorimeter with electrothermal feedback", *Appl. Phys. Lett.* **69**, 1945-1947 (1996).

Chapter 5

Smart Double Relaxation Oscillation SQUIDs

In multi-channel SQUID systems based on resistively shunted non-hysteretic dc SQUIDs, a large number of wires is required between the room temperature electronics and the SQUIDs. For instance, in a 128-channel system operated with the standard flux locked loop configuration of Fig. 2.11, more than 750 wires are needed. The heat leak associated with these wires boils off several liters of liquid helium per hour [1,2]. Furthermore, the large number of wires decreases the reliability and increases the complexity and the production costs of multi-channel dc SQUID systems.

To reduce the number of wires in multi-channel SQUID systems, several research groups have developed digital single-chip SQUIDs [3,4,5,6]. In such SQUIDs, the entire flux locked loop circuitry is integrated on the same chip as the sensing SQUID. Using a time-division multiplexer for the readout of several single-chip SQUIDs, a further decrease of the number of wires can be achieved [7,8]. Additional advantages of the single-chip configuration are the reduction of crosstalk between different channels, the simpler room temperature electronics and the potential for a very large bandwidth, as the delay times of the leads between the room temperature electronics and the SQUID are no longer of importance.

At present, most single-chip digital SQUIDs are based on the concept which was developed originally at the Fujitsu laboratories in Japan [9]. Its principle will be discussed briefly in section 5.1. The on-chip flux locked loop circuitry of the Fujitsu single-chip SQUID is based on a superconducting up-down counter. A modified version of such a counter can also be used in combination with a DROS. A major advantage of such a *"smart DROS"*, compared to the Fujitsu SQUID, is the absence of an external clock, since the relaxation oscillations in

the DROS generate an on-chip clock signal. This enables smooth operation at high clock frequencies, resulting in a better sensitivity and a larger bandwidth. In section 5.2, the smart DROS concept will be introduced.

As already said, the key element of the on-chip feedback circuitry in a smart DROS is a superconducting up-down counter. In section 5.3, the principle of operation of this so-called *Josephson counter* will be discussed and in section 5.4, the dynamics of the smart DROS will be investigated theoretically by means of numerical simulations.

Based on these numerical simulations, a prototype of the Josephson counter was developed, which is described in section 5.5. Subsequently, using the experience acquired with the Josephson counter, a fully integrated smart DROS was designed and fabricated. In section 5.6, it will appear that the experimental characteristics of this smart DROS were in good agreement with the theoretical expectations, which demonstrates the viability of the smart DROS concept beyond any doubt.

Finally, in section 5.7, suggestions for further improvement of the smart DROS are given.

5.1 The Fujitsu single-chip SQUID

The subject of this section is the single-chip digital SQUID which was developed at the Fujitsu laboratories by Fujimaki *et al.* [1,3]. This is not the only single-chip SQUID concept reported in the literature. An example of a competing design is the digital SQUID which was originally suggested by

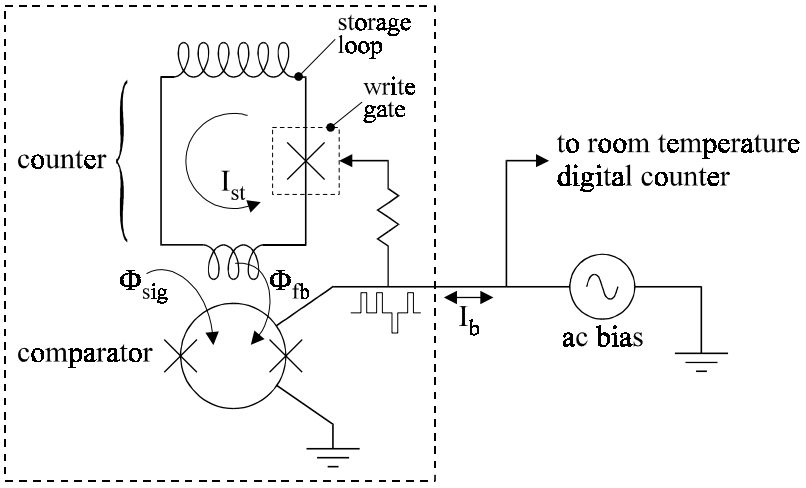

Figure 5.1 *Scheme of the single-chip SQUID that was developed at the Fujitsu laboratories. The elements inside the large dashed block are integrated on the chip.*

Likharev *et al.* [6,10,11]. Contrary to the Fujitsu single-chip SQUID, that is based on latching Josephson logic, the latter design is entirely based on rapid single flux quantum (RSFQ) logic, which makes the system potentially very fast, having a theoretical bandwidth in the GHz range and a slew rate of the order of $10^9\ \Phi_0$/s. However, the layout of these RSFQ SQUIDs is very complex, comprising for instance more than thousand Josephson junctions. The construction of a SQUID system is not really simplified when such complicated sensors are used. Conversely, the on-chip flux locked loop circuitry of the Fujitsu single-chip SQUID has a relatively simple architecture, which is, in addition, compatible with the use of a DROS.

5.1.1 Principle of operation

The basic scheme of the Fujitsu single-chip SQUID is shown in Fig. 5.1. The main elements are a *comparator* and an *up-down counter*. The comparator is a hysteretic dc SQUID with asymmetric current injection in the SQUID loop, which causes an asymmetric threshold characteristic, as sketched in Fig. 5.2a. The comparator is biased with a bipolar alternating clock current, having a frequency f_c and an amplitude as indicated in Fig. 5.2b.

If $\Phi_{sig} < 0$, the point (Φ_{sig},I_b) moves along the dashed line A-A' in Fig. 5.2a, and the comparator switches to the voltage state each time when point A" is crossed. Consequently, the comparator produces negative voltage pulses. If $\Phi_{sig} > 0$, the point (Φ_{sig},I_b) follows the line B-B', and the comparator generates a positive voltage pulse each time when point B" is crossed. Thus, the comparator discriminates between $\Phi_{sig} > 0$ and $\Phi_{sig} < 0$ by generating positive respectively negative voltage pulses with a frequency f_c. Because the junctions of the

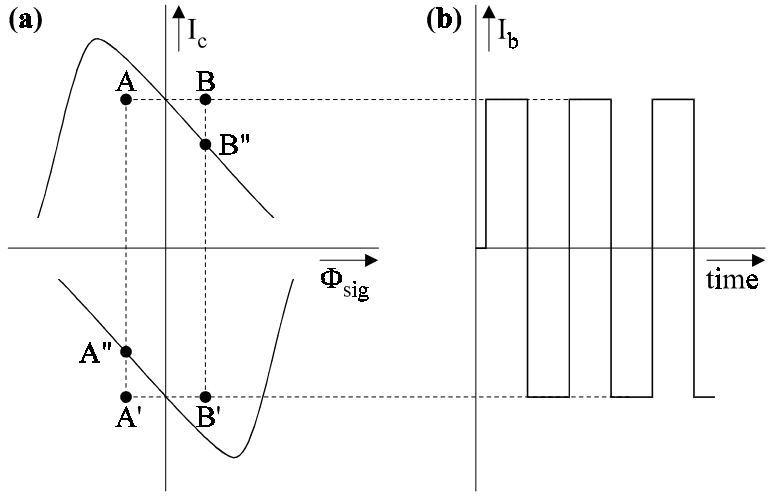

Figure 5.2 **(a)** *Threshold characteristic and* **(b)** *time-dependent bias current of the comparator in the Fujitsu single-chip SQUID.*

comparator are unshunted, the amplitude of these voltage pulses is of the order of the gap voltage of the Nb/AlO_x/Nb Josephson junctions (~2.8 mV).

The voltage pulses generated by the comparator constitute the input signal for the digital counter, which has the same function as the integrator in a conventional flux locked loop scheme. As a fully digital counter would lead to a very complex chip architecture, an alternative circuit was developed. In this scheme, the counter consists of a superconducting storage loop to which single flux quanta are added or removed by means of a *write gate*. When a positive voltage pulse is applied to the write gate, one flux quantum is added to the quantized flux in the storage loop. Likewise, a negative voltage pulse causes the number of stored flux quanta to be decreased by one. For each flux quantum which is added to or removed from the storage loop, the circulating current I_{st} in the counter changes by an amount of $\delta I_{st} = \Phi_0/L_{st}$, with L_{st} the inductance of the storage loop. The operation principle of the write gate will be discussed in more detail in section 5.3.

The current in the storage loop also flows through the feedback coil, which is magnetically coupled to the comparator via a mutual inductance M_{fb}. The quantization unit of the feedback flux, $\delta\Phi_{fb}$, is given by

$$\delta\Phi_{fb} = M_{fb} \cdot \delta I_{st} = \frac{M_{fb}}{L_{st}} \cdot \Phi_0 . \tag{5.1}$$

The net flux sensed by the comparator is $\Phi_{net} = \Phi_{sig} - \Phi_{fb}$. When the system is flux locked, $\Phi_{net} \approx 0$ and the comparator alternately generates positive and negative pulses. Consequently, the number of flux quanta in the storage loop oscillates between n and n+1. If the signal flux is changed in positive (negative) direction, the dynamic equilibrium of the system is disturbed, and the comparator generates only positive (negative) pulses. As a result, the current in the counter, and thus the feedback flux, increases (decreases) each clock period until the dynamic equilibrium is recovered. This is illustrated schematically in Fig. 5.3. The maximum slew rate of the system depends on the clock frequency f_c and on the quantization unit $\delta\Phi_{fb}$:

$$\left(\frac{\partial \Phi_{sig}}{\partial t} \right)_{max} = f_c \cdot \delta\Phi_{fb} . \tag{5.2}$$

A digital counter at room temperature, detecting the voltage pulses which are generated by the comparator, is used for the readout of the single-chip SQUID. Since the amplitude of the pulses is ~1 mV, simple amplification techniques can be used. If the system operates properly, the output of the room temperature counter is synchronized with the on-chip counter. However, like in any delta-modulated system, *bit errors* can cause a relative drift of the counters, which induces excess noise at low frequencies [5].

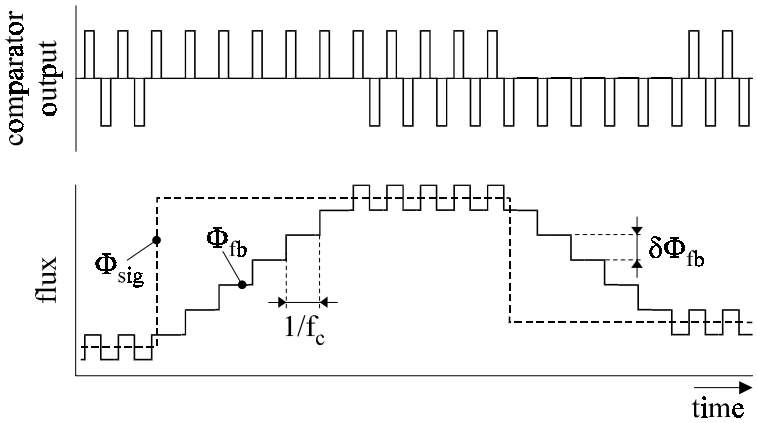

Figure 5.3 *Response of the Fujitsu single-chip SQUID to a time-dependent input flux.*

Based on the same arguments which hold for a ROS, it can be shown that the sensitivity of the digital single-chip SQUID improves at higher clock frequencies. For optimum sensitivity, f_c should be around 1 GHz [12]. Also the bandwidth and the slew rate of the system improve at higher clock frequencies. However, most single-chip SQUIDs presented in the literature operate at moderate frequencies of about 10 MHz, which prevents technical complications such as transmission line resonances or ground level fluctuations.

Fujimaki *et al.* demonstrated a single-chip SQUID with an integrated 500 nH input coil, operating at a clock frequency of 10 MHz [13]. The flux noise of this device was $\sqrt{S_\Phi} = 6.2\ \mu\Phi_0/\sqrt{\text{Hz}}$ ($\varepsilon \approx 3500\ h$; $\varepsilon_{coupl} \approx 4000\ h$) and the noise spectrum was white down to at least 0.2 Hz. This is attributed to the bipolar clock which acts like a bias current reversal scheme for conventional dc SQUIDs [14]. The maximum slew rate, 170 Φ_0/s, and the bandwidth of the on-chip flux locked loop, 1.1 kHz, were limited by the small quantization unit of $\delta\Phi_{fb} = 17\ \mu\Phi_0$.

An array of eight of these single-chip SQUIDs was operated with a Josephson time-division multiplexer [8]. The eight single-chip SQUIDs were operated at a clock frequency of $f_c = 5$ MHz, whereas the clock frequency for the multiplexer was 120 MHz. The system was operated successfully, although the flux noise of the system increased to 11.3 $\mu\Phi_0/\sqrt{\text{Hz}}$ when the multiplexer was active.

5.1.2 Variations on the Fujitsu single-chip SQUID

The dynamic range of the counter, i.e. the maximum number of flux quanta which can be stored, is limited by the maximum current which can flow through the write gate, $I_{g,max}$. In the single-chip SQUID discussed above, $I_{g,max} \approx 35\ \mu\text{A}$, corresponding to a dynamic range of $\pm I_{g,max} \cdot L_{st}/\Phi_0 = \pm 1.25 \cdot 10^5$.

Due to the small value of $\delta\Phi_{fb} = 17\ \mu\Phi_0$, the linear flux range of the Fujitsu single-chip SQUID was only $\pm 1.25 \cdot 10^5 \cdot 17\ \mu\Phi_0 = \pm 2.1\ \Phi_0$.

The dynamic range of the single-chip magnetometer can be increased by using the superconducting flux transformer as the counter inductance, instead of implementing a separate counter. In this configuration, the output pulses from the comparator control a write gate which writes flux quanta to and from the flux transformer circuit. In this way, the current in the flux transformer circuit is nulled continuously, and hence the dynamic range of the device is virtually infinite [4].

To improve the sensitivity of the single-chip SQUID, two-stage [15,16] or even three-stage [17] systems with a resistively shunted, non-hysteretic sensor SQUID in the first stage have been developed at HYPRES [18]. At clock frequencies above 1 MHz, the flux noise of the two-stage device, $20\ \mu\Phi_0/\sqrt{\text{Hz}}$, was limited by the sensitivity of the front-end analogue SQUID. No noise data has been published for the three-stage version.

5.2 The smart DROS

5.2.1 Principle of operation

The pulsed output of a DROS is particularly suited for digital readout. A possible digital readout scheme for a DROS, the *smart DROS* configuration, is illustrated in Fig. 5.4. The technical implementation of the bi-directional digital counter in this figure will be discussed in section 5.3.

Depending on the value of the signal flux, the relaxation oscillations in the DROS generate voltage pulses either across the reference SQUID or across the signal SQUID. The voltage pulses produced by the signal SQUID drive the “up”

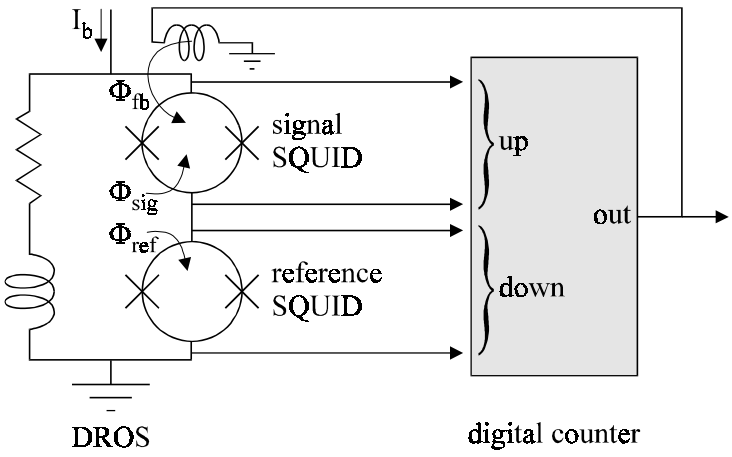

Figure 5.4 *Schematic representation of the smart DROS configuration.*

input of the counter, whereas the voltage pulses generated by the reference SQUID activate the "down" input. The output of the counter is fed back to the signal SQUID of the DROS, resulting in a net applied flux of $\Phi_{net} = \Phi_{sig}-\Phi_{fb}$. Each voltage pulse at the "up" ("down") input of the counter induces an increase (decrease) of the feedback flux by an amount $\delta\Phi_{fb}$.

When the system of Fig. 5.4 is operated, it automatically locks to the dynamic equilibrium where both hysteretic dc SQUIDs of the DROS have a switching probability of 50%. If the signal flux is changed, the system is forced out of this equilibrium, and consequently only one of the SQUIDs generates pulses while the other remains superconducting. As a result, the feedback flux increases or decreases - depending on the sign of the flux change - by one unit $\delta\Phi_{fb}$ per relaxation oscillation cycle, until a new dynamic equilibrium is reached. Thus, the output of the counter reconstructs the signal flux according to the same principle as used in the Fujitsu single-chip SQUID. A major difference with the Fujitsu SQUID is that the smart DROS does not require an external clock, since the relaxation oscillations constitute an internal clock.

5.2.2 Transfer function of the smart DROS

In the conventional readout scheme, a DROS is operated as a flux-to-voltage converter. Likewise, a DROS with digital readout converts the input flux to pulse rates. Therefore, the digital counterpart of the V-Φ_{sig} characteristic is the *pulse rate versus flux characteristic*, which is sketched in Fig. 5.5. In this graph, $\langle f_{sig} \rangle$ represents the time-averaged pulse rate of the signal SQUID, and $\langle f_{ref} \rangle$ is the average pulse rate of the reference SQUID. At values of Φ_{sig} where

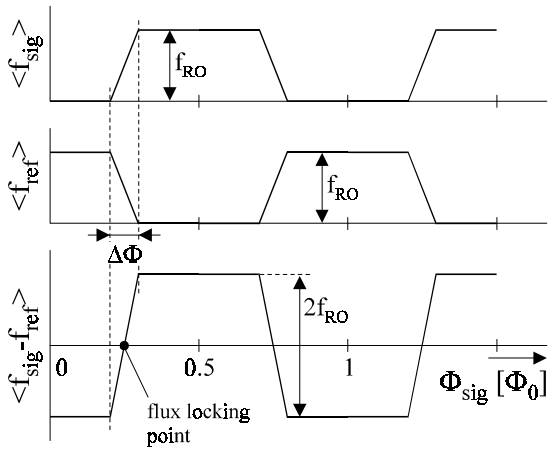

Figure 5.5 *The "digital" transfer function of a DROS. The upper (middle) graph displays the average pulse rate of the signal (reference) SQUID as a function of the signal flux. The lower graph represents the difference between both pulse rates.*

only the signal SQUID participates in the relaxation oscillations, $\langle f_{sig} \rangle = f_{RO}$ and $\langle f_{ref} \rangle = 0$. On the other hand, if the value of the signal flux is such that only the reference SQUID oscillates, $\langle f_{ref} \rangle = f_{RO}$ and $\langle f_{sig} \rangle = 0$. The width of the transition between these two extremes, $\Delta\Phi$, can be calculated with Eq. (4.3b). The action of the digital counter depends on the value of $\langle f_{sig} - f_{ref} \rangle$, plotted in the lower graph of Fig. 5.5. If the smart DROS operates, both SQUIDs have a switching probability of 50%, which implies that $\langle f_{sig} - f_{ref} \rangle = 0$. In the locking point, the "digital" transfer function of the DROS is $\partial\langle f_{sig} - f_{ref} \rangle / \partial\Phi_{sig} = 2f_{RO}/\Delta\Phi$.

The functional diagram of the smart DROS is depicted in Fig. 5.6. The transfer functions of the DROS and the counter are indicated in this figure, where j represents the imaginary unit. These transfer functions describe all signals as continuously varying quantities, disregarding the digital character of the system. Therefore, the model of Fig. 5.6 is only valid for frequencies well below f_{RO}. The transfer function $\partial\Phi_{fb}/\partial\Phi_{sig}$ of the system in Fig. 5.6 is

$$\frac{\partial\Phi_{fb}}{\partial\Phi_{sig}} = \frac{\left(2f_{RO}/\Delta\Phi\right)\cdot\left(\delta\Phi_{fb}/j\omega\right)}{1+\left(2f_{RO}/\Delta\Phi\right)\cdot\left(\delta\Phi_{fb}/j\omega\right)} = \frac{1}{j\omega\tau+1} \quad , \quad \tau = \frac{\Delta\Phi}{2f_{RO}\cdot\delta\Phi_{fb}}. \qquad (5.3)$$

This is the frequency response of a first-order low pass filter with a -3 dB bandwidth of $1/(2\pi\tau) = (1/\pi)\cdot f_{RO}\cdot(\delta\Phi_{fb}/\Delta\Phi)$. This implies that the bandwidth of the on-chip flux locked loop is considerably below the relaxation frequency when $\delta\Phi_{fb} \ll \Delta\Phi$, a situation which can occur in practical devices. The maximum slew rate of the smart DROS is given by Eq. (5.2), substituting the relaxation oscillation frequency f_{RO} instead of f_c.

5.2.3 Sensitivity of the smart DROS

At the operation point, both SQUIDs of the DROS have an equal switching probability of 50% and the "digital" transfer function of the DROS is given by $\partial\langle f_{sig} - f_{ref} \rangle / \partial\Phi_{sig} = 2f_{RO}/\Delta\Phi$. As is derived in ref. [12], the 50% switching probability of both SQUIDs causes an equivalent flux noise of

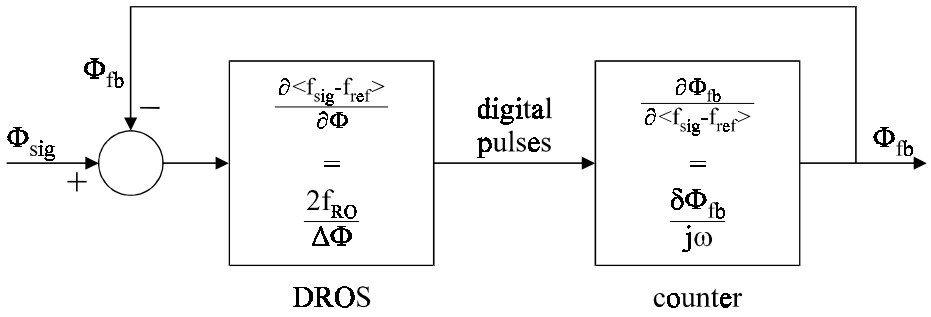

Figure 5.6 *Block scheme of the smart DROS.*

$$S_{\Phi,digital} = \frac{\Delta\Phi^2}{4f_{RO}}, \tag{5.4}$$

where the index “digital” refers to the digital readout scheme.

The flux noise of a DROS with the conventional analogue readout scheme, $S_{\Phi,analogue}$, was derived in section 4.1.3. By substituting Eqs. (4.3a) and (4.4a) in Eq. (4.4b), one obtains

$$S_{\Phi,analogue} = \frac{S_V}{\left(\partial V/\partial\Phi_{sig}\right)^2} = \frac{\left(V_c^2/4f_{RO}\right)}{\left(V_c/\Delta\Phi\right)^2} = \frac{\Delta\Phi^2}{4f_{RO}}. \tag{5.5}$$

A direct comparison of Eqs. (5.4) and (5.5) shows that the intrinsic sensitivity of the DROS is *not* affected by the digital readout scheme.

To prevent the sensitivity of a smart DROS to be limited by *quantization errors*, the quantization unit of the feedback flux should not exceed the broadband flux noise of the DROS:

$$\delta\Phi_{fb} < \sqrt{S_\Phi \cdot f_{RO}}\,. \tag{5.6}$$

From Eqs. (5.6) and (5.4), the maximum allowed value of $\delta\Phi_{fb}$ follows as $\delta\Phi_{fb,max} = \sqrt{(S_\Phi \cdot f_{RO})} = \tfrac{1}{2}\Delta\Phi$. Substituting this value in Eq. (5.3), a theoretical maximum bandwidth of $f_{RO}/2\pi$ results for the smart DROS.

5.3 The Josephson counter

The basic element in the flux locked loop circuitry of a smart DROS is a bi-directional counter, which can be implemented either in semiconducting [19] or in superconducting digital electronics. As the counter and the DROS should preferably be integrated on a single chip, it is natural to use the same, i.e. superconducting, technology for both. However, a digital multi-bit counter based on Josephson electronics has a rather complex architecture. Therefore, we decided to use a relatively simple “semi-digital” counter, based on the counters of the Fujitsu and HYPRES single-chip SQUIDs. In this section, the operation theory of such a *Josephson counter* is explained.

5.3.1 Principle of operation

A schematic diagram of the Josephson counter is shown in Fig. 5.7. It consists of a superconducting storage loop of inductance L_{st}, which is interrupted by two write gates, the *up-gate* and the *down-gate*. These write gates are resistively shunted non-hysteretic dc SQUIDs. The write gates can be compared to “water locks”, admitting flux quanta to (up-gate) or removing flux quanta from (down-gate) the superconducting storage loop.

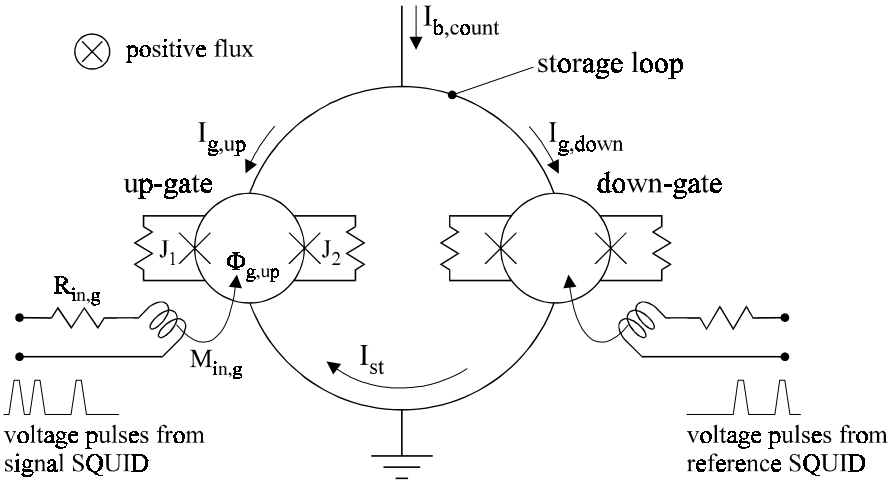

Figure 5.7 *Schematic representation of the Josephson counter.*

The voltage pulses generated by the DROS are converted to flux pulses by means of input coils which have a mutual inductance $M_{in,g}$ with the write gates. The values of $R_{in,g}$ and $M_{in,g}$ should be dimensioned to yield an amplitude of approximately 1 Φ_0 for the flux pulses which are coupled to the write gates. Furthermore, the time constant $L_{in,g}/R_{in,g}$, $L_{in,g}$ being the inductance of the input coils, should be smaller than the typical pulse duration.

Figure 5.8a shows the threshold characteristic of the up-gate. If the applied flux $\Phi_{g,up}$ is increased, starting at point A of Fig. 5.8a, the write gate remains in the n = 0 flux quantum state by the induction of an anti-clockwise screening current in its SQUID loop. This screening current causes the current through junction J_1 to increase while the current through junction J_2 decreases. At point B of Fig. 5.8a, the current through junction J_1 reaches its critical value and J_1 switches momentarily to the voltage state. As the junction is non-hysteretic, the normal conducting state does not persist and J_1 switches back to the zero-voltage state after having generated an SFQ-pulse. This SFQ-pulse causes the phase difference across J_1 to make a "2π-leap", and therefore the write gate enters the n = 1 flux quantum state. This is a very fast process on a typical time scale of the order of 10 ps [10]. The 2π phase leap of J_1 causes the phase difference across the entire up-gate, ϕ_{up}, to increase by π radians.

The flux quantization condition, see section 2.1.2, imposes that

$$I_{st} \cdot L_{st} + \frac{\left(\phi_{down} - \phi_{up}\right)}{2\pi} \cdot \Phi_0 = 0\,, \tag{5.7}$$

where ϕ_{up} and ϕ_{down} represent the phase differences across the up-gate, respectively the down-gate, and I_{st} is the circulating current in the storage loop.

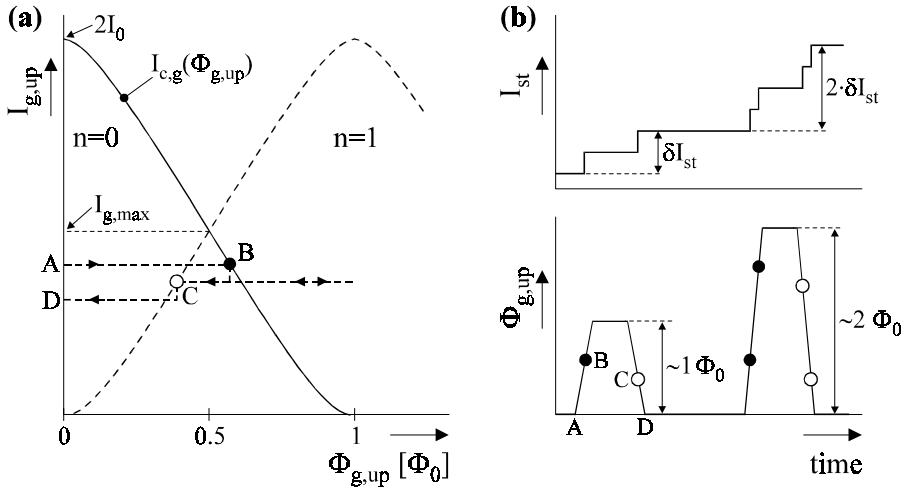

Figure 5.8 **(a)** *Threshold characteristic of the up-gate for the n = 0 and the n = 1 flux quantum states. When a flux quantum is written, the path A-B-C-D is followed. The black circle indicates the point were junction J_1 generates an SFQ-pulse and the open circle marks the point where J_2 produces an SFQ-pulse.* **(b)** *The flux writing process as a function of time. The first pulse adds one flux quantum to the flux in the storage loop, whereas the second pulse adds two flux quanta.*

Consequently, the phase jump across the up-gate of π radians implies that I_{st} increases by an amount of $\Phi_0/2L_{st}$. As I_{st} increases, the current $I_{g,up}$ through the up-gate decreases, whereas the current through the down-gate, $I_{g,down}$, increases, both by an amount of $\Phi_0/2L_{st}$.

If $\Phi_{g,up}$ is decreased again, the write gate stays in the n = 1 state by inducing a clockwise screening current in its SQUID loop, until point C in Fig. 5.8a is reached. At this point, junction J_2 reaches its critical current and produces a phase slip of 2π, so that the write gate re-enters the n = 0 state. This 2π phase leap of J_2 causes ϕ_{up} to be increased by π radians. Consequently, I_{st} increases once again by an amount of $\Phi_0/2L_{st}$. Thus, the total current rise in the storage loop, δI_{st}, is given by

$$\delta I_{st} = \frac{\Phi_0}{L_{st}}. \tag{5.8}$$

In Fig. 5.8b, the flux writing process is illustrated schematically as a function of time. The number of flux quanta that is written to the storage loop depends on the amplitude of the input pulses. For example, the second pulse of Fig. 5.8b has an amplitude of ~2 Φ_0 instead of ~1 Φ_0, which causes the addition of *two* flux quanta to the stored flux.

The function of the down-gate is identical to that of the up-gate, but as the sign of ϕ_{down} in Eq. (5.7) is opposite to that of ϕ_{up}, flux pulses which are applied to the down-gate cause a decrease of I_{st} instead of an increase.

5.3.2 Output range of the Josephson counter

The write gates can only operate properly when the following conditions are satisfied:

$$0 < I_{g,up} < I_{g,max} \qquad \text{and} \qquad 0 < I_{g,down} < I_{g,max} \ , \tag{5.9}$$

with $I_{g,max}$ as indicated in Fig. 5.8a. In fact, $I_{g,max}$ is the critical current of the write gates at $\Phi = (n+½)\cdot\Phi_0$, which is, according to Eq. (2.14), equal to

$$I_{g,max} = \frac{\beta_{L,g}}{1+\beta_{L,g}} \cdot 2I_0 \, , \tag{5.10}$$

where I_0 represents the critical current of one junction and $\beta_{L,g}$ is the screening parameter of the write gates. Using the following circuit equations:

$$I_{b,count} = I_{g,up} + I_{g,down} \tag{5.11a}$$

and

$$I_{st} = \frac{I_{g,down} - I_{g,up}}{2} \, , \tag{5.11b}$$

the boundary conditions of Eq. (5.9) imply that

$$\left|I_{st}\right| < \min\left(\frac{I_{b,count}}{2} \, , I_{g,max} - \frac{I_{b,count}}{2} \right). \tag{5.12a}$$

As I_{st} can have positive and negative values, the peak-to-peak range for I_{st} is given by

$$\Delta I_{st} = \min\left(I_{b,count} \ , 2I_{g,max} - I_{b,count} \right). \tag{5.12b}$$

According to Eq. (5.12b), the output range ΔI_{st} is maximum when $I_{b,count} = I_{g,max}$, in which case $\Delta I_{st} = I_{g,max}$.

5.4 Numerical simulations of a smart DROS

Before starting the design and fabrication of the smart DROS, the dynamic behaviour of the device was investigated by means of numerical simulations. For that purpose, the scheme shown in Fig. 5.9 was implemented in the numerical simulation program JSIM [20].

The parameter values listed in Fig. 5.9 are typical, with the exception of the value of L_{st} = 50 nH. This small value was chosen to speed up the numerical simulation process. For the same reason, a DROS with a reference junction instead of a reference SQUID was used in the simulations. The time constant of the DROS, L_{sh}/R_{sh} = 10 ns, implies a relaxation frequency of $f_{RO} \approx 100$ MHz. The L_{sh}-C_{sq} resonances in the DROS are suppressed with a damping resistance of R_d = 30 Ω, giving a damping parameter of D = 2.8 [from Eq. (3.1)]. The values of $M_{in,g}$ = 480 pH and $R_{in,g}$ = 80 Ω imply an amplitude of ~2 Φ_0 for the flux pulses applied to the write gates. As $R_{in,g} > R_d$, the operation of the DROS is not strongly influenced by the readout circuitry.

In the preliminary simulations, either M_{fb} or $M_{in,g}$ was set to zero for a detailed examination of the interaction between the DROS and the Josephson counter. Trace (a) of Fig. 5.10 shows the results of a numerical simulation with M_{fb} = 0. The signal flux was varied in time in such a way that $I_{c,sig} > I_{c,ref}$ for t < 25 ns and $I_{c,sig} < I_{c,ref}$ for t > 25 ns. Consequently, for t < 25 ns, only the reference junction participates in the relaxation oscillations, whereas only the signal SQUID oscillates for t > 25 ns. As expected, the voltage pulses generated

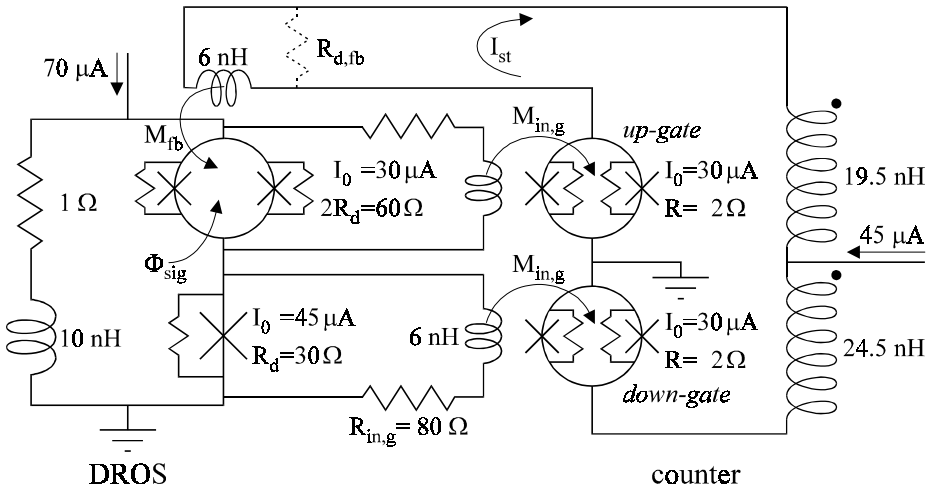

Figure 5.9 *Diagram of the circuit which was used to investigate the dynamic behaviour of a smart DROS by means of numerical simulations. The inductance of all SQUIDs is 60 pH, the capacitance of all Josephson junctions is 0.5 pF, and $M_{fb} = M_{in,g}$ = 480 pH.*

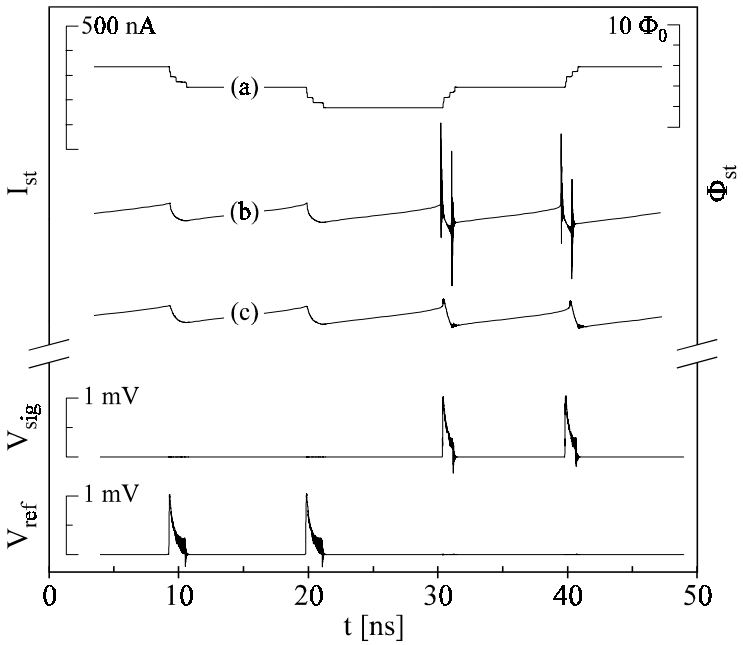

Figure 5.10 *Numerical simulations of the circuit in Fig. 5.9 for three different sets of parameters. V_{ref} is the voltage across the reference junction of the DROS, V_{sig} is the voltage across the signal SQUID, I_{st} is the circulating current in the storage loop and $\Phi_{st} = L_{st} \cdot I_{st}$ represents the stored flux. The signal flux was varied in such a way that $I_{c,sig} > I_{c,ref}$ for $t < 25$ ns and $I_{c,sig} < I_{c,ref}$ for $t > 25$ ns. Trace (a): $M_{fb} = 0$, $R_{d,fb} = \infty$, $M_{in,g} = 480$ pH. Trace (b): $M_{fb} = 480$ pH, $R_{d,fb} = \infty$, $M_{in,g} = 0$. Trace (c): $M_{fb} = 480$ pH, $R_{d,fb} = 30\ \Omega$, $M_{in,g} = 0$. The other parameters are indicated in Fig. 5.9.*

by the reference junction cause the circulating current in the counter to decrease, whereas the pulses produced by the signal SQUID cause I_{st} to increase. As the amplitude of the flux pulses applied to the write gates is ~2 Φ_0, each relaxation oscillation pulse causes the stored flux to increase or decrease by an amount of 2 Φ_0.

Trace (b) of Fig. 5.10 shows a simulation in which $M_{in,g}$ was set to zero, whereas the value of M_{fb} was restored to 480 pH. The signal flux was varied in the same way as for trace (a). As $M_{in,g} = 0$, no flux pulses were applied to the write gates in this simulation. Nevertheless, as the relaxation oscillations in the DROS cause the net flux in the signal SQUID to fluctuate, current oscillations are induced in the counter via the mutual inductance between the signal SQUID and the feedback coil. These oscillations of I_{st} "reflect" the relaxation oscillations in the DROS.

When the reference junction oscillates, the relaxation oscillations induce smooth current fluctuations in the counter. However, when the signal SQUID oscillates, large current spikes are induced in the counter when the signal SQUID switches from the superconducting state to the normal state and vice versa. These spikes, which could possibly degrade the operation of the counter, can be reduced by shunting the feedback coil with a damping resistor $R_{d,fb}$, as shown in Fig. 5.9. For high frequencies, $R_{d,fb}$ constitutes a lower impedance than the storage inductor, and therefore the current spikes will flow through $R_{d,fb}$ rather than through the counter inductance. To prevent phase shifts in the feedback loop, the value of $R_{d,fb}$ has to be such that the time constant $L_{fb}/R_{d,fb}$ is much smaller than $1/f_{RO}$. Furthermore, the additional flux noise due to the Johnson noise generated by $R_{d,fb}$, $\sqrt{S_\Phi} = M_{fb}\cdot\sqrt{(4k_BT/R_{d,fb})}$, should be negligible compared to the intrinsic noise of the DROS. Trace (c) of Fig. 5.10 shows a numerical simulation with the same parameters as for trace (b), but now with $R_{d,fb} = 30\ \Omega$. As expected, the current spikes in the counter are strongly suppressed by the addition of $R_{d,fb}$.

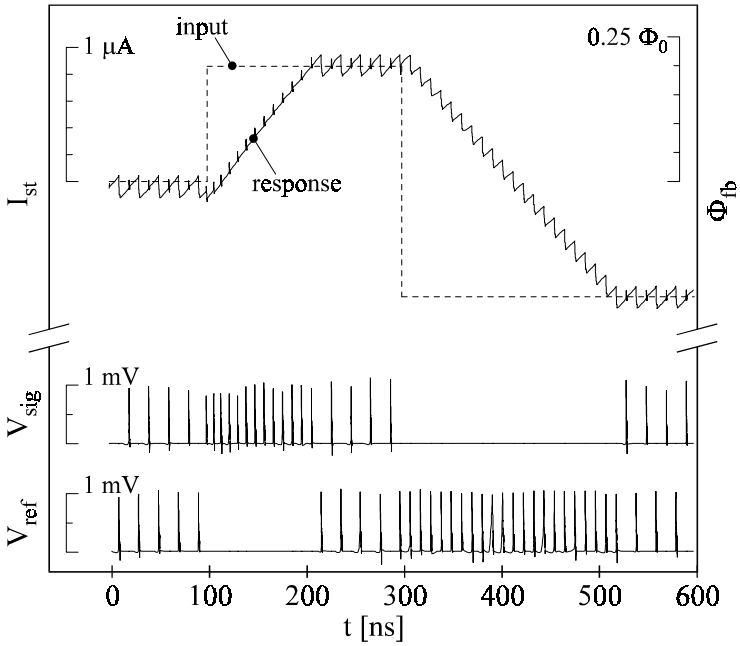

Figure 5.11 *Numerical simulation of the response of a smart DROS to variations of the input flux. V_{ref} is the voltage across the reference junction of the DROS, V_{sig} is the voltage across the signal SQUID, I_{st} is the circulating current in the storage loop and $\Phi_{fb} = M_{fb}\cdot I_{st}$ represents the feedback flux.*
Simulation parameters: $M_{in,g} = M_{fb} = 480$ pH, $R_{d,fb} = 30\ \Omega$, other parameters as indicated in Fig. 5.9.

Figure 5.11 shows a numerical simulation of a smart DROS in operation. Initially, the system is in its dynamic equilibrium, and the reference junction and the signal SQUID pulse alternately. Consequently, the current in the counter oscillates around an average value. At t = 100 ns, a flux step of 0.2 Φ_0 is applied, disturbing the dynamic equilibrium of the system. As a result, only the signal SQUID produces voltage pulses, causing the circulating current in the counter - and accordingly the feedback flux - to increase steadily until the system has established a new dynamic equilibrium. At t = 300 ns, a flux step of -0.4 Φ_0 is applied and now only the reference SQUID generates pulses in order to restore the dynamic equilibrium.

The simulations in Fig. 5.11 show that the output of the smart DROS tracks the input flux, which indicates proper operation.

5.5 Experimental investigation of the Josephson counter

The numerical simulations in the previous section show that, in theory, the construction of a smart DROS based on a Josephson counter is possible. Before designing and constructing a fully integrated smart DROS, we first developed a prototype of the Josephson counter to investigate its characteristics. This is described in the present section.

5.5.1 Chip layout of the Josephson counters

For an experimental investigation of the Josephson counter, devices like the one shown in Fig. 5.12 have been designed, fabricated and characterized. The devices were fabricated with our standard Nb/AlO_x thin film process, having a minimum feature size of 4 μm.

The write gates are non-hysteretic washer-type dc SQUIDs, each with a 10-turns input coil. The hole size of the washers, 20 μm, corresponds to an inductance of 32 pH. The actual SQUID inductance was measured to be $L_{sq,g} \approx 75$ pH ($\beta_{L,g} \approx 2.2$), which is about twice the hole inductance, probably due to the parasitic inductance of the slit. The mutual inductance between the input coils and the write gates was measured to be $M_{in,g} \approx 480$ pH. The critical current of the 4 x 4 μm^2 Josephson junctions is $I_0 \approx 30$ μA and the experimental value of the shunt resistor across the junctions is 1.5 Ω. With the assumed junction capacitance of 0.5 pF, these parameters yield $\beta_C \approx 0.1$, which implies non-hysteretic junction behaviour.

The storage inductor, having a design value of 600 nH, is composed of four two-layer multi-turn coils of the same type that was used in early DROS experiments [21,22]. The coils are arranged “gradiometrically” in order to minimize the sensitivity to external noise. This configuration also reduces the magnetic stray fields produced by the storage inductor.

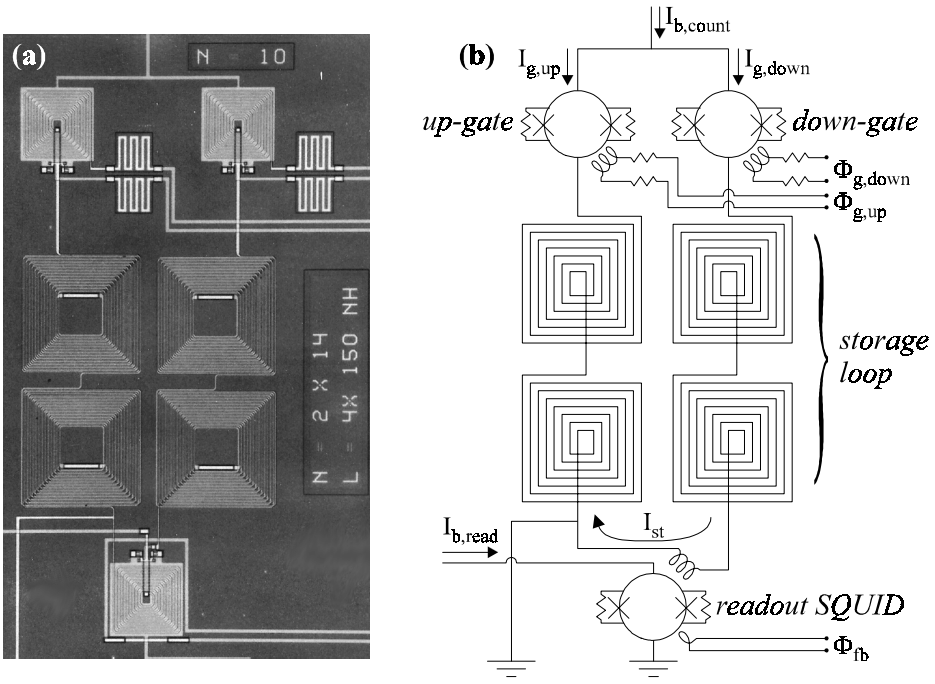

Figure 5.12 (a) *Micrograph and* **(b)** *scheme of the prototype of the Josephson counter. The actual area shown in figure (a) is approximately 1.0 x 1.7 mm².*

The circulating current in the storage loop was measured with an additional non-hysteretic dc SQUID, the *readout SQUID*, located in the "down-branch" of the counter. The additional inductance due to the input coil of this readout SQUID (~5 nH) is negligible in comparison with the other inductances in the storage loop. The parameters of the readout SQUID are equal to those of the write gates. The current $I_{g,down}$ can be calculated from $I_{g,down} = \Phi_{read}/M_{in,read}$, where Φ_{read} represents the flux which is induced in the readout SQUID, and $M_{in,read} \approx 480$ pH is the mutual inductance between the readout SQUID and its input coil. A single-turn feedback coil around the readout SQUID was used for flux locked loop operation.

5.5.2 Characterization of the Josephson counters

Four Josephson counters were tested by applying flux pulses, generated by two function generators, to the write gates. To reduce the influence of environmental electromagnetic noise, the counters were enclosed in a Nb shield. Moreover, all wires between the room temperature environment and the Josephson counters were low pass filtered in order to prevent radio frequency interference (RFI).

The readout SQUID was operated with the DROS flux locked loop electronics of Fig. 4.5. Due to its small flux-to-voltage transfer of ~100 μV/Φ_0, the sensitivity of the readout SQUID was amplifier limited, but this is not an important issue in the present experiments.

The measured response to flux pulses which were applied to the up-gate is shown in Fig. 5.13. The pulses, with a peak-to-peak amplitude of ~24 Φ_0, were applied at a frequency of about 5 Hz. Trace (a) was recorded for $I_{b,count}$ = 0, and represents the direct crosstalk between $\Phi_{g,up}$ and the readout SQUID. Trace (b) was measured at $I_{b,count}$ = 39 μA. By subtracting trace (a) from trace (b), the "parasitic" crosstalk effect was excluded, as shown by trace (c). The latter trace shows a clear correspondence with the model of Fig. 5.8b. If flux pulses were applied to the down-gate, I_{st} decreased instead of increased at each pulse. These measurements indicate that the counters operate as expected.

Figure 5.14 shows the measured response of a counter when pulse trains of ~1800 flux pulses were applied alternately to the up-gate and to the down-gate. The peak-to-peak amplitude of the flux pulses was ~1 Φ_0 for trace (a), ~2 Φ_0 for trace (b) and ~3 Φ_0 for trace (c). Consequently, the gates wrote respectively one, two or three flux quanta to the storage loop at each pulse. From the amplitudes

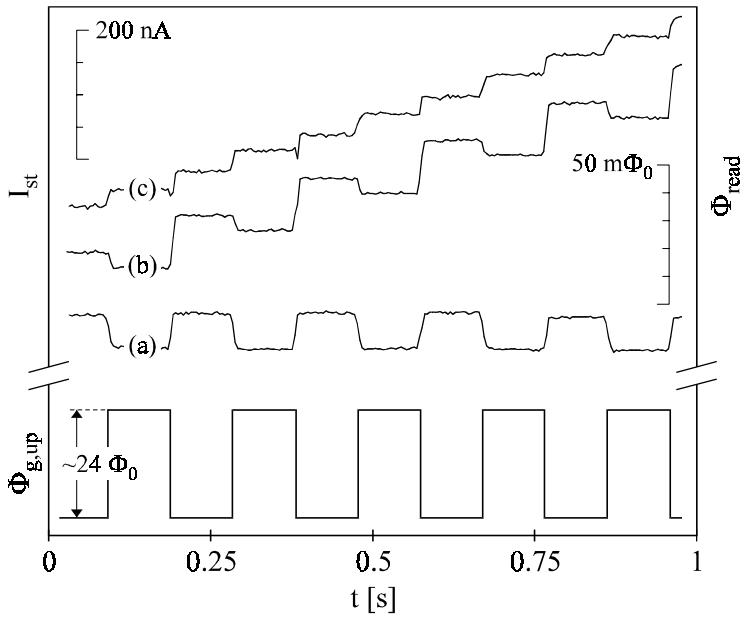

Figure 5.13 *Experimental response of a Josephson counter to flux pulses at the up-gate. Trace (a) was measured at $I_{b,count}$ = 0 μA and trace (b) at $I_{b,count}$ = 39 μA. Trace (c) gives the difference between trace (b) and trace (a). The vertical offsets are arbitrary.*

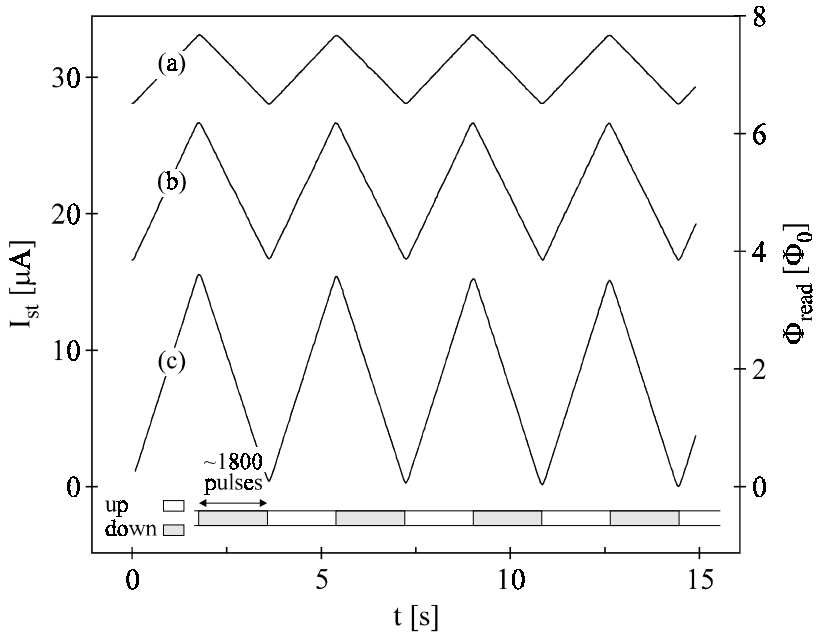

Figure 5.14 *Experimental response of a Josephson counter to pulse trains of ~1800 pulses each, applied alternately to the up-gate and to the down-gate. The amplitude of the applied flux pulses was about 1 Φ_0 for trace (a), 2 Φ_0 for trace (b) and 3 Φ_0 for trace (c). The counter bias current was $I_{b,count}$ = 30 μA for all traces. The vertical offsets are arbitrary.*

of the traces [5.1 μA for trace (a), 10.0 μA for trace (b) and 15.1 μA for trace (c)], the value of L_{st} was determined to be L_{st} = 750 nH (±10%). Two of the investigated Josephson counters showed a much lower value for L_{st}, which was attributed to electrical shorts in the two-layer multi-turn storage inductors.

For determination of the output range of the counters, ΔI_{st}, the number of applied flux pulses was increased until the current in the storage loop saturated, as is illustrated by the measurements in Fig. 5.15a.

Figure 5.15b shows the measured values of ΔI_{st} as a function of $I_{b,count}$. For this particular device, the critical current of the Josephson junctions was ~45 μA instead of 30 μA. The solid line in Fig. 5.15b is a fit according to Eq. (5.12b), using $I_{g,max}$ = 75 μA. This fit value is in good agreement with the theoretical expectation of 70 μA, obtained from Eq. (5.10). Obviously, the experimental relation between ΔI_{st} and $I_{b,count}$ is well described by Eq. (5.12b).

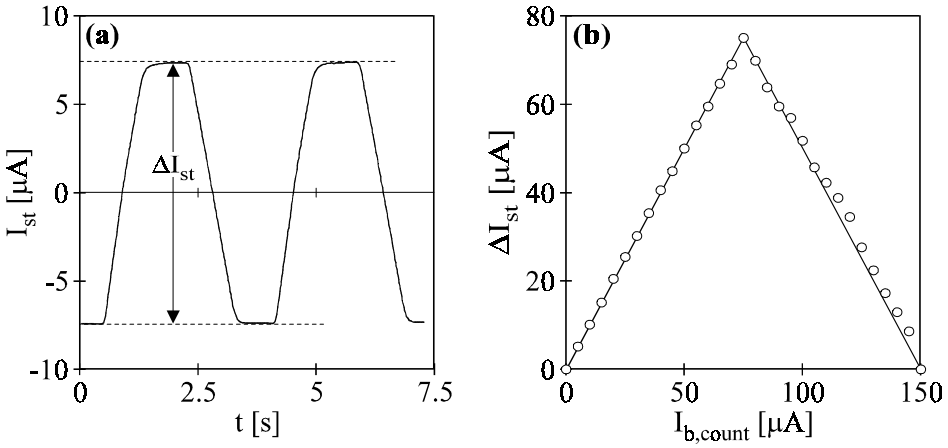

Figure 5.15 (a) *Experimental response of a Josephson counter to pulse trains, applied alternately to the up-gate and to the down-gate, at a counter bias current of $I_{b,count}$ = 15 μA. The number of flux pulses was sufficiently large to saturate the current in the storage loop. The positive and negative saturation levels are indicated by the horizontal dashed lines.* **(b)** *Peak-to-peak output range as a function of the applied bias current. The solid line is a fit according to Eq. (5.12b). The maximum value of ΔI_{st} = 75 μA corresponds to a flux change of ~$2.5 \cdot 10^4$ Φ_0 in the storage loop.*

5.6 Experimental investigation of the smart DROS

Using the theoretical results of section 5.4 and the experimental results of section 5.5, an integrated smart DROS was designed. This fully operational prototype is discussed in this section.

5.6.1 Design of the smart DROS

A micrograph and the scheme of the fabricated smart DROSs are presented in Fig. 5.16a (page 124) respectively Fig. 5.16b (page 125). The main parameters of the device are listed next to Fig. 5.16b. The devices, having a minimum feature size of 4 μm, were fabricated using our standard Nb/AlO_x thin film process. For testing purposes, also separate elements of the smart DROS, such as the DROS, the Josephson counter or the readout SQUID, were fabricated on the same wafer as the compound devices.

As for the Josephson counters described in the previous section, an additional non-hysteretic dc SQUID with its own room temperature flux locked loop circuitry was used for the readout of the smart DROS. This readout scheme limits the practical versatility of the prototype because it still requires external flux locked loop circuitry for operation, but the main goal of the present device was to demonstrate the viability of the smart DROS concept. In section 5.7, some alternative readout schemes will be suggested.

Both the readout SQUID and the DROS are magnetically coupled to the counter via *intermediate flux transformers*. Due to the gradiometric layout of these flux transformers, fluctuations in the bias current of the counter, $I_{b,count}$, do not induce flux variations in the DROS or in the readout SQUID. The effective magnetic coupling between the circulating current in the counter and the signal SQUID of the DROS was measured to be $M_{fb,eff} = \partial\Phi_{fb}/\partial I_{st} = 0.15$ nH, and the experimental value of the coupling between I_{st} and the readout SQUID is $M_{read,eff} = \partial\Phi_{read}/\partial I_{st} = 0.60$ nH. Thus, if Φ_{sig} is changed by an amount of 1 Φ_0, the on-chip feedback loop will react by changing Φ_{fb} by the same amount, but in opposite direction, which corresponds to a flux change of $M_{read,eff}/M_{fb,eff} \cdot 1\ \Phi_0 = 4.0\ \Phi_0$ in the readout SQUID.

The Josephson counter in the smart DROS prototype is based on the design which was discussed in section 5.5. The inductance of the storage loop was measured to be $L_{st} = 840$ nH (±5%). The difference of about 90 pH with respect to the inductance of the simple Josephson counters of section 5.5 is caused by the additional inductance of the intermediate flux transformers. The value of $R_{in,g} = 80\ \Omega$ was chosen on the basis of the numerical simulations of section 5.4. The current spikes which are induced in the counter by the relaxation oscillations in the DROS are suppressed with two resistors of 200 Ω each.

The design value of the DROS time constant, $L_{sh}/R_{sh} = 10$ ns, implies a relaxation frequency of $f_{RO} \approx 100$ MHz, which was confirmed experimentally. Several test-DROSs, of the same layout as in Fig. 5.16, but not coupled to a Josephson counter, were characterized with the standard DROS measurement setup of Fig. 4.5. The experimental V-Φ_{sig} characteristic of one of the test-DROSs is plotted in Fig. 5.17 on page 126. This curve was obtained at a bias current of 125 μA, which was typically the optimum bias current for the test-DROSs. This is in good agreement with the theoretical maximum bias current of 140 μA calculated with Eq. (4.1). In accordance with Eq. (4.3c), the typical flux-to-voltage transfer of the test-DROSs was around 2 mV/Φ_0. However, the white flux noise of the test-devices, $\sqrt{S_\Phi} = 7$ .. 8 $\mu\Phi_0/\sqrt{\text{Hz}}$, was larger than the theoretical value of ~2.5 $\mu\Phi_0/\sqrt{\text{Hz}}$ [from Eq. (4.4b)]. The low value of the damping parameter of the test-DROSs, $D = 0.4$, could be at the origin of this excess noise. Furthermore, the parasitic capacitance of the multi-turn shunt inductors could give rise to parasitic resonances in the DROS, which also decreases its sensitivity.

(a)

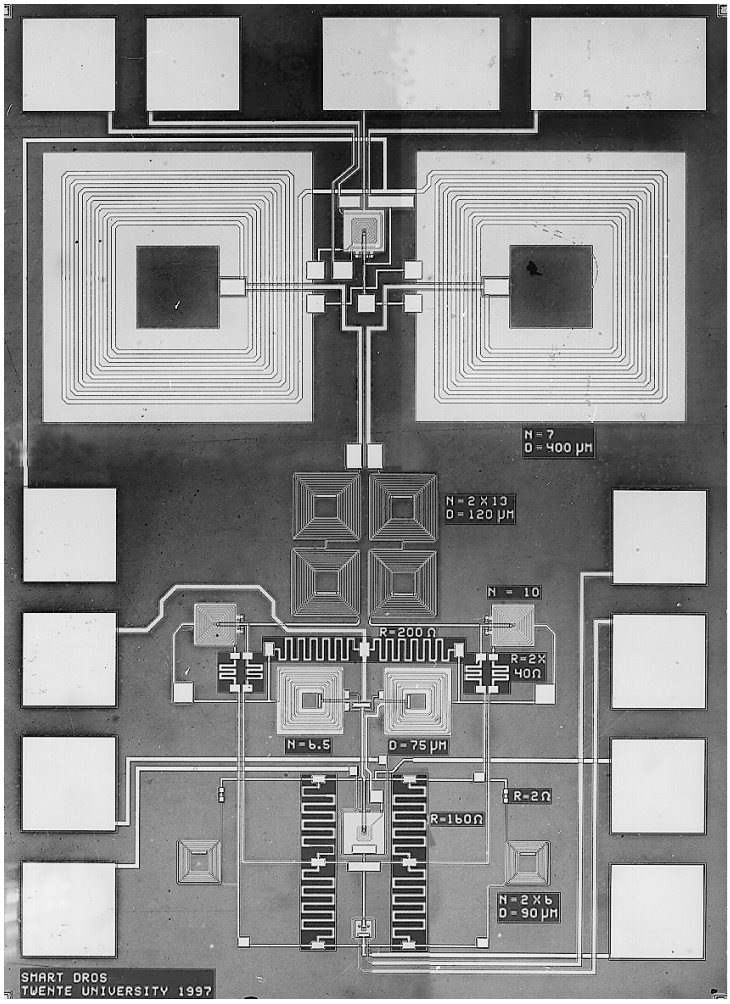

Figure 5.16 (a) *Micrograph and* **(b)** *scheme of the prototype of the smart DROS. The actual size of the device is 3.6 x 4.9 mm². The critical current of all Josephson junctions is ~30 μA, and the estimated junction capacitance is 0.5 pF. The measured value of the shunt resistors across the non-hysteretic junctions in the readout SQUID and in both write gates is 1.5 Ω ($\beta_C \approx 0.1$). The parameter values listed in figure (b) are either design values [marked with a)] or measured values [marked with b)].*

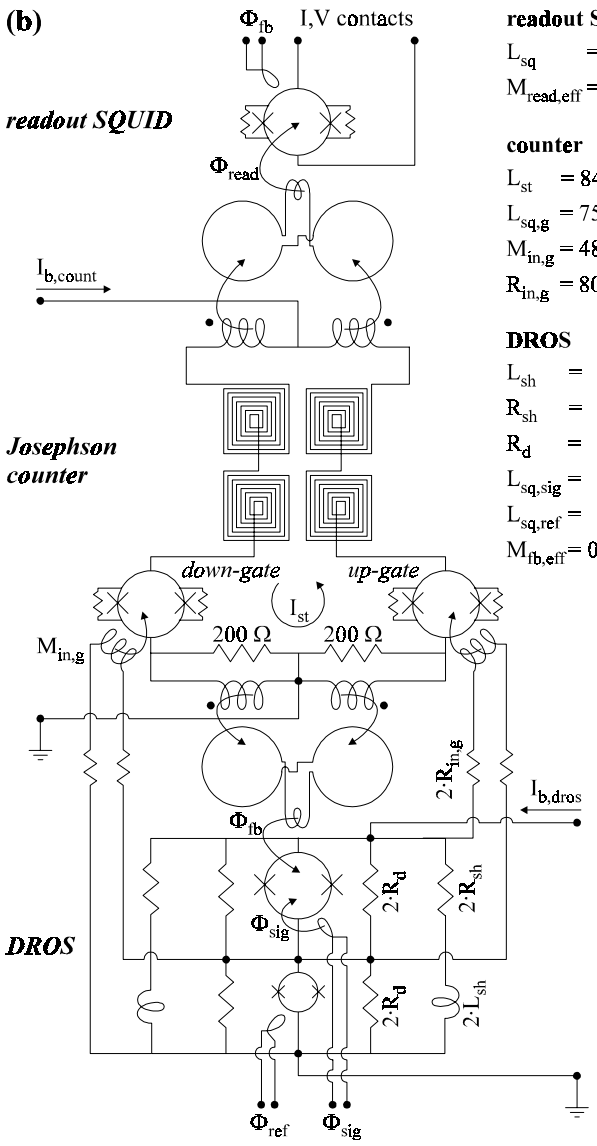

readout SQUID
L_{sq} = 75 pH [b)]
$M_{read,eff}$ = 0.60 nH [b)]

counter
L_{st} = 840 nH [b)]
$L_{sq,g}$ = 75 pH [b)]
$M_{in,g}$ = 480 pH [b)]
$R_{in,g}$ = 80 Ω [a)]

DROS
L_{sh} = 10 nH [a)]
R_{sh} = 1 Ω [a)]
R_d = 80 Ω [a)]
$L_{sq,sig}$ = 75 pH [b)]
$L_{sq,ref}$ = 32 pH [b)]
$M_{fb,eff}$ = 0.15 nH [b)]

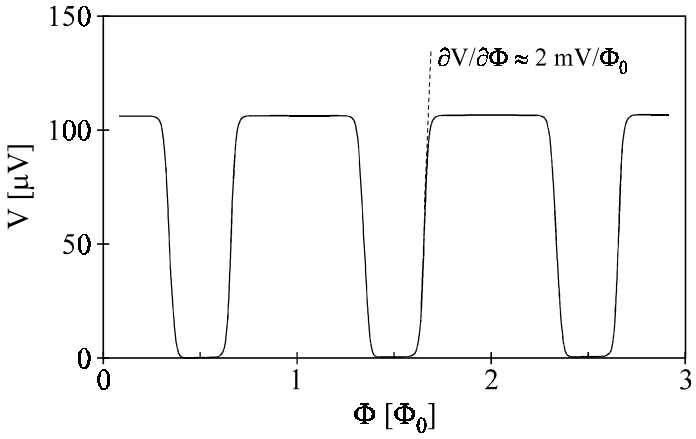

Figure 5.17 *Experimental V-Φ_{sig} characteristic of one of the test-DROSs at a bias current of $I_{b,dros}$ = 125 μA.*

5.6.2 Operation of the smart DROS

Four smart DROSs were characterized experimentally. The devices were shielded from external noise sources by means of a superconducting Nb shielding, and all electrical connections between the room temperature electronics and the smart DROSs were low pass filtered for RFI suppression. The readout SQUID was operated in a simple flux locked loop without flux modulation.

In Fig. 5.18a, the transfer function of one of the smart DROSs is shown for nine different values of $I_{b,count}$. The settings of the DROS, Φ_{ref} and $I_{b,dros}$, were not changed for the different traces. The horizontal axis of Fig. 5.18a shows the applied signal flux, Φ_{sig}, and the vertical axis gives the resulting flux in the readout SQUID, Φ_{read}. The linear relation between Φ_{sig} and Φ_{read} clearly shows that the device works according to the theory of section 5.4.

As discussed in section 5.3.2, the output range of the Josephson counter depends on the value of $I_{b,count}$. For the device in Fig. 5.18, the operation range increased linearly with $I_{b,count}$ until $I_{b,count} \approx 50$ μA. Above that value, the output range of the Josephson counter decreased again, cf. Fig. 5.15b. At $I_{b,count}$ = 50 μA, the smart DROS showed a linear response over a Φ_{sig} range of almost 3 Φ_0.

The slope of the characteristics in Fig. 5.18a is $\partial\Phi_{read}/\partial\Phi_{sig}$ = 3.9. Averaged over the four characterized devices, the value of $\partial\Phi_{read}/\partial\Phi_{sig}$ was $\langle\partial\Phi_{read}/\partial\Phi_{sig}\rangle$ = 3.95, with a maximum deviation of ±2%. This is in good agreement with the value of $M_{read,eff}/M_{fb,eff}$ = 4.0.

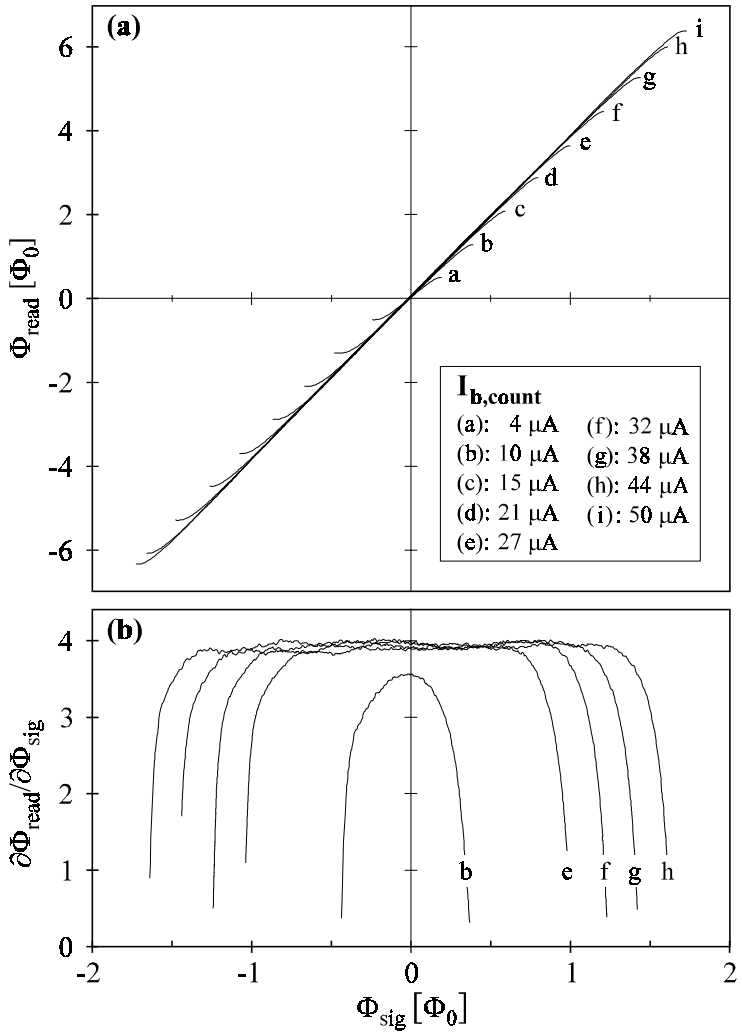

Figure 5.18 (a) *Experimental transfer function of a smart DROS for different values of $I_{b,count}$. The horizontal axis displays the applied signal flux, and the vertical axis gives the resulting flux in the readout SQUID.* **(b)** *The slope $\partial\Phi_{read}/\partial\Phi_{sig}$ of some of the characteristics in figure (a).*

To investigate the linearity of the system, the local slope $\partial\Phi_{read}/\partial\Phi_{sig}$ of the characteristics in Fig. 5.18a was measured by superposing a sinusoidal signal with a frequency of 500 Hz and an amplitude of ~0.01 Φ_0 on the slow (~0.1 Hz) sweep of Φ_{sig}. With an analogue lock-in amplifier [23], the amplitude of the resulting 500 Hz fluctuation of Φ_{read}, which is proportional to $\partial\Phi_{read}/\partial\Phi_{sig}$, was measured. Figure 5.18b shows the experimental results for several values of

$I_{b,count}$. For each bias current, the value of $\partial\Phi_{read}/\partial\Phi_{sig}$ at the plateau is constant within a relative range of ±2.5%. As the traces in Fig. 5.18b did not show hysteresis when the sweep direction of Φ_{sig} was changed, motion of pinned flux is not likely to be the mechanism behind the small fluctuations of $\partial\Phi_{read}/\partial\Phi_{sig}$. Probably, the parasitic magnetic coupling between the different elements of the smart DROS is the malefactor.

Trace (a) of Fig. 5.19 shows the experimental flux noise spectrum of one of the characterized devices. The white flux noise level of $\sqrt{S_{\Phi,sig}} \approx 6.5\ \mu\Phi_0/\sqrt{\text{Hz}}$ corresponds to an energy sensitivity of $\varepsilon \approx 2000\ h$. As a result of the non-modulated flux locked loop configuration, the readout SQUID has a rather high white flux noise level of ~16 $\mu\Phi_0/\sqrt{\text{Hz}}$. Taking into account the flux gain of 4.0, this corresponds to a contribution of 4 $\mu\Phi_0/\sqrt{\text{Hz}}$ to the overall flux noise, as plotted in trace (b) of Fig. 5.19. Subtracting the noise of the readout SQUID from the total flux noise, the intrinsic flux noise level of the smart DROS was deduced to be ~5 $\mu\Phi_0/\sqrt{\text{Hz}}$ ($\varepsilon_{intr} \approx 1150\ h$).

Trace (c) of Fig. 5.19 shows the flux noise of the same DROS, but now operated in a conventional flux locked loop at room temperature. For this measurement, the DROS and the counter were disconnected by scratching the resistors $R_{in,g}$ mechanically. The measured white flux noise, 7 $\mu\Phi_0/\sqrt{\text{Hz}}$, is almost identical to the overall flux noise (~6.5 $\mu\Phi_0/\sqrt{\text{Hz}}$), and somewhat above the intrinsic flux noise (~5 $\mu\Phi_0/\sqrt{\text{Hz}}$) of the smart DROS. Thus, the intrinsic flux noise of the DROS in the smart configuration is even better than in the conventional configuration. The reason could be that the resistors $R_{in,g}$, which

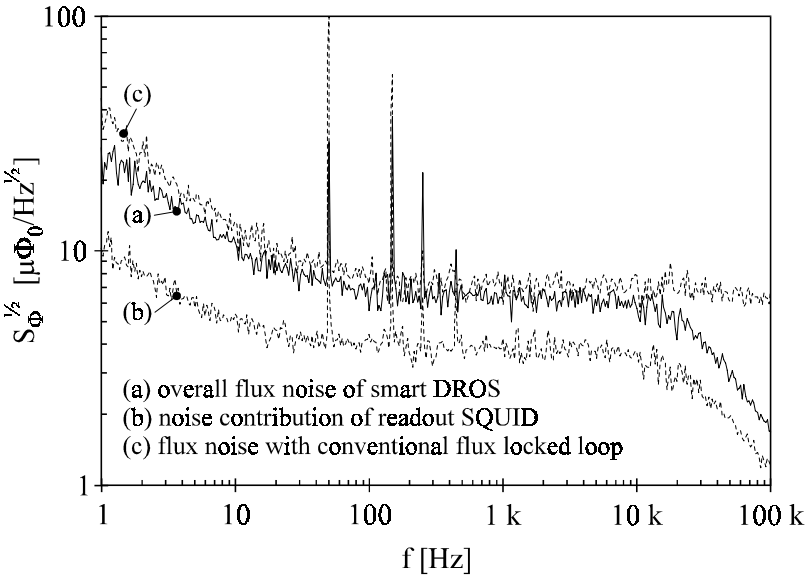

Figure 5.19 *Flux noise spectra of the smart DROS.*

are connected parallel to the damping resistors R_d of the DROS, increase the value of the damping parameter from $D = 0.4$ in the conventional scheme to $D = 1.6$ in the smart configuration.

The bandwidth and the slew rate of the smart DROS prototype could not be determined, since these performance parameters were limited by the flux locked loop circuitry of the readout SQUID, having a bandwidth of about 20 kHz.

5.7 Discussion and conclusions

The results in the previous section prove that the smart DROS works in practice as well as in theory. The energy sensitivity of the presented prototype, $\varepsilon \approx 2000\ h$ ($\varepsilon_{intr} \approx 1150\ h$), is better than that of the Fujitsu single-chip SQUID almost by a factor of two [13]. However, the prototype still needs some fine-tuning to become a device of real practical value.

For instance, the relaxation frequency can be increased to ~1 GHz in order to increase the sensitivity, the bandwidth and the slew rate. Furthermore, a new design for the storage inductor and the intermediate flux transformers can improve the dynamic range of the device considerably. Two last examples of potential improvements are the replacement of the single-turn input coil of the DROS by a multi-turn input coil for efficient coupling with the outside world and the implementation of a reference junction instead of a reference SQUID to reduce the number of wires.

However, all these modifications do not eliminate the bottleneck of the prototype: the readout SQUID, which still requires flux locked loop circuitry at room temperature. Because of this readout SQUID, the initial aim of the smart DROS, operation without external flux locked loop electronics, has not been accomplished yet. Some alternative readout schemes to get around this situation will be discussed below.

The smart DROS could for instance be read out in the same way as the Fujitsu single-chip SQUID by counting the output voltage pulses of the DROS with a room temperature bi-directional counter. With this readout system, a very large dynamic range can be realized when the flux transformer circuit is used as the counter inductance [4]. However, as in the case of frequency readout of a ROS, cryogenic pre-amplification of the voltage pulses, for instance with a high electron mobility transistor (HEMT) [5,24], might be necessary in this case. Furthermore, coaxial transmission lines between the cryogenic environment and the digital counter at room temperature would be required, which introduces a serious heat load problem in multi-channel systems. Therefore, this readout scheme is especially appropriate for applications which require a large measurement bandwidth and a large dynamic range, but only a few channels.

As mentioned in the introduction of section 5.3, the counter of the smart DROS can also be implemented with semiconductor electronics. In ref. [19], for

instance, a cryogenic 12 bit digital counter based on conventional CMOS integrated circuits is presented. A smart DROS based on such a semiconducting counter would generate an output voltage depending linearly on the input flux. As it is not straightforward to integrate the superconducting and the semiconducting elements of such a “hybrid” smart DROS on a single chip, it would consist of several discrete components, which increases the system complexity. However, the number of wires between the environment and the SQUIDs in a multi-channel system could be reduced drastically with this configuration, which is a large advantage. Moreover, for low signal frequencies, as for instance in bio-magnetic applications, simple wires instead of coaxial lines would suffice for the readout of a “hybrid” smart DROS.

Further development of the smart DROS, following the recommendations above, offers the perspective of a very sensitive, fast and versatile SQUID sensor.

References

[1] N. Fujimaki, “Josephson integrated circuits III. A single-chip SQUID magnetometer”, *Fujitsu Sci. Tech. J.* **27**, 59-83 (1991).

[2] http://www.hypres.com/~masoud/digital.shtml

[3] N. Fujimaki, H. Tamura, T. Imamura and S. Hasuo, “A single-chip SQUID magnetometer”, *IEEE Trans. Electron Devices* **35**, 2412-2418 (1988).

[4] M. Radparvar, “A wide dynamic range single-chip SQUID magnetometer”, *IEEE Trans. Appl. Supercond.* **4**, 87-91 (1994).

[5] U. Fath, R. Hundhausen, T. Fregin, P. Gerigk and W. Eschner, “Experimental digital SQUID with integrated feedback circuit”, *IEEE Trans. Appl. Supercond.* **7**, 2747-2751 (1997).

[6] S.V. Rylov, “Analysis of high-performance counter-type A/D converters using RSFQ logic/memory elements”, *IEEE Trans. Magn.* **27**, 2431-2434 (1991).

[7] K. Gotoh, N. Fujimaki, H. Suzuki, T. Imamura, S. Hasuo and A. Shibatomi, “Multichannel single-chip SQUID with a Josephson multiplexer”, *Supercond. Sci. Technol.* **4**, 610-612 (1991).

[8] K. Gotoh, N. Fujimaki, T. Imamura and S. Hasuo, “8-channel array of single-chip SQUIDs connection to Josephson multiplexer”, *IEEE Trans. Appl. Supercond.* **3**, 2601-2604 (1993).

[9] Fujitsu Laboratories Ltd., 10-1 Morinosato-Wakamiya, Atsugi 243-01, Japan.

[10] K.K. Likharev and V.K. Semenov, “RSFQ logic/memory family: a new Josephson-junction technology for sub-terahertz-clock-frequency digital systems”, *IEEE Trans. Appl. Supercond.* **1**, 3-28 (1991).

[11] V.K. Semenov and J.A. Polyakov, “Fully integrated digital SQUID”, in abstract book *3rd European Conference on Applied Superconductivity* (EUCAS), abstract no. 10Ge-70, Veldhoven, the Netherlands (1997).

[12] N. Fujimaki, H. Tamura, T. Imamura and S. Hasuo, “Thermal noise-limited sensitivity of the pulse-biased SQUID magnetometer”, *J. Appl. Phys.* **65**, 1626-1630 (1989).

[13] N. Fujimaki, K. Gotoh, T. Imamura and S. Hasuo, “Thermal-noise-limited performance in single-chip superconducting quantum interference devices”, *J. Appl. Phys.* **71**, 6182-6188 (1992).

[14] R.H. Koch, J. Clarke, J.M. Martinis, W.M. Goubau, C.M. Pegrum and D.J. van Harlingen, "Investigation of 1/f noise in tunnel junction dc SQUIDs", *IEEE Trans. Magn.* **19**, 449-452 (1983).

[15] M. Radparvar and S.V. Rylov, "High sensitivity digital SQUID magnetometers", *IEEE Trans. Appl. Supercond.* **7**, 3682-3685 (1997).

[16] P.F. Yuh and S.V. Rylov, "An experimental digital SQUID with large dynamic range and low noise", *IEEE Trans. Appl. Supercond.* **5**, 2129-2132 (1995).

[17] M. Radparvar and S. Rylov, "An integrated digital SQUID magnetometer with high sensitivity input", *IEEE Trans. Appl. Supercond.* **5**, 2142-2145 (1995).

[18] HYPRES Inc., 175 Clearbrook Road, Elmsford, NY 10523, U.S.A.

[19] E. Crocoll, H. Matz, M. Reick and W. Jutzi, "Digital CMOS circuits below 100 K", in *Superconducting Devices and Their Applications*, ed. H. Koch and H. Lübbig, Springer Proceedings in Physics **64**, Springer-Verlag, Berlin / Heidelberg, 362-365 (1992).

[20] Simulation software: JSIM 2.1, developed by E.S. Fang, University of California, Berkeley, CA 94720, U.S.A.

[21] D.J. Adelerhof, *Second generation dc SQUID magnetometers: (Double) Relaxation Oscillation SQUIDs*, Ph.D. thesis University of Twente, Enschede (1993).

[22] D.J. Adelerhof, H. Nijstad, J. Flokstra and H. Rogalla, "Relaxation oscillation SQUIDs with high $\partial V/\partial \Phi$", *IEEE Trans. Appl. Supercond.* **3**, 1862-1865 (1993).

[23] Princeton Applied Research model PAR 124.

[24] G. Fontana, R. Mezzena, S. Vitale, M. Cerdonio, M. Mück, G. Hallmanns and C. Heiden, "Improved sensitivity of planar microwave biased rf SQUIDs using a cryogenic HEMT preamplifier", *IEEE Trans. Appl. Supercond.* **3**, 1820-1823 (1993).

Summary

This thesis describes the development of low T_c superconducting quantum interference devices (SQUIDs) based on the relaxation oscillation principle. SQUIDs are the most sensitive magnetic flux sensors available nowadays. As they can detect very accurately any physical quantity that can be converted to a magnetic flux, their field of applications is wide-ranging. Examples of applications are the detection of the tiny magnetic fields generated by the human brain, the measurement of voltages in the picovolt range and the readout of cryogenic particle detectors.

A dc SQUID consists of a superconducting loop which is interrupted by two Josephson junctions. These Josephson junctions constitute a weak link between the superconducting wave functions in both parts of the SQUID loop. Due to interference of these wave functions, the voltage across a current biased dc SQUID is modulated by the magnetic flux which is applied to the SQUID loop. The flux versus voltage characteristic of a dc SQUID is periodic with a period equal to the flux quantum, $\Phi_0 = 2.07 \cdot 10^{-15}$ Wb. For most applications, the non-linear flux-to-voltage transfer function is linearized by using the SQUID as a null detector in a feedback loop, the so-called flux locked loop.

Most contemporary low T_c dc SQUIDs are based on thin film Josephson tunnel junctions, which consist of two superconducting electrodes, separated by a thin (~1 nm) insulating barrier. Due to the intrinsic capacitance of these tunnel junctions, their current versus voltage characteristics are hysteretic. Usually, this hysteresis is removed with external resistive shunts across the junctions. These resistors limit the maximum slope of the flux-to-voltage characteristic to a typical value of $\partial V/\partial\Phi = 100\ \mu V/\Phi_0$. Consequently, the typical flux noise level of a dc SQUID, $\sqrt{S_\Phi} = 1\ \mu\Phi_0/\sqrt{Hz}$, corresponds to a voltage noise of $\sqrt{S_V} \approx 0.1$ nV/$\sqrt{Hz}$ at the output. Since this is about one order of magnitude below the input noise of present room temperature amplifiers, direct voltage

readout would reduce the sensitivity considerably. Usually, amplifier limitation of the sensitivity is avoided with flux modulation techniques and resonant cryogenic impedance matching circuitry. Especially in multi-channel systems, incorporating hundreds of dc SQUIDs, such modulated readout schemes have disadvantages, such as crosstalk between adjacent channels, the complex construction of the system and the associated high production costs. Moreover, the modulation frequency, 100 to 500 kHz for most commercial systems, constrains the measurement bandwidth.

The relaxation oscillation SQUID (ROS) and the double relaxation oscillation SQUID (DROS) have been developed to enable simpler, non-modulated readout techniques, thus avoiding the drawbacks of the conventional flux locked loop configuration. The principle of operation of these "second generation" dc SQUIDs is based on relaxation oscillations which are induced in hysteretic dc SQUIDs by an external shunt, consisting of an inductor L and a resistor R in series.

In a ROS, this external L-R circuit shunts a single hysteretic dc SQUID. If a ROS is biased with an appropriate dc bias current, the relaxation oscillation process generates voltage pulses with a typical amplitude of 1 mV. The frequency of these pulses depends on the critical current of the hysteretic dc SQUID, which itself depends on the applied magnetic flux. Therefore, a ROS is a flux-to-frequency converter. ROSs can also be used as flux-to-voltage transducers, but the flux-to-voltage transfer coefficient of a ROS is typically of the same order as that of conventional resistively shunted dc SQUIDs. Therefore, voltage readout of a ROS has no significant advantages compared with voltage readout of a conventional dc SQUID.

Theoretically, the sensitivity of a ROS is limited by the thermal noise on the critical current of the hysteretic dc SQUID. The sensitivity improves if the relaxation frequency is increased, but as soon as the relaxation frequency exceeds ~1% of the plasma frequency of the Josephson junctions, interference between the relaxation oscillations and the plasma oscillations impedes further improvement of the sensitivity. Therefore, the optimum relaxation frequency is about 1 GHz for most practical devices. At this relaxation frequency, the theoretical noise performance of a ROS matches that of standard dc SQUIDs.

For ROSs operating at frequencies in the GHz range, parasitic L-C resonances between the shunt inductor and the capacitance of the Josephson junctions can seriously degrade the performance. Such parasitic resonances can be suppressed with an additional damping resistor.

Several ROSs with different parameters have been investigated experimentally. These ROSs were not equipped with multi-turn input coils. The flux versus frequency characteristics of the devices were measured at various values of the bias current. The highest observed relaxation frequency was ~7 GHz; higher frequencies could not be detected due to the noise of the readout amplifier at room temperature. The experimental characteristics were

successfully fitted with a simple model, and the values of the fit parameters were in close agreement with the theoretical expectation.

The ROSs were also operated in a flux locked loop with frequency readout. The best measured white flux noise was $\sqrt{S_\Phi} = 2.5\ \mu\Phi_0/\sqrt{\text{Hz}}$, which corresponds to an energy resolution of $\varepsilon \approx 600\,h$. This energy sensitivity exceeds the theoretical value by two orders of magnitude, which discrepancy is probably caused by the non-ideal FM demodulator which was used for the flux locked loop experiments. The application of a cryogenic high frequency pre-amplifier could possibly improve the flux locked loop performance, but this would lead to a rather complex readout configuration.

DROSs are used with voltage readout instead of frequency readout. Their large flux-to-voltage transfer coefficient enables direct voltage readout with a room temperature amplifier without degradation of the sensitivity. In a DROS, two hysteretic dc SQUIDs in series, the signal SQUID and the reference SQUID, are shunted by an external L-R circuit. The signal flux is applied to the signal SQUID, whereas a constant flux is applied to the reference SQUID in order to tune its critical current to a fixed value. Depending on the value of the signal flux, either the signal SQUID or the reference SQUID participates in the relaxation oscillations, while the other SQUID remains superconducting.

The maximum flux-to-voltage transfer coefficient of a DROS is determined by the thermal spread on the critical currents of both SQUIDs, a typical value for practical devices is $\partial V/\partial\Phi \approx 1\ \text{mV}/\Phi_0$. As for a ROS, the sensitivity of a DROS improves at increasing relaxation frequencies. At relaxation frequencies exceeding ~1% of the plasma frequency, interactions between the plasma oscillations and the relaxation oscillations limit the flux-to-voltage transfer coefficient and the sensitivity of a DROS, which implies an optimum relaxation frequency of ~1 GHz for most practical devices. At this frequency, the sensitivity of a DROS is comparable to that of a conventional dc SQUID.

Several measurement systems based on DROSs are discussed in this thesis. A three-channel first-order gradiometer system with wire-wound pickup coils was constructed in order to investigate the applicability of DROSs in multi-channel magnetometer systems. The white magnetic field noise of this system, 4 fT/√Hz (~10 fT/√Hz @ 1 Hz), did not change when the three channels were operated simultaneously. This demonstrates that interference of the relaxation oscillations in adjacent DROSs does not play a significant role in multi-channel systems, which makes the DROS a promising device for use in large bio-magnetic systems.

Using the experience acquired with this three-channel gradiometer system, improved DROSs were designed, fabricated and characterized. In order to reduce the direct pickup of magnetic fields, the signal SQUIDs of these new DROSs had a gradiometric “figure-8” configuration. Another innovation was the substitution of the reference SQUID by a single reference junction. In this way, the number of wires between the DROS and the room temperature electronics could be decreased by two. The white flux noise of the devices with a

reference junction, 6 $\mu\Phi_0/\sqrt{Hz}$ ($\varepsilon \approx 200\ h$), was only slightly larger than that of the devices with a reference SQUID, 5 $\mu\Phi_0/\sqrt{Hz}$ ($\varepsilon \approx 150\ h$). Connected to an external planar first-order gradiometer with pickup coils of 2 x 2 cm^2, the devices reached a magnetic field sensitivity better than 2 $fT/\sqrt{Hz}$ (~10 $fT/\sqrt{Hz}$ @ 1 Hz) inside a magnetically shielded room, which is amply sufficient for a wide variety of bio-magnetic experiments. The gradiometric DROSs were also used as very sensitive current sensors with a resolution of 2 $pA/\sqrt{Hz}$. This application was demonstrated by recording the subgap current versus voltage characteristics of a voltage biased tunnel junction at temperatures between 1.6 K and 4.2 K.

In order to increase the effective pickup area without using an external flux transformer, a directly coupled eight-loop DROS magnetometer was developed. Owing to the multi-loop structure of the signal SQUID, a relatively large effective pickup area of 4.1 mm^2 could be realized with a moderate SQUID inductance of 410 pH. However, due to the Johnson noise generated in the damping resistors, the flux-to-voltage transfer coefficient of the directly coupled devices was limited to 280 $\mu V/\Phi_0$. As a direct consequence of this moderate transfer, the magnetic field sensitivity of the multi-loop DROS magnetometer was restricted to 7 $fT/\sqrt{Hz}$ due to the noise of the room temperature readout amplifier.

The pulsed output signal of a DROS is particularly suited for digital readout. In a digital or “smart” DROS, the voltage pulses produced by the signal SQUID and the reference SQUID drive a bi-directional digital counter whose output supplies the feedback flux to keep the DROS flux locked. Thus, the role of the digital counter is comparable to that of the integrator in the conventional flux locked loop configuration.

Especially when the counter and the DROS are integrated on a single chip, the smart DROS configuration can lead to a simpler readout scheme, requiring for instance less wires between the cryogenic environment and room temperature. Unlike other types of digital SQUIDs, the smart DROS does not need an external clock for operation, because the relaxation oscillations constitute an internal clock. Therefore, a smart DROS can work at high frequencies, which makes it potentially a very fast sensor.

A prototype of the smart DROS has been designed, fabricated and characterized. The bi-directional counter in this prototype is based on a so-called Josephson counter, consisting of a superconducting storage loop and two write gates. These write gates, which are driven by the voltage pulses generated by the DROS, can add flux quanta to or remove flux quanta from the quantized flux in the storage loop. The circulating current in the storage loop generates the feedback flux for the DROS via a flux transformer. For readout of the Josephson counter, an additional resistively shunted dc SQUID, coupled to the circulating current in the counter by means of a second flux transformer, was included in the design. This readout SQUID was operated in a flux locked loop with room temperature electronics. Of course, this readout configuration

limits the versatility of the prototype considerably, but the main goal of the present experiments was to demonstrate the feasibility of the smart DROS concept.

The smart DROS prototype, having a relaxation frequency of ~100 MHz, worked properly and its response was linear over an input flux range of ~3 Φ_0. The bandwidth and the maximum slew rate of the prototype were limited by the external flux locked loop circuitry of the readout SQUID. The flux noise of the device, 6.5 $\mu\Phi_0/\sqrt{\text{Hz}}$ ($\varepsilon \approx 2000\ h$) including the noise of the readout SQUID and 5 $\mu\Phi_0/\sqrt{\text{Hz}}$ ($\varepsilon \approx 1150\ h$) excluding the noise of the readout SQUID, was even better than the noise level of 7 $\mu\Phi_0/\sqrt{\text{Hz}}$ which was measured for the same DROS, operated in a conventional instead of a “smart” flux locked loop.

These promising results encourage further development of the smart DROS. An example of a new development could be the replacement of the superconducting Josephson counter by a cryogenic semiconducting circuit. Such improved smart DROSs can for instance be used in large multi-channel SQUID systems - e.g. for bio-magnetic measurements - or in applications requiring a wide measurement bandwidth, such as the readout of cryogenic particle detectors.

Samenvatting (Summary in Dutch)

Dit proefschrift beschrijft de ontwikkeling van lage-T_c SQUIDs die gebaseerd zijn op het relaxatie oscillatie principe. Het woord SQUID is een acroniem voor het Engelse *Superconducting QUantum Interference Device*. SQUIDs zijn de gevoeligste sensoren voor magnetische flux die momenteel bestaan. Omdat ze iedere fysische grootheid die naar magnetische flux is te "vertalen" met grote precisie kunnen meten hebben ze een breed toepassingsgebied. Voorbeelden van toepassingen zijn de detectie van de zeer kleine magnetische velden die worden gegenereerd door menselijke hersenen of andere organen, het meten van elektrische spanningen in het picovoltbereik en de uitlezing van cryogene deeltjesdetectors.

Een dc SQUID bestaat uit een supergeleidende ring die op twee plaatsen is onderbroken door een Josephson junctie. Deze Josephson juncties vormen een zwakke koppeling tussen de supergeleidende golffuncties in beide delen van de ring, waardoor interferentie mogelijk is. Ten gevolge van deze interferentie is de elektrische spanning over een stroom-gebiast dc SQUID afhankelijk van de magnetische flux die wordt omsloten door de SQUID-ring. De flux versus spanning karakteristiek van een dc SQUID is periodiek, met een periode gegeven door het fluxquantum $\Phi_0 = 2.07 \cdot 10^{-15}$ Wb. Deze niet-lineaire flux-naar-spanning overdrachtsfunctie wordt meestal gelineariseerd door het SQUID als een nuldetector in een teruggekoppeld systeem, de zogenaamde *flux locked loop*, te gebruiken.

De meeste moderne lage-T_c dc SQUIDs zijn gebaseerd op dunne film Josephson tunnel juncties, bestaande uit twee supergeleidende electrodes gescheiden door een dunne (~1 nm) isolerende barrière. Door hun inherente capaciteit hebben zulke Josephson tunnel juncties een hysteretische stroom versus spanning karakteristiek. Gewoonlijk wordt deze hysterese opgeheven met shuntweerstanden over de juncties. Deze weerstanden beperken de

maximale helling van de flux versus spanning karakteristiek echter tot een typische waarde van $\partial V/\partial\Phi = 100\ \mu V/\Phi_0$. Dientengevolge komt de typische fluxruis van $1\ \mu\Phi_0/\sqrt{Hz}$ overeen met een spanningsruis van $0.1\ nV/\sqrt{Hz}$ aan de uitgang van het SQUID, hetgeen een grootteorde lager is dan de ingangsruis van moderne versterkers op kamertemperatuur. Daarom zou directe spanningsuitlezing met een versterker op kamertemperatuur de gevoeligheid van een SQUID systeem aanzienlijk beperken. Om dit te voorkomen worden gewoonlijk fluxmodulatietechnieken en resonante impedantie-aanpassings-circuits toegepast. Vooral in meer-kanaals systemen, die uit honderden individuele SQUIDs kunnen bestaan, hebben zulke gemoduleerde schema's nadelen. Zo kan het modulatiesignaal, dat in de meeste commerciële systemen een frequentie van 100 tot 500 kHz heeft, overspraak tussen aangrenzende kanalen veroorzaken en wordt de bandbreedte van het systeem er door beperkt. Verder maakt het gemoduleerde uitlezingsschema SQUID systemen complexer en dus duurder.

Het relaxatie oscillatie SQUID (ROS) en het dubbele relaxatie oscillatie SQUID (DROS) zijn ontworpen om eenvoudigere, niet-gemoduleerde uitlezings-methoden mogelijk te maken. Het werkingsprincipe van deze "tweede generatie" dc SQUIDs berust op relaxatie oscillaties die worden opgewekt in hysteretische dc SQUIDs door een externe shunt, bestaande uit een serieschakeling van een inductie L en een weerstand R.

In een ROS staat deze externe L-R shunt parallel aan een enkel hysteretisch dc SQUID. Als een ROS wordt gebiast met een geschikte gelijkstroom, worden spanningspulsen met een typische amplitude in de orde van 1 mV opgewekt. De frequentie van deze pulsen hangt af van de kritische stroom van het hysteretische dc SQUID, die op zijn beurt weer afhankelijk is van de aangeboden magnetische flux. Zodoende is een ROS een flux-naar-frequentie omzetter. Net als conventionele dc SQUIDs kunnen ook ROSsen gebruikt worden als flux-naar-spanning omzetters. Maar aangezien de flux-naar-spanning overdrachtscoëfficiënt van een ROS vergelijkbaar is met die van een conventioneel dc SQUID, levert spanningsuitlezing van een ROS geen belangrijke voordelen op.

De theoretische gevoeligheid van een ROS wordt bepaald door de thermische ruis op de kritische stroom van het hysteretische dc SQUID. Als de relaxatiefrequentie wordt verhoogd, verbetert de gevoeligheid. Echter, bij relaxatiefrequenties hoger dan ~1% van de plasmafrequentie van de Josephson juncties verhindert interferentie tussen de relaxatie oscillaties en de plasma oscillaties een verdere verbetering van de gevoeligheid. Dit impliceert een optimale relaxatiefrequentie van ~1 GHz voor praktische ROSsen. Theoretisch heeft een ROS bij deze frequentie dezelfde gevoeligheid als een conventioneel dc SQUID.

Parasitaire L-C resonanties tussen de shunt-inductie en de capaciteit van de Josephson juncties kunnen de gevoeligheid van ROSsen met een relaxatie-

frequentie in het GHz-gebied ernstig beperken. Dergelijke parasitaire resonanties kunnen worden voorkomen met een extra dempingsweerstand.

Van verschillende ROSsen zonder geïntegreerde inkoppelspoel zijn de flux versus frequentie karakteristieken gemeten voor uiteenlopende waarden van de biasstroom. De hoogst waargenomen relaxatiefrequentie was ~7 GHz; hogere frequenties waren niet meetbaar vanwege de ruis van de gebruikte voorversterker. De experimentele karakteristieken konden goed worden beschreven met een eenvoudig model, en de gevonden waarden voor de model-parameters waren in goede overeenstemming met de verwachtingswaarden.

De ROSsen zijn ook gebruikt in een flux locked loop met frequentie-uitlezing. De laagste fluxruis die gemeten werd, $\sqrt{S_\Phi} = 2.5\ \mu\Phi_0/\sqrt{\text{Hz}}$, komt overeen met een energieresolutie van $\varepsilon \approx 600\,h$. Dit is meer dan twee grootteordes hoger dan de theoretische waarde, wat waarschijnlijk een gevolg is van de niet-ideale FM-demodulator die werd gebruikt. Een cryogene hoogfrequente voorversterker zou de ruiseigenschappen mogelijkerwijs kunnen verbeteren, maar dit zou tot een complex systeem leiden.

DROSsen worden gebruikt met spannings- in plaats van frequentie-uitlezing. Dankzij hun hoge flux-naar-spanning overdrachtscoëfficiënt is directe spanningsuitlezing met een versterker op kamertemperatuur mogelijk zonder verlies van gevoeligheid. In een DROS zijn twee hysteretische dc SQUIDs, het signaal-SQUID en het referentie-SQUID, geshunt met een extern L-R circuit. De te meten signaalflux wordt aangeboden aan het signaal-SQUID, en de kritische stroom van het referentie-SQUID wordt op een vaste waarde ingesteld door middel van een constante flux. Afhankelijk van de waarde van de signaalflux neemt ofwel het signaal-SQUID, ofwel het referentie-SQUID deel aan het relaxatie oscillatie proces, terwijl het andere SQUID supergeleidend blijft.

De maximale flux-naar-spanning overdrachtscoëfficiënt van een DROS wordt bepaald door de thermische spreiding op de kritische stromen van beide SQUIDs; een typische waarde voor praktische DROSsen is $\partial V/\partial\Phi = 1\ \text{mV}/\Phi_0$. Net zoals voor een ROS verbetert ook de gevoeligheid van een DROS als de relaxatiefrequentie wordt verhoogd. Ook voor DROSsen speelt interferentie van de relaxatie oscillaties en de plasma oscillaties in de Josephson juncties een rol als de relaxatiefrequentie ~1% van de plasmafrequentie overschrijdt. Deze interferentie beperkt de flux-naar-spanning overdrachtscoëfficiënt en de gevoeligheid. In de praktijk betekent dit een optimale relaxatiefrequentie van ongeveer 1 GHz. De gevoeligheid van een DROS met deze relaxatiefrequentie is vergelijkbaar met die van een conventioneel dc SQUID.

Verschillende op DROSsen gebaseerde meetsystemen worden in dit proefschrift besproken. Om de toepasbaarheid van DROSsen in meer-kanaals magnetometer systemen te onderzoeken werd een drie-kanaals DROS eerste-orde gradiometer met draadgewonden oppikspoelen gebouwd. De ruis van dit systeem, $4\ \text{fT}/\sqrt{\text{Hz}}$ ($\sim 10\ \text{fT}/\sqrt{\text{Hz}}$ @ 1 Hz), veranderde niet wanneer de drie kanalen tegelijkertijd actief waren. Dit betekent dat interferentie van de

relaxatie oscillaties in aangrenzende DROSsen geen belangrijke rol speelt in meer-kanaals DROS magnetometers. Dit maakt het DROS een veelbelovende kandidaat voor biomagnetische systemen.

Met de ervaringen opgedaan bij de constructie van dit drie-kanaals gradiometer systeem zijn verbeterde DROSsen ontworpen. Om de invloed van externe magnetische storingen te beperken werd voor een achtvormig gradiometrisch signaal-SQUID gekozen. Een andere innovatie was de vervanging van het referentie-SQUID door een enkele referentie-junctie. Dit heeft als voordeel dat er twee draden minder nodig zijn tussen het DROS en de elektronica op kamertemperatuur. De witte fluxruis van de DROSsen met een referentie-junctie, 6 $\mu\Phi_0/\sqrt{Hz}$ ($\varepsilon \approx 200\ h$), was slechts een fractie hoger dan de ruis van de exemplaren met een referentie-SQUID, die 5 $\mu\Phi_0/\sqrt{Hz}$ ($\varepsilon \approx 150\ h$) bedroeg. Verbonden met een externe planaire eerste-orde gradiometer met oppikspoelen van 2 x 2 cm^2 werd een gevoeligheid beter dan 2 $fT/\sqrt{Hz}$ (~10 $fT/\sqrt{Hz}$ @ 1 Hz) gemeten in een magnetisch afgeschermde ruimte. Dit is ruimschoots voldoende voor allerhande biomagnetische metingen. De gradiometrische DROSsen zijn ook gebruikt als zeer gevoelige stroommeters met een resolutie van 2 $pA/\sqrt{Hz}$. Deze toepassing werd gedemonstreerd door de subgap stroom versus spanning karakteristieken van een spannings-gebiaste Josephson tunnel junctie te meten bij temperaturen tussen 1.6 K en 4.2 K.

Om het effectieve oppervlak te vergroten zonder een externe flux-transformator werd een direct gekoppeld “karrenwiel” DROS ontwikkeld waarvan de inductie van het signaal-SQUID was opgebouwd uit acht parallelle supergeleidende lussen. Dankzij deze configuratie kon een effectief oppervlak van 4.1 mm^2 bereikt worden bij een relatief lage SQUID-inductie van 410 pH. De flux-naar-spanning overdrachtscoëfficiënt van deze direct gekoppelde DROSsen was echter beperkt tot 280 $\mu V/\Phi_0$ door de Johnson ruis opgewekt in de dempingsweerstanden. Als een direct gevolg van deze relatief lage overdracht was de gevoeligheid van deze DROSsen, 7 $fT/\sqrt{Hz}$, begrensd door de ruis van de voorversterker.

Het gepulste karakter van het uitgangssignaal van een DROS is uitermate geschikt voor digitale verwerking. In zo'n digitaal of “smart” DROS sturen de spanningspulsjes van het DROS een bidirectionele teller aan. De uitgang van deze teller levert op zijn beurt de terugkoppelingsflux om het DROS in flux locked loop te houden. Derhalve is de functie van de teller te vergelijken met die van de integrator in een conventionele flux locked loop.

Vooral wanneer de teller en het DROS op één enkele chip geïntegreerd zijn, kan het smart DROS bijdragen aan een eenvoudigere uitlezing en een reductie van het aantal draden tussen de sensoren en de omgeving. Daar de relaxatie oscillaties een interne klok vormen heeft het smart DROS geen extern kloksignaal nodig, dit in tegenstelling tot andere digitale SQUIDs. Hierdoor kan een smart DROS op hoge frequenties werken, wat het potentieel tot een zeer snelle sensor maakt.

Een prototype van het smart DROS is ontwikkeld en getest. In dit prototype werd een zogenaamde Josephson-teller, bestaande uit een supergeleidende opslaglus en twee schrijfpoorten, gebruikt. Via deze schrijfpoorten, die worden aangestuurd door de spanningspulsen van het DROS, kunnen fluxquanta toegevoegd (en verwijderd) worden aan de gequantiseerde flux in de opslaglus. De kringstroom in de opslaglus genereert de terugkoppelingsflux voor het DROS via een fluxtransformator. Voor de uitlezing van de teller werd een niet-hysteretisch dc SQUID, magnetisch gekoppeld met de opslaglus via een tweede fluxtransformator, gebruikt. Dit uitlezings-SQUID werd in flux locked loop gebracht met elektronica op kamertemperatuur. Natuurlijk beperkt deze uitlezingsmethode de praktische bruikbaarheid van het smart DROS - er is immers nog steeds externe flux locked loop elektronica benodigd - maar het hoofddoel van het prototype was het demonstreren van het smart DROS concept.

Het smart DROS prototype, met een relaxatiefrequentie van ~100 MHz, werkte naar behoren en had een lineair ingangsbereik van ongeveer 3 Φ_0. De bandbreedte en de maximale slew rate waren begrensd door de externe flux locked loop van het uitlezings-SQUID. De fluxruis was 6.5 $\mu\Phi_0/\sqrt{\text{Hz}}$ ($\varepsilon \approx 2000\ h$) inclusief de ruis van het uitlezings-SQUID en 5 $\mu\Phi_0/\sqrt{\text{Hz}}$ ($\varepsilon \approx 1150\ h$) exclusief deze ruisbijdrage. Dit is zelfs beter dan het ruisniveau van 7 $\mu\Phi_0/\sqrt{\text{Hz}}$ dat werd gemeten met hetzelfde DROS in een conventionele in plaats van een “smart” flux locked loop.

Deze veelbelovende resultaten moedigen aan tot verder onderzoek. Een voorbeeld van een mogelijke nieuwe ontwikkeling is de vervanging van de Josephson-teller door een teller op basis van halfgeleiders. Zulke verbeterde smart DROSsen zouden bijvoorbeeld kunnen worden gebruikt voor grote meer-kanaals systemen ten behoeve van biomagnetische experimenten, of voor toepassingen waarin een hoge bandbreedte is vereist, zoals de uitlezing van cryogene deeltjesdetectors.

Dankwoord

Dit proefschrift beschrijft de resultaten van het onderzoek dat ik de afgelopen vier jaren als OIO heb verricht bij de leerstoel Lage Temperaturen. Ofschoon velen hebben bijgedragen aan het plezier waarmee ik dit gedaan heb, wil ik toch enkele personen met name noemen.

Allereerst wil ik mijn promotor Horst Rogalla en assistent-promotor Jaap Flokstra bedanken voor de mogelijkheid die ze me boden om dit onderzoek te doen. Tijdens de periodieke werkbesprekingen hield Jaap de vinger aan de pols, voldoende ruimte overlatend voor eigen initiatief.

Het enthousiasme van mijn voorganger Derk Jan Adelerhof werkte zo aanstekelijk dat ik besloot om dit promotieonderzoek te gaan doen. Eerst als student en later als beginnend promovendus heb ik van hem de fijne kneepjes van het vak geleerd, waarvoor ik hem nogmaals wil bedanken.

Of het nu de fabricage van samples, het modificeren van de opstelling of het genereren van een ruisarm hartsignaal betrof, Christian Brons draaide z'n hand er niet voor om. Zijn technische ondersteuning was perfect en onze samenwerking verliep zeer plezierig.

Diverse studenten hebben met hun afstudeeropdracht een belangrijke steen bijgedragen aan de totstandkoming van dit proefschrift. Martin Siekman heeft zich beziggehouden met het realiseren van een flux locked loop opstelling voor ROSsen, Harm Wichers ontwierp het direct gekoppelde “karrenwiel” DROS, Erik Korterink maakte de planaire gradiometer en Hans Kattouw heeft een belangrijke bijdrage geleverd aan de ontwikkeling van de Josephson-teller. Ik wil hen allemaal hartelijk bedanken voor hun inzet.

Arnout Hamster en Eric Bréelle hebben het manuscript van dit proefschrift zorgvuldig gelezen en van het nodige commentaar voorzien. Arnout leverde ook een wezenlijke bijdrage aan de metingen in paragraaf 4.5. Ik wens hem veel succes met het vervolg van deze experimenten.

Harry Steffens zorgde voor het voor dit onderzoek onontbeerlijke vloeibare helium en Dick Veldhuis bewerkte een aantal samples met de FIB, waarvoor ik hen graag wil bedanken.

Natuurlijk mogen in een lijst als deze mijn ouders en Marjolein niet ontbreken. Zonder hun interesse en steun zou mijn promotietijd er heel anders hebben uitgezien.